



Structure of Brightest Cluster Galaxies and Intracluster Light

M. Kluge^{1,2} , B. Neureiter², A. Riffeser¹ , R. Bender^{1,2} , C. Goessl¹ , U. Hopp^{1,2}, M. Schmidt¹, C. Ries¹, and N. Brosch³

¹University-Observatory, Ludwig-Maximilians-University, Scheinerstrasse 1, D-81679 Munich, Germany

²Max Planck Institute for Extraterrestrial Physics, Giessenbachstrasse, D-85748 Garching, Germany

³Tel Aviv University, Tel Aviv, 69978, Israel

Received 2019 August 21; revised 2020 January 17; accepted 2020 February 4; published 2020 March 16

Abstract

Observations of 170 local ($z \lesssim 0.08$) galaxy clusters in the northern hemisphere have been obtained with the Wendelstein Telescope Wide Field Imager (WWFI). We correct for systematic effects such as point-spread function broadening, foreground star contamination, relative bias offsets, and charge persistence. Background inhomogeneities induced by scattered light are reduced down to $\Delta SB > 31 \text{ g' mag arcsec}^{-2}$ by large dithering and subtraction of night-sky flats. Residual background inhomogeneities brighter than $SB_\sigma < 27.6 \text{ g' mag arcsec}^{-2}$ caused by galactic cirrus are detected in front of 23% of the clusters. However, the large field of view allows discrimination between accretion signatures and galactic cirrus. We detect accretion signatures in the form of tidal streams in 22%, shells in 9.4%, and multiple nuclei in 47% of the brightest cluster galaxies (BCGs) and find two BCGs in 7% of the clusters. We measure semimajor-axis surface brightness profiles of the BCGs and their surrounding intracluster light (ICL) down to a limiting surface brightness of $SB = 30 \text{ g' mag arcsec}^{-2}$. The spatial resolution in the inner regions is increased by combining the WWFI light profiles with those that we measured from archival *Hubble Space Telescope* images or deconvolved WWFI images. We find that 71% of the BCG+ICL systems have surface brightness (SB) profiles that are well described by a single Sérsic function, whereas 29% require a double Sérsic function to obtain a good fit. We find that BCGs have scaling relations that differ markedly from those of normal ellipticals, likely due to their indistinguishable embedding in the ICL.

Unified Astronomy Thesaurus concepts: cD galaxies (209); Galaxy formation (595); Galaxy stellar halos (598); Surface photometry (1670); Scaling relations (2031); Brightest cluster galaxies (181)

Supporting material: extended figures, machine-readable table

1. Introduction

Following the first detection of an “extended mass of luminous intergalactic matter of very low surface brightness” in the Coma cluster (Zwicky 1951), numerous early studies have confirmed that subgroupings of galaxies in clusters “[...] often share a common outer envelope several hundred kiloparsecs in diameter” (Kormendy & Bahcall 1974; also Arp & Bertola 1971; Welch & Sastry 1971; Thuan & Kormendy 1977). A similar envelope was discovered to surround the Virgo cluster galaxy M87 (Arp & Bertola 1969; de Vaucouleurs 1969).

Today, we know that many galaxy clusters are populated by an outstandingly bright and extended elliptical galaxy near the geometric and kinematic cluster center. They are referred to as brightest cluster galaxies (BCGs). The definition of this galaxy type is similar to the historic definition of cD galaxies (Matthews et al. 1964; Morgan & Lesh 1965). cD galaxies form a subset of BCGs that are surrounded by an extended, diffuse stellar envelope. That envelope is part of the ex situ stellar population that was accreted during mass assembly (Cooper et al. 2013, 2015; Pillepich et al. 2018). It is probably mixed with the intracluster light (ICL), which is kinematically unbound from the BCG. In this work, we do not distinguish between stellar envelope, stellar halo, and ICL because they are probably indistinguishable with photometric data alone. Oegerle & Hill (2001) classify 20% of BCGs as cD galaxies. The issue with this subset definition is that the detection of an existing envelope depends on the depth of the observation. Moreover, large samples of BCGs are Gaussian distributed in their brightnesses (Postman & Lauer 1995; Hansen et al. 2009; Donzelli et al. 2011; Lauer et al. 2014), which implies that the transition

between cD and non-cD BCGs is continuous. Hence, it makes sense to study BCGs as a generalized class of galaxies.

Contrary to what the name suggests, a BCG is in our adopted definition not necessarily the brightest galaxy in a cluster: it must also lie close to the cluster center as traced by the satellite galaxy distribution or the intracluster medium. Between 20% and 40% of central galaxies are not the brightest galaxy in their host clusters (Skibba et al. 2011; Hoshino et al. 2015). A famous example is M87 in the Virgo cluster. The brightest galaxy is M49, but it is located far off the cluster center. M87 is (in projection) near the X-ray gas emission peak (e.g., Kellogg et al. 1971), which is a good tracer for the potential minimum of the cluster. Moreover, the rising velocity dispersion profile of the surrounding planetary nebulae is steeper for M87 (Longobardi et al. 2018) than for M49 (Hartke et al. 2018), showing that intracluster planetary nebulae are more centered on M87 than on M49. The velocity dispersion profile of the globular clusters rises toward the outskirts of M87 (Côté et al. 2001), but it falls toward the outskirts of M49 (Sharples et al. 1998), showing that the intracluster globular clusters are also more centered on M87. All of the arguments above agree that M87 qualifies better as the BCG of the Virgo cluster in our adopted definition.

The currently widely accepted two-phase formation scenario (e.g., Contini et al. 2014, 2018) states that the BCG formed first by galactic mergers and the ICL was accreted afterward by a mixture of (1) galaxy harassment, that is, high-velocity encounters between satellite galaxies (Moore et al. 1996); (2) tidal stripping induced by effects of dynamical friction against the whole cluster potential (Byrd & Valtonen 1990; Gnedin 2003); and (3) preprocessing in smaller groups (Mihos 2004; Rudick et al. 2006). Remnants of these violent processes are predicted by simulations to occur at low

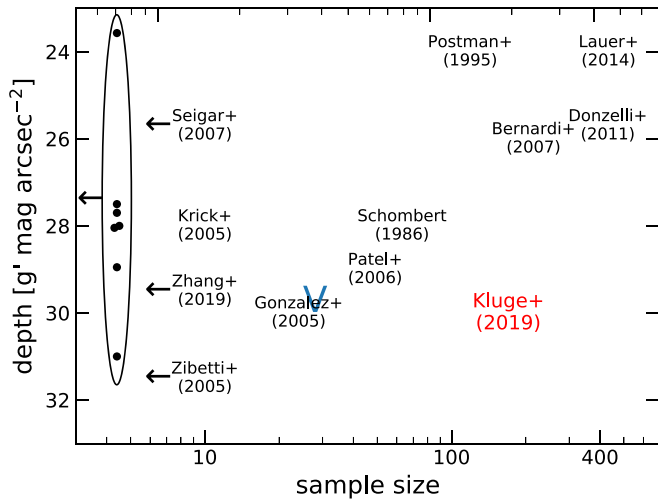


Figure 1. Overview of photometric low-redshift BCG surveys: Seigar et al. (2007), Krick & Bernstein (2005), Zhang et al. (2019), Zibetti et al. (2005), Gonzalez et al. (2005), Patel et al. (2006), Schombert (1986), Postman & Lauer (1995), Bernardi et al. (2007), Lauer et al. (2014), Donzelli et al. (2011). The so far published VST survey of Early-type GALaxieS (VEGAS) sample is shown by a blue “V” (Capaccioli et al. 2015; Spavone et al. 2017, 2018; Cattapan et al. 2019). The dots embedded in the ellipse represent single- or double-target BCG observations. From top to bottom: Jorgensen et al. (1992), Bender et al. (2015), Ferrarese et al. (2012), Feldmeier et al. (2002), Kormendy et al. (2009), Mihos et al. (2005), Iodice et al. (2016). The arrows indicate that the sample size is smaller than the label position in the plot. Our survey (red) populates an unexplored parameter space region in sample size and depth.

surface brightnesses (SBs), mostly below $SB \gtrsim 29$ g' mag arcsec $^{-2}$ (Rudick et al. 2009; Puchwein et al. 2010; Harris et al. 2017; Mancillas et al. 2019), and are confirmed by observations (e.g., Arnaboldi et al. 2012; Kormendy & Bender 2012; Iodice et al. 2017; Mihos et al. 2017). We refer to these remnants as accretion signatures.

The build-up, shape, and substructure of BCG+ICL light profiles, as well as the types and abundances of accretion signatures, are sensitive probes for the dynamical evolution of galaxy clusters (e.g., Puchwein et al. 2010; Cui et al. 2014). To constrain formation models, especially in the faint outskirts of BCGs, a large sample of BCGs with deep light profiles is needed. Figure 1 illustrates that so far, either the studied sample was relatively small (Gonzalez et al. 2005; Krick & Bernstein 2005; Patel et al. 2006; Seigar et al. 2007) or the surface brightness at the transition radius between the two photometric components of double Sérsic BCGs is mostly below the limiting magnitude of the surveys (Postman & Lauer 1995; Bernardi et al. 2007; Donzelli et al. 2011; Lauer et al. 2014). In this paper, we present a study that fulfills both criteria. We perform a statistical analysis of the SB profiles, isophotal shape profiles, and structural parameters of BCG+ICLs. An analysis of the correlations of these parameters with host cluster properties and various approaches to separating the ICL from the BCGs is reserved for an forthcoming paper.

This paper is organized as follows. In Section 2, we present our sample and selection criteria. The data and data reduction are described in Section 3. Our methods to measure and combine the surface brightness profiles are described in Section 4. Sections 3 and 4 are dedicated to readers who are interested in the image processing techniques necessary for deep imaging. An extensive error analysis is given in Section 5. We present our results of accretion signatures, average profiles, and structural parameters in Section 6. They are discussed in Section 7 and summarized in Section 8.

Throughout the paper we assume a flat cosmology with $H_0 = 69.6$ km s $^{-1}$ Mpc $^{-1}$ and $\Omega_m = 0.286$. Distances and angular scales were calculated using the web tool from Wright (2006). Virgo infall is not considered. If not stated otherwise, then three types of flux corrections were applied: (1) dust extinction using the maps from Schlafly & Finkbeiner (2011), (2) K corrections following Chilingarian et al. (2010) and Chilingarian & Zolotukhin (2012), and (3) cosmic $(1+z)^4$ dimming. Magnitudes are always given in the AB system.

2. Sample Selection

Our sample is based on the Abell–Corwin–Olowin (ACO) catalog (Abell et al. 1989). It contains 4073 rich galaxy clusters, out of which we selected 141 by the following criteria:

1. redshift $z \lesssim 0.08$,
2. galactic latitude $|b| > 13^\circ$,
3. decl. $> +5^\circ$,
4. no bright stars nearby.

Regarding the fourth criterion, a stellar brightness limit in the range $5 < g < 9$, where g is the stellar magnitude in the g band, is applied, depending on the projected distance $2''.6 < d < 0''.08$ from the BCG. Additionally, we allow 15 exceptions from the redshift constraint because of preobservational misidentification of the BCG and one exception from the decl. constraint: A85 was observed for a different program. The sample is extended with nine clusters from the Von Der Linden et al. (2007) catalog, three clusters from the Albert et al. (1977) catalog, and one group from the Morgan et al. (1975) catalog. The final sample of 170 BCGs is listed in Table 1, and its spatial distribution is shown in Figure 2.

In order to investigate the completeness of our sample, we plot the BCG redshifts against the total BCG+ICL brightness in Figure 3. A slight Malmquist bias is seen by the upward trend of the average brightness with increasing redshift, shown by the red line.

Furthermore, we compare the completeness of our sample to that of the most comprehensive samples available in the literature, Lauer et al. (2014) and Donzelli et al. (2011). After applying the same volume-limiting constraints, the overlap of Lauer et al.’s sample on our sample is 90%. An overall agreement is expected because both Lauer et al.’s and our samples are mainly drawn from the ACO catalogs. Following the same criteria, the overlap with the sample of Donzelli et al. is 89%, and vice versa 80%.

The selection of the BCG in each cluster was done manually while inspecting the deep Wendelstein Telescope Wide Field Imager (WWFI) images. We always chose the most extended elliptical galaxy (at the ~ 27 g' mag arcsec $^{-2}$ isophote) that is located close to the cluster center, as traced by the X-ray gas or satellite galaxy distribution. It usually coincides with the brightest galaxy in the cluster, but that is not a stringent criterion. Our choices differ in 26 (20%) out of the 127 clusters that overlap with the Lauer et al. (2014) sample, who select the brightest galaxy measured in a metric aperture of 10 h $^{-1}$ kpc radius. That is a consequence of the more cD-like definition of BCGs that we adopted. Out of those 26 galaxies, 15 are marked as the second-brightest galaxy in the Lauer et al. sample.

Private discussion with Tod Lauer and Marc Postman revealed that the choice of the BCG in those clusters is debatable. That is mainly due to (1) the Abell cluster number does not unambiguously identify a cluster in the case of

Table 1
BCG Sample

Cluster	BCG	R.A. (J2000)	Decl. (J2000)	z	Angular Scale (kpc arcsec ⁻¹)	L14 Selection	HST Available
(1)	(2)	(3)	(4)	(5)	(6)	(7)	(8)
A76	IC 1565	00:39:26.3	+06:44:04	0.038372	0.765	✓	✓
A85	MCG-02-02-086	00:41:50.4	−09:18:11	0.055380	1.083	✓	—
A150	UGC 716	01:09:18.4	+13:10:09	0.061321	1.190	✓	—
A152	UGC 727	01:10:03.1	+13:58:42	0.058280	1.135	✓	—
A154	IC 1634	01:11:02.9	+17:39:47	0.069478	1.336	M2	—
A158	LEDAS 1518776	01:11:46.3	+16:51:29	0.064500	1.248	other	—
A160	MCG+02-04-010	01:12:59.6	+15:29:29	0.043830	0.869	✓	✓
A161	LEDAS 2098391	01:15:22.3	+37:20:24	0.076954	1.467	✓	—
A171	MCG+03-04-014	01:17:17.9	+16:15:57	0.071670	1.375	✓	—
A174	2MASX J01201619+3548272	01:20:16.1	+35:48:27	0.078056	1.486	✓	—
A179	2MASX J01223283+1931312	01:22:32.8	+19:31:32	0.056194	1.097	M2	—
A193	IC 1695	01:25:07.6	+08:41:58	0.050171	0.987	✓	✓
A225	NVSS J013848+184931	01:38:48.9	+18:49:32	0.069375	1.334	✓	—
A240	UGC 1191	01:42:06.0	+07:39:54	0.062534	1.212	✓	—
A245	2MASX J01435285+0624499	01:43:52.8	+06:24:51	0.079310	1.508	other	—
A257	2MASX J01490841+1357474	01:49:08.3	+13:57:48	0.070540	1.355	✓	—
A260	IC 1733	01:50:42.9	+33:04:56	0.035680	0.714	✓	✓
A262	NGC 708	01:52:46.3	+36:09:07	0.016220	0.332	✓	✓
A292	UGC 1518	02:02:18.9	+19:04:02	0.064648	1.250	✓	—
A347	NGC 910	02:25:26.9	+41:49:23	0.017302	0.354	✓	✓
A376	UGC 2232	02:46:03.9	+36:54:19	0.048610	0.958	✓	✓
A397	UGC 2413	02:56:28.7	+15:54:58	0.034447	0.690	✓	✓
A399	UGC 2438	02:57:53.1	+13:01:52	0.071239	1.367	✓	—
A400	NGC 1128	02:57:41.6	+06:01:21	0.023980	0.487	✓	✓
A407	2MASX J03015146+3550283	03:01:51.8	+35:50:20	0.047820	0.943	✓	—
A426	NGC 1275	03:19:48.1	+41:30:43	0.017560	0.359	—	✓
A498	2MASX J04375071+2112203	04:37:50.7	+21:12:21	0.059823	1.163	✓	—
A505	UGC 3197	04:59:55.6	+80:10:44	0.053504	1.048	✓	—
A539	LEDAS 17025	05:16:37.3	+06:26:27	0.028142	0.568	M2	—
A553	2MASX J06124115+4835445	06:12:41.1	+48:35:45	0.069059	1.329	—	—
A559	2MASX J06395117+6958332	06:39:51.0	+69:58:34	0.075700	1.445	—	—
A568	MCG+06-16-019	07:07:41.5	+35:03:32	0.081702	1.549	✓	—
A569	NGC 2329	07:09:08.0	+48:36:56	0.019420	0.396	✓	✓
A582	2MASX J07280080+4155074	07:28:00.8	+41:55:08	0.060245	1.171	✓	—
A592	2MASX J07424058+0922207	07:42:40.6	+09:22:21	0.065651	1.268	other	—
A595	MCG+09-13-062	07:49:27.2	+52:02:33	0.070938	1.362	M2	—
A600	2MASX J07563560+6344237	07:56:35.5	+63:44:25	0.080997	1.537	✓	—
A602	2MASX J07532661+2921341	07:53:26.6	+29:21:35	0.060420	1.174	M2	—
A607	SDSS J075724.71+392106.6	07:57:24.7	+39:21:07	0.095620	1.784	—	—
A612	2MASX J08011329+3440311	08:01:13.2	+34:40:31	0.082720	1.567	—	—
A634	UGC 4289	08:15:44.8	+58:19:16	0.027090	0.548	✓	✓
A671	IC 2378	08:28:31.6	+30:25:53	0.050320	0.990	✓	✓
A688	SDSSJ083734.33+154907.6	08:37:34.3	+15:49:08	0.152620	2.672	—	—
A690	ICRF J083915.8+285038	08:39:15.8	+28:50:39	0.079020	1.503	✓	—
A695	2MASX J08411308+3224596	08:41:13.1	+32:25:00	0.071103	1.365	✓	—
A734	2MASX J09003199+1614213	09:00:32.0	+16:14:26	0.074717	1.428	—	—
A744	2MASX J09072049+1639064	09:07:20.5	+16:39:07	0.072850	1.395	✓	—
A757	2MASX J09130775+4742307	09:13:07.7	+47:42:31	0.051350	1.009	✓	—
A834	2MASX J09413277+6642376	09:41:32.7	+66:42:39	0.070910	1.361	✓	—
A883	2MASX J09511516+0529170	09:51:15.1	+05:29:17	0.078983	1.502	—	—
A999	MCG+02-27-004	10:23:23.7	+12:50:07	0.032490	0.653	✓	✓
A1003	MCG+08-19-026	10:25:01.5	+47:50:31	0.063660	1.233	✓	—
A1016	IC 613	10:27:07.8	+11:00:39	0.032370	0.650	✓	✓
A1020	2MASX J10274949+1026306	10:27:49.5	+10:26:31	0.067702	1.305	✓	—
A1056	LEDAS 2186592	10:38:01.7	+41:46:26	0.124670	2.251	—	—
A1066	2MASX J10393872+0510326	10:39:38.7	+05:10:33	0.068170	1.313	✓	—
A1100	MCG+04-26-010	10:48:45.6	+22:13:05	0.046666	0.922	✓	—
A1108	NGC 3405	10:49:43.3	+16:14:20	0.021740	0.442	—	—
A1142	IC 664	11:00:45.3	+10:33:12	0.033860	0.679	✓	✓
A1155	2MASXJ11043955+3513477	11:04:39.5	+35:13:49	0.076788	1.464	✓	—
A1173	2MASX J11091531+4133412	11:09:15.3	+41:33:42	0.076620	1.461	—	—
A1177	NGC 3551	11:09:44.4	+21:45:33	0.031830	0.640	✓	✓

Table 1
(Continued)

Cluster	BCG	R.A. (J2000)	Decl. (J2000)	z	Angular Scale (kpc arcsec ⁻¹)	L14 Selection	HST Available
(1)	(2)	(3)	(4)	(5)	(6)	(7)	(8)
A1185	NGC 3550	11:10:38.4	+28:46:04	0.035094	0.703	✓	—
A1187	2MASX J11110955+3935522	11:11:09.6	+39:35:53	0.078380	1.492	✓	—
A1190	MCG+07-23-031	11:11:43.6	+40:49:15	0.078150	1.488	✓	—
A1203	2MASX J11134824+4017083	11:13:48.2	+40:17:09	0.075510	1.442	✓	—
A1213	2MASX J11162274+2915086	11:16:22.7	+29:15:09	0.045300	0.896	✓	—
A1218	2MASX J11184993+5144291	11:18:49.9	+51:44:30	0.079470	1.511	✓	—
A1228	UGC 6394	11:22:56.4	+34:06:42	0.042710	0.847	other	—
A1257	MCG+06-25-069	11:26:17.3	+35:20:25	0.034320	0.688	other	—
A1270	MCG+09-19-084	11:28:41.9	+54:10:21	0.070400	1.352	✓	—
A1275	2MASX J11292709+3638189	11:29:27.1	+36:38:19	0.060690	1.179	✓	—
A1279	2MASX J11313927+6714296	11:31:39.3	+67:14:31	0.054130	1.060	✓	—
A1314	IC 712	11:34:49.3	+49:04:40	0.033350	0.669	✓	—
A1324	LEDA 2557423	11:37:16.3	+57:06:49	0.117960	2.146	—	—
A1356	2MASX J11422978+1028327	11:42:29.8	+10:28:33	0.071612	1.374	✓	—
A1365	NVSS J114430+305259	11:44:30.5	+30:53:01	0.076260	1.455	✓	—
A1367	NGC 3842	11:44:02.1	+19:57:00	0.020830	0.424	✓	—
A1371	MCG+03-30-100	11:45:22.2	+15:29:44	0.068220	1.314	M2	—
A1400	2MASS J11520578+5458171	11:52:05.7	+54:58:18	0.060070	1.168	other	—
A1413	MCG+04-28-097	11:55:18.0	+23:24:18	0.142800	2.527	—	✓
A1423	2MASX J11574738+3342438	11:57:47.3	+33:42:44	0.080010	1.520	✓	—
A1424	MCG+01-31-003	11:57:28.9	+05:05:21	0.080446	1.528	✓	—
A1435	MCG+02-31-009	12:00:14.3	+10:41:49	0.061220	1.189	—	—
A1436	MCG+09-20-056	12:00:13.8	+56:15:03	0.067212	1.296	M2	—
A1452	MCG+09-20-071	12:03:07.1	+51:40:31	0.065544	1.266	M2	—
A1507	NGC 4199A	12:14:48.6	+59:54:23	0.060070	1.168	✓	—
A1516	2MASX J12185235+0514443	12:18:52.3	+05:14:45	0.078342	1.491	—	—
A1526	2MASX J12214375+1345168	12:21:43.8	+13:45:17	0.081740	1.550	—	—
A1534	MCG+10-18-041	12:24:42.7	+61:28:15	0.070010	1.345	✓	—
A1569	2MASX J12362580+1632181	12:36:25.7	+16:32:19	0.068464	1.318	other	—
A1589	MCG+03-32-083	12:41:17.4	+18:34:29	0.071800	1.377	✓	—
A1610	IC 822	12:47:45.5	+30:04:39	0.060622	1.178	✓	—
A1656	NGC 4874	12:59:35.7	+27:57:34	0.023100	0.469	M2	✓
A1668	IC 4130	13:03:46.6	+19:16:18	0.063510	1.230	✓	—
A1691	MCG+07-27-039	13:11:08.6	+39:13:37	0.072300	1.386	✓	—
A1749	IC 4269	13:29:21.0	+37:37:23	0.055785	1.090	✓	—
A1767	MCG+10-19-096	13:36:08.3	+59:12:24	0.071062	1.364	✓	—
A1775	MCG+05-32-063	13:41:49.1	+26:22:25	0.075460	1.441	✓	✓
A1795	MCG+05-33-005	13:48:52.5	+26:35:35	0.063550	1.231	✓	✓
A1800	UGC 8738	13:49:23.5	+28:06:27	0.078288	1.490	✓	—
A1809	2MASX J13530637+0508586	13:53:06.4	+05:09:00	0.078850	1.500	✓	—
A1812	2MASX J13522099+3730370	13:52:21.0	+37:30:38	0.061810	1.199	—	—
A1825	UGC 8888	13:58:00.4	+20:37:57	0.062135	1.205	✓	—
A1828	2MASX J13581472+1820457	13:58:14.7	+18:20:47	0.064913	1.255	✓	—
A1831	MCG+05-33-033	13:59:15.1	+27:58:35	0.076110	1.452	✓	—
A1890	NGC 5539	14:17:37.7	+08:10:47	0.058180	1.134	✓	—
A1899	MCG+03-37-008	14:21:41.7	+17:45:09	0.056445	1.102	✓	—
A1904	MCG+08-26-024	14:22:10.2	+48:34:15	0.070980	1.363	✓	—
A1913	2MASX J14263943+1641139	14:26:39.4	+16:41:15	0.053610	1.050	other	—
A1982	MCG+05-35-020	14:51:14.4	+30:41:33	0.056322	1.100	✓	—
A1983	MCG+03-38-044	14:52:55.3	+16:42:11	0.044764	0.886	M2	✓
A2022	MCG+05-36-002	15:04:15.9	+28:29:48	0.058189	1.134	✓	—
A2029	IC 1101	15:10:56.1	+05:44:42	0.077900	1.484	✓	✓
A2052	UGC 9799	15:16:44.5	+07:01:18	0.034470	0.691	✓	✓
A2061	2MASX J15212054+3040154	15:21:20.6	+30:40:16	0.078820	1.499	✓	—
A2063	MCG+02-39-020	15:23:05.3	+08:36:34	0.034170	0.685	✓	—
A2065	MCG+05-36-020	15:22:24.0	+27:42:52	0.069020	1.328	✓	—
A2107	UGC 9958	15:39:39.0	+21:46:58	0.042060	0.835	✓	—
A2122	UGC 10012	15:44:59.0	+36:06:35	0.066210	1.278	✓	—
A2147	UGC 10143	16:02:17.0	+15:58:29	0.035380	0.708	✓	✓
A2151	NGC 6041	16:04:35.8	+17:43:18	0.035100	0.703	✓	—
A2152	MCG+03-41-095	16:05:29.2	+16:26:10	0.044440	0.880	✓	—
A2162	NGC 6086	16:12:35.5	+29:29:06	0.031900	0.641	✓	—

Table 1
(Continued)

Cluster	BCG	R.A. (J2000)	Decl. (J2000)	z	Angular Scale (kpc arcsec ⁻¹)	L14 Selection	HST Available
(1)	(2)	(3)	(4)	(5)	(6)	(7)	(8)
A2197	NGC 6173	16:29:44.9	+40:48:42	0.029380	0.592	✓	✓
A2199	NGC 6166	16:28:39.1	+39:33:11	0.030920	0.622	✓	✓
A2247	UGC 10638	16:50:58.6	+81:34:30	0.038809	0.774	M2	—
A2248	2MASX J16573834+7703462	16:57:38.4	+77:03:46	0.065641	1.268	M2	—
A2255	2MASX J1712287+640338	17:12:28.8	+64:03:39	0.073440	1.406	—	—
A2256	UGC10726	17:04:27.1	+78:38:26	0.059170	1.152	✓	—
A2271	MCG+13-12-022	17:18:16.6	+78:01:07	0.057439	1.120	✓	—
A2293	2MASX J18012131+5739016	18:01:21.3	+57:39:02	0.073396	1.405	M2	—
A2308	2MASX J18340865+7057188	18:34:08.5	+70:57:20	0.083424	1.579	✓	—
A2319	MCG+07-40-004	19:21:10.0	+43:56:45	0.054588	1.068	—	—
A2388	LEDA 140981	21:53:39.3	+08:15:10	0.061500	1.194	✓	—
A2469	—	22:40:34.3	+12:17:56	0.065600	1.267	other	—
A2495	MCG+02-58-021	22:50:19.7	+10:54:13	0.080060	1.521	✓	✓
A2506	NGC 7432	22:58:01.9	+13:08:05	0.025464	0.516	—	—
A2513	NGC 7436	22:57:57.5	+26:09:01	0.024600	0.499	—	—
A2516	2MASX J23001449+1835027	23:00:14.5	+18:35:03	0.081825	1.551	—	—
A2524	2MASX J23031792+1740232	23:02:55.8	+17:45:01	0.081490	1.546	✓	—
A2558	2MASX J23124349+1021435	23:12:43.5	+10:21:44	0.064900	1.255	✓	—
A2572	NGC 7597	23:18:30.2	+18:41:21	0.037540	0.749	other	—
A2589	NGC 7647	23:23:57.4	+16:46:38	0.041170	0.818	✓	✓
A2593	NGC7649	23:24:20.0	+14:38:50	0.042042	0.835	✓	✓
A2618	2MASX J23340547+2259000	23:34:05.5	+22:59:00	0.072813	1.395	✓	—
A2622	2MASX J23350151+2722203	23:35:01.5	+27:22:21	0.063441	1.229	✓	—
A2625	2MASX J23374932+2048340	23:37:49.3	+20:48:34	0.059118	1.151	✓	—
A2626	IC 5338	23:36:30.6	+21:08:51	0.055108	1.078	✓	✓
A2630	2MASX J23380105+1554022	23:38:01.0	+15:54:02	0.068170	1.313	other	—
A2634	NGC 7720	23:38:29.4	+27:01:54	0.030350	0.611	✓	✓
A2637	2MASX J2338533+212752	23:38:53.3	+21:27:53	0.073702	1.410	✓	—
A2657	2MASX J23445742+0911349	23:44:57.4	+09:11:36	0.041081	0.817	M2	✓
A2665	MCG+01-60-039	23:50:50.5	+06:08:59	0.056100	1.096	✓	—
A2666	NGC 7768	23:50:58.5	+27:08:51	0.026955	0.545	✓	✓
A2675	2MASX J23554260+1120355	23:55:42.6	+11:20:36	0.076893	1.466	✓	—
A2678	2MASX J23554532+1139135	23:55:45.3	+11:39:14	0.078125	1.487	M2	—
AWM1	NGC 2804	09:16:50.0	+20:11:55	0.027670	0.559	—	—
AWM5	NGC 6269	16:57:58.1	+27:51:16	0.034891	0.699	—	—
AWM7	NGC 1129	02:54:25.2	+41:34:37	0.017639	0.361	—	✓
L2027	LEDA 1479941	00:43:11.8	+15:16:03	0.078650	1.497	—	—
L2030	NGC 7237	22:14:46.9	+13:50:28	0.026180	0.530	—	—
L2069	2MASX J01072180+1416240	01:07:21.8	+14:16:24	0.078512	1.494	—	—
L2093	2MASX J01092719+1415359	01:09:27.2	+14:15:37	0.060780	1.181	—	—
L2211	NGC 7651	23:24:26.0	+13:58:21	0.042460	0.843	—	—
L3009	2MASX J09204890+4039516	09:20:48.8	+40:39:52	0.072690	1.393	—	—
L3055	2MASX J07464283+3059493	07:46:42.9	+30:59:50	0.056850	1.109	—	—
L3152	NGC 6338	17:15:22.9	+57:24:41	0.027300	0.552	—	✓
L3186	2MASX J17153003+6439511	17:15:30.0	+64:39:52	0.079040	1.503	—	—
MKW4	NGC 4104	12:06:39.0	+28:10:29	0.028605	0.577	—	—

Note. Cluster names beginning with “AWM,” “L,” and “MKW” are taken from the Albert et al. (1977), Von Der Linden et al. (2007), and Morgan & Lesh (1965) catalogs, respectively. A comparison to the BCG selection by Lauer et al. (2014, hereafter L14) is given in column (7). The items stand for agreement (✓), our BCG choice is the second-ranked galaxy L14 (M2), or the cluster is not present in L14 (—) and our choice is neither the first- nor the second-ranked galaxy in L14. The last column states whether *Hubble Space Telescope* images were used to increase the spatial resolution of the inner light profiles.

line-of-sight overlap (three cases); (2) there is disagreement on the distance to the cluster center, usually in the case of ongoing mergers of clusters (four cases); (3) the BCG is fainter in the metric aperture but brighter in terms of total luminosity (eight cases); (4) the criteria “brightest in the metric aperture” and “most extended” stand in conflict with each other (11 cases); and (5) the criteria “brightest in the metric aperture” and “central” stand in conflict with each other (three cases). The

sometimes-occurring conflict between “brightest” and “central” was also pointed out by Von Der Linden et al. (2007).

3. Data

The observations have been carried out with the 2 m Fraunhofer telescope at the Wendelstein Observatory. It is located in the Bavarian Alps, 70 km southeast from Munich,

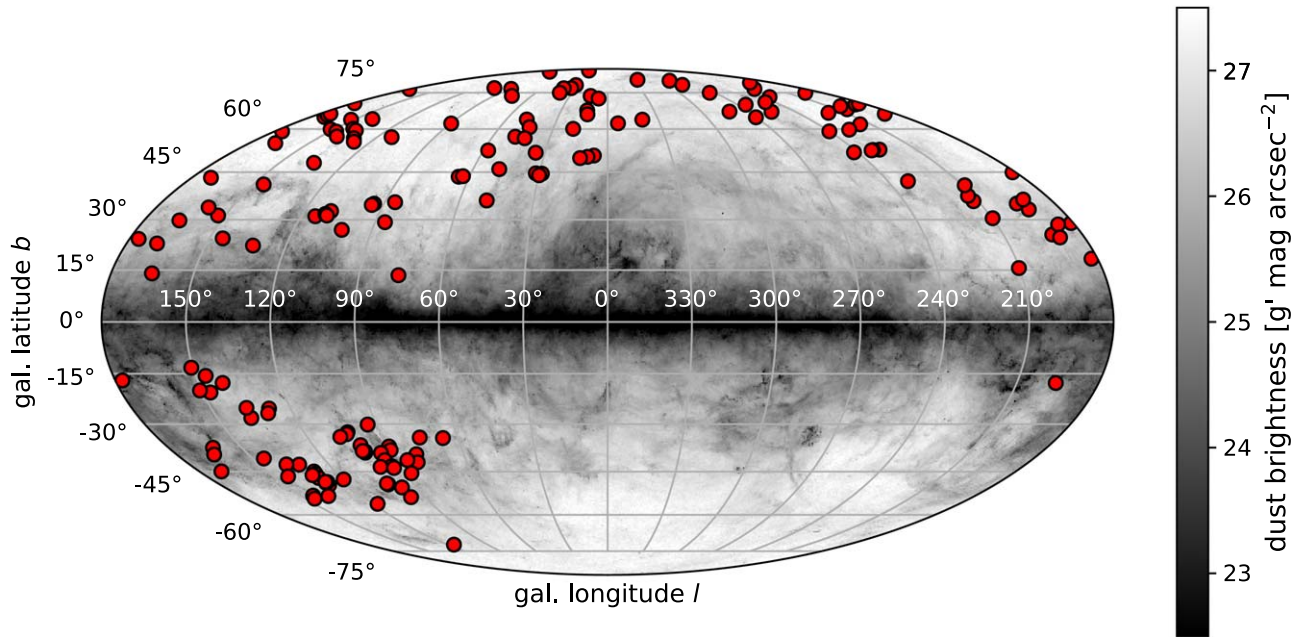


Figure 2. Our sample. The observed galaxy clusters are marked as red points. The background is the far-infrared dust emission map from Planck Collaboration et al. (2014). It is scaled to match the emission of the galactic cirrus (see Section 5.2).

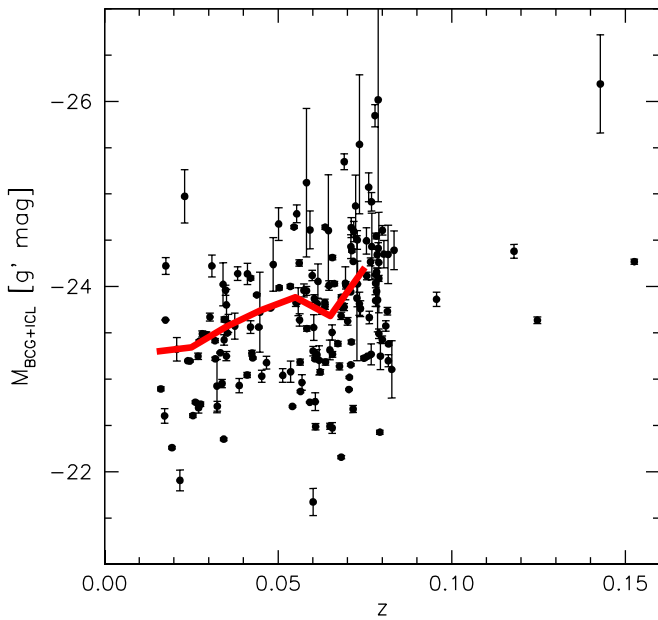


Figure 3. Redshift z of the BCG plotted against the total brightness of the BCG + ICL $M_{\text{BCG+ICL}}$ measured in this paper. The red line shows the average brightness in each redshift bin with width $\Delta z = \pm 0.005$. Four outliers with $M_{\text{BCG+ICL}} < -27$ g' mag were neglected because total brightness depends heavily on the extrapolation of the upward-curved light profiles that are unlikely to continue to infinite radius.

Germany. The telescope is a modern Alt-Az instrument that has been in operation since late 2013. We have utilized the Wendelstein Wide Field Imager (WWFI; Kosyra et al. 2014) for our survey as its first light instrument. Its optical components are designed to minimize ghost intensities (Hopp et al. 2014), which qualifies the setup well for a deep imaging study.

The field of view with $27'.6 \times 28'.9$ in combination with the large dither pattern is wide enough to cover the ICL down to an

SB of 30 g' mag arcsec $^{-2}$ while still providing sufficient sky coverage (see Figure 4, left panel) to model the background accurately. That corresponds to a median semimajor axis radius of $a = 350 \pm 128$ kpc for our sample.

The camera consists of four 4096×4109 pixel e2v CCD detectors installed in a camera by Spectral Instruments. The detectors are aligned in a 2×2 mosaic (see Figure 5). On the sky, the gaps between the CCDs are $98''$ in the north–south direction and $22''$ in the east–west direction. A large 52-step dither pattern is chosen for the observations to fill up the gaps and provide sufficient sky coverage. It is illustrated in Figure 4. For the first four exposures, the BCG is centered on each CCD, then shifted by two arcminutes in the R.A. or decl. direction before repeating the four exposures off-center. That procedure is repeated 13 times whereby the shifting direction changes for each step. In other words, the dither pattern is a 13-step spiral where each step is repeated on all four CCDs. This strategy allows us to model any time-stable background pattern accurately, which is especially important near the location of the BCG. The total integration time per target is 52 minutes and is split into 60 s single exposures.

We have chosen the g' band for all observations because the night-sky brightness is more stable in that filter band compared to redder bands, due to the absence of strong emission lines. The fact that optical reflections have lower intensities is also important.

The pixel scale of $0''.2/\text{pixel}$ oversamples the seeing-limited data. The typical seeing of $\text{FWHM} \simeq 1.2 \pm 0''.2$ allows us to resolve the inner cores of BCGs after deconvolving the central image regions. If available, we use high-resolution *Hubble Space Telescope* imaging data downloaded from the Hubble Legacy Archive (<https://hla.stsci.edu>) to measure the central light profiles and combine them with the profiles measured from wide-field WWFI data.

As the main interest of this work is the faint outskirts of BCGs, the observing constraints were prioritized more on dark and photometric conditions than on excellent seeing. Hence,

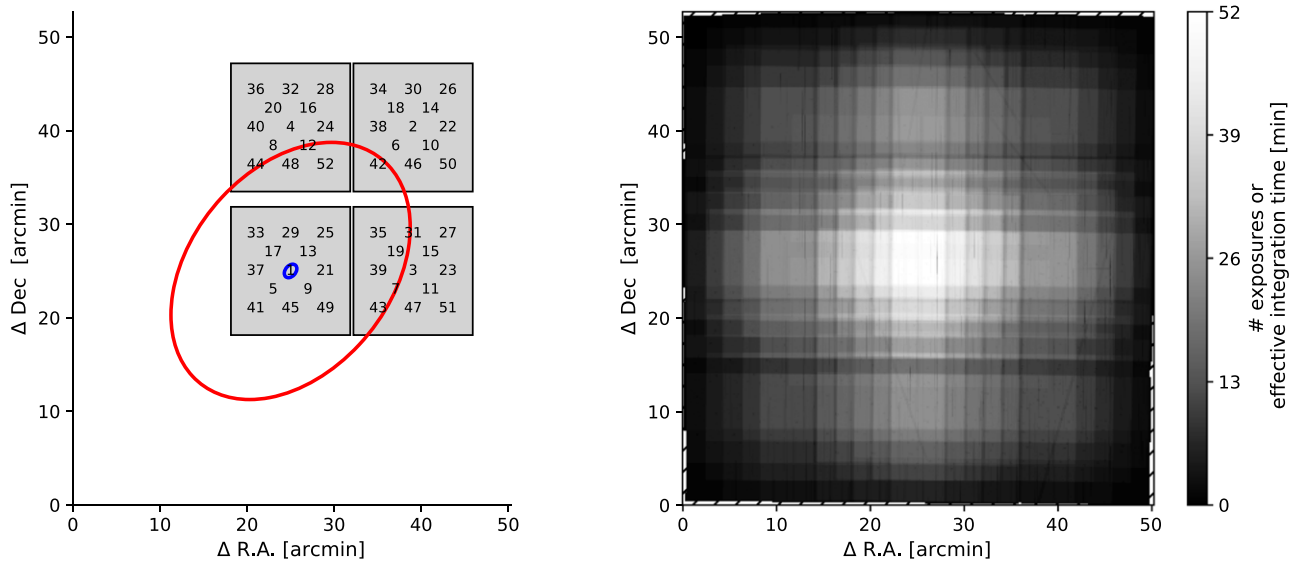


Figure 4. Left: illustration of the dither pattern. The four CCDs are represented by gray squares. The illustrated pointing corresponds to the first element of the dither pattern. The position of the BCG on the detectors is indicated by the number $1 \leq i \leq 52$ for each dither element i . Blue and red ellipses correspond to the isophotes with $SB = 30 \text{ g' mag arcsec}^{-2}$ for the apparently smallest BCG, A2630 (semimajor axis radius $a = 50''$), and the apparently largest BCG, A1367 ($a = 955''$), respectively, that were observed with this dither pattern. Right: stacked weight file of A600. The spatially dependent number of exposures that were added are color coded.

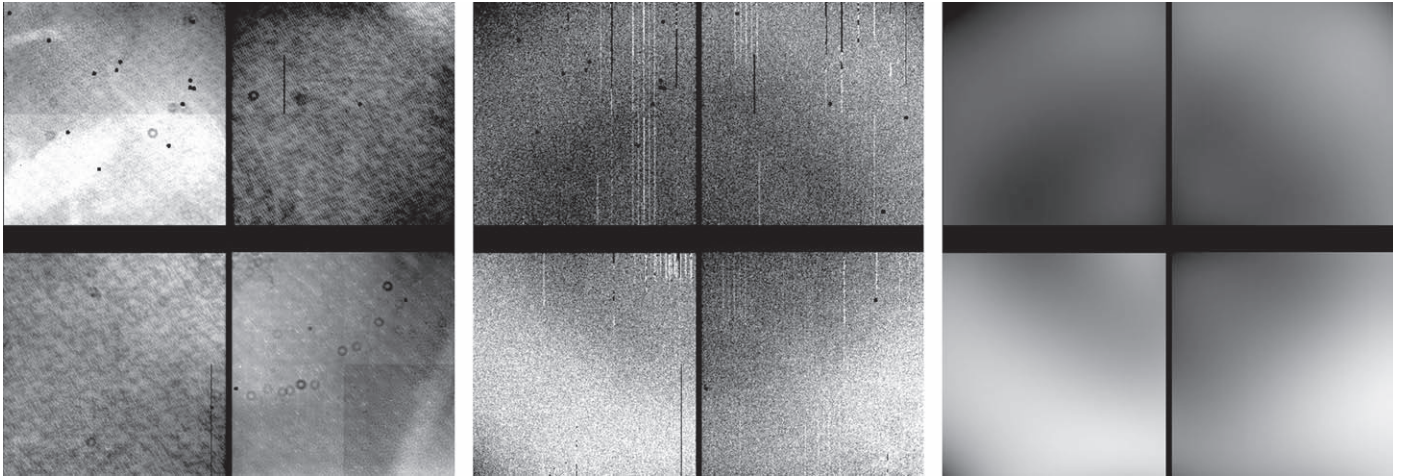


Figure 5. Left: example master flat in the g' band. Variations are on the 3% level. Middle panel: example night-sky flat, also in the g' band. Variations are on the 2% level. Charge persistence stripes are visible as vertical white lines. Right panel: fit of the night-sky flat with 2D fourth-order polynomials for each of the four CCDs.

the median seeing for our survey is worse than the median site seeing of $0''.8$ reported by Hopp et al. (2008).

3.1. Data Reduction

The data reduction pipeline was specifically developed and assembled for the WWFI. It includes bias subtraction, flat-fielding, charge persistence, bad pixel and cosmic-ray masking, photometric zero-point calibration, background subtraction, bright star removal, resampling, and coadding. The photometric zero-points are calibrated using Pan-STARRS1 DR2 catalogs (Flewelling et al. 2016) and provide SB profiles consistent with the Sloan Digital Sky Survey (SDSS). A comparison of 10 BCG SB profiles with those measured from SDSS DR12 image data shows that the SB profiles agree within $0.02 \text{ mag arcsec}^{-2}$ before point-spread function (PSF) debroadening correction. Dark current is negligible at the low CCD operating temperature

of -115°C . Detailed descriptions of all important aspects regarding deep surface photometry follow in the next subsections.

3.1.1. Bias

Bias exposures show a chess field-like pattern. Each of the 16 readout amplifiers places a unique bias offset on the corresponding data region. A time-stable vertical line pattern is hidden beneath these offsets. To get rid of this line pattern, we subtract a master-bias image that was created by averaging all the bias images taken in the relevant month. The offsets are subtracted beforehand. Cosmic rays are removed with the tool *cosmicfits* (Gössl & Riffeser 2002).

The values of the offsets themselves are not stable over time. They fluctuate mildly on minute timescales. We measure ~ 0.1 ADU residuals even after the clipped average of the corresponding overscan regions had been subtracted. The origin of this

effect could be a heating up of the readout electronics, which is correlated to the number of charges being read out. An alternative explanation is based on electromagnetic interferences from a nearby transmitting antenna. In order to eliminate the varying offsets from the science images, we match the background fluxes along 30-pixel-wide adjacent stripes along the borders of each quadrant to the average value of these stripes. This is done for each CCD independently. Regions affected by charge persistence are masked beforehand in order to dismiss contaminated pixels (see Section 3.1.3).

3.1.2. Flat-fielding

We correct for large-scale illumination inhomogeneities and small-scale patterns like dust using calibration images that were taken each night during twilight. These twilight flats are flux-aligned with fourth-order polynomials to each other and then combined into a master flat (Figure 5, left panel). Every bias-subtracted science image is divided by this master flat. However, large-scale residuals on a 2% level remain (Figure 5, middle panel). That is common for wide-field imagers. The residual patterns are almost (but not perfectly!) point-symmetric around the center and stable for one pointing in one night. We have identified three properties of this pattern that point toward a color effect as its origin: (1) the closer to dark time the flats are taken, the weaker is the pattern structure; (2) it is weaker in narrowband filters; (3) the quotient of two exposures that were taken while first a green and second a red LED illuminated the inner dome shows a similar pattern with $\sim 2\%$ large-scale variation.

We conclude that the bluer color of the twilight sky compared to the redder night sky, in combination with color-dependent stray light originating inside the optical path, led to inhomogeneities in the flat-fielding process. No improvement in flatness was accomplished by using dome flats instead of twilight flats. Even though the chosen lamp produced redder light than the twilight sky, the difficulty of illuminating a large inner dome surface homogeneously from a short distance limits the possibility of achieving perfect flatness.

The multiplicative scaling of the flat-field pattern correlates positively with the night-sky brightness. Color changes toward a bluer night sky that are due to airglow, city lights, or lunar twilight invoke an inversion of the pattern. We factor in that behavior by scaling night-sky flats (NSFs) accordingly (see Equation (6) in Section 3.1.5).

3.1.3. Charge Persistence Masking

Bright foreground stars from the Galaxy are unavoidable in all observed fields, especially due to the wide field of the WWFI camera. The extreme numbers of photons arriving from these stars trigger a tremendous release of free electrons into the valence band of the CCD detector. A small fraction of them gets trapped inside defects in the silicon lattice. These trapped electrons are then released over time where the release rate follows a power law $\dot{N} \propto t^{-1}$. That process can last for hours, depending on the severity of saturation. After the trapped electrons are released, they are stored inside the pixels' potential wells until readout.

When the electrons are being shifted toward the readout register as part of the readout process, they temporarily affect the pixel values along their path. More precisely, the electron bulk loses a fraction in lattice defects of the pixels along the readout direction. Many of these secondarily trapped electrons

are released over the first 2 μs , which is the length of a readout step. As a result, a saturation stripe appears in the same exposure where saturation happened, but opposite to the shifting direction. Another charge persistence stripe appears in subsequent exposures in the shifting direction because the damaged pixels slowly release the remaining trapped electrons (see Figure 5, middle panel). Over time, these artificial signals contaminate an increasing fraction of the total field of view because of the dithering strategy.

Our masking strategy is to store the locations where stars saturated and check the corresponding stripes' background flux relative to the ± 15 -pixel-wide areas alongside them. The charge persistence stripe is being masked when the contaminating signal is higher than the local background plus 0.2 times the rms background scatter. The factor 0.2 was empirically determined to minimize false-positive detections. The location information of a positive detection is forwarded to the subsequent images until the stripe is no longer detectable.

3.1.4. Bright Star Removal

Bright foreground stars have to be removed from the images for two reasons. Some of the PSFs' extended wings (see Figure 6 and, e.g., Kormendy 1973) overlap in projection with the targeted ICL, and they furthermore complicate the background modeling. We follow the strategy from Slater et al. (2009) to model and subtract the ~ 100 brightest stars in the observed fields. Their approach has been successfully applied for the Burrell Schmidt Deep Virgo Survey (Mihos et al. 2017). Duc et al. (2015) and later Karabal et al. (2017) performed a similar correction for the MATLAS survey data, but with time-consuming manual modeling.

We split the cleaning procedure into two steps. First, we subtract the circular PSF light profile from every star, and second, we model and subtract the out-of-focus reflections, which are location dependent. The circularly symmetric light profile for a zeroth magnitude star is shown in Figure 6. It spans $\sim 14'$ in radius and $\sim 19 g'$ mag arcsec $^{-2}$ dynamic range in surface brightness. The blue line is a Moffat (1969) fit to the core and depends on the seeing. The outer components are time-stable because they are due to the optics. Surprisingly, they can be modeled by three $r^{1/4}$ profiles. The outermost $r^{1/4}$ component is extrapolated to the edge of the field of view. We are mostly interested in removing the wings accurately. A single PSF model is therefore sufficient for all observations. The analytic SB profile shown by the red line in Figure 6 is used to model all stars that are listed in the Tycho-2 catalog (Høg et al. 2000) and located inside of a circular aperture with radius $r < 1.3$ around the center of the field. Stellar magnitudes are converted from the Tycho B_T and V_T to the Johnson B_J and V_J filter system using Equation (1.3.20) from ESA (1997):

$$V_J = V_T - 0.09(B - V)_T, \quad (1)$$

$$(B - V)_J = 0.85(B - V)_T \quad (2)$$

and are then converted to SDSS g -band magnitudes using the equation derived by Jester et al. (2005):

$$g = V_J + 0.60(B_J - V_J) - 0.12. \quad (3)$$

Our photometric zero-points are calibrated to the Pan-STARRS photometric filter system. The difference between SDSS g and Pan-STARRS g' magnitudes (e.g., $g - g' = 0.09$ for the Sun; Willmer 2018) is not relevant here because the reference g' -band PSF SB profile is assigned its g -band catalog

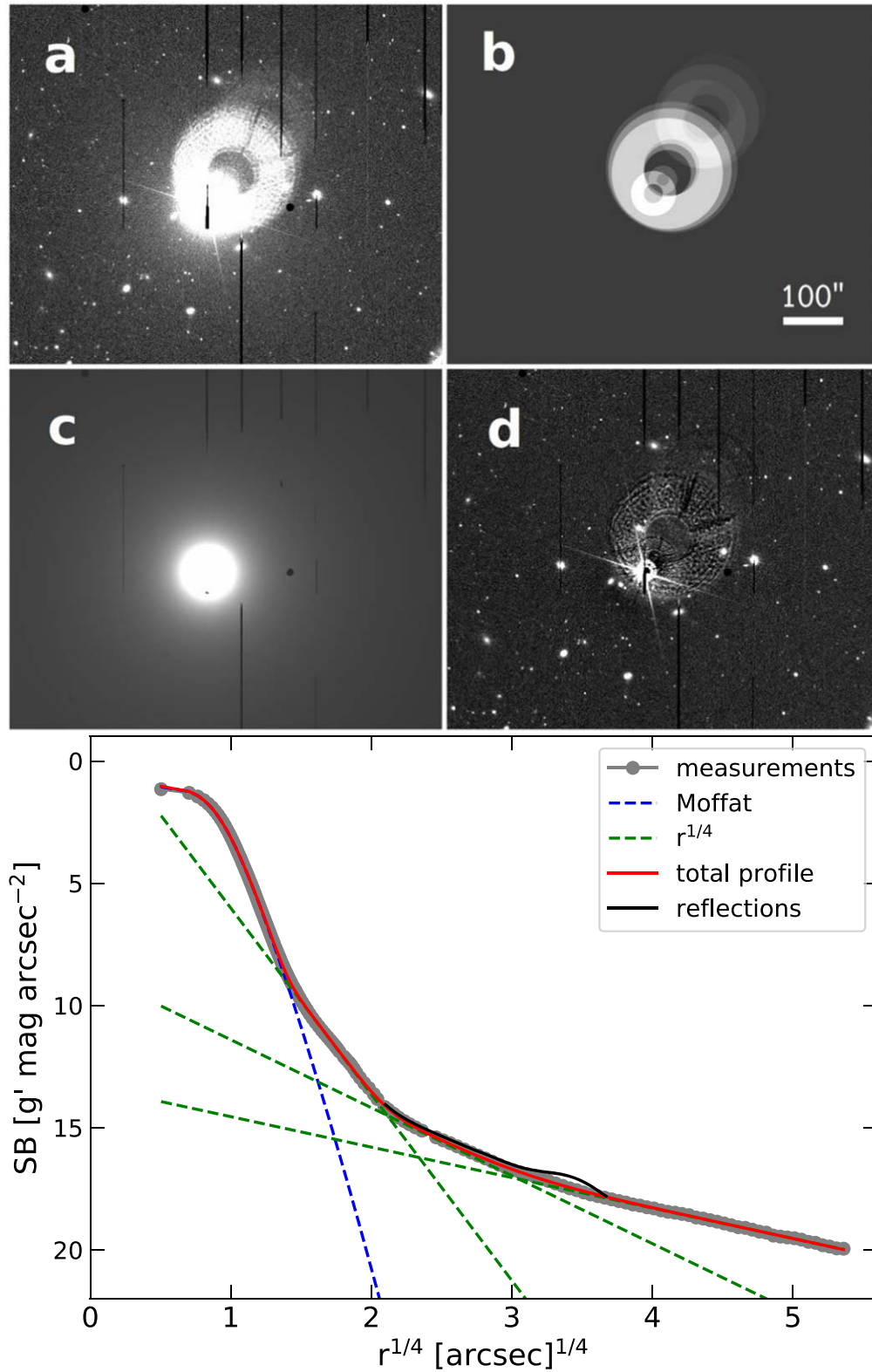


Figure 6. Top panel: (a) example cutout of a bright star, (b) model of the ghosts, (c) model of the point-symmetric component of the PSF, (d) residual after subtracting both models. Bottom panel: SB profile of a zeroth magnitude star. The multicomponent fit to the data points is shown as a red line and is used for the modeling. The FWHM of the Moffat fit (blue dashed line) to the central region is $\text{FWHM} = 1''.05$. The outer three $r^{1/4}$ components (green dashed lines) are formed by the optical elements in the telescope. The contribution from the reflections is plotted separately as the black line.

magnitude. It is scaled for different stars according to their g -band magnitudes. However, the uncertainties of the color transformations propagate an error to the individual scaling of the model stars. Further relevant effects are intrinsic stellar

variabilities and the uncertainty of the preliminary photometric zero-point calibration at that intermediate step of the data reduction. We want to minimize the average residuals of the brightest stars. That is achieved by introducing an empirically

Table 2
Reflection Properties for a Zeroth Magnitude Star

j	s	r_{outer} (arcsec)	SB (g' mag arcsec $^{-2}$)
1	0.04371	37.4	17.03
2	0.08649	23.8	17.98
3	0.10602	92.6	17.28
4	0.11811	102.6	17.40
5	0.12555	109.6	18.22
6	0.26040	74.0	19.12
7	0.28365	87.6	19.12
8	0.31713	86.4	20.04

Note. The relative shift s , given in column (2), is defined in Equation (4) as the center offset of a ring with respect to the source divided by its distance from the optical axis. The outer radius of each reflection ring j is given in column (3). The inner radius is always $r_{\text{inner}} = 0.424r_{\text{outer}}$. The surface brightness normalized to a zeroth magnitude star of each ring is given in column (4).

determined scaling factor f_{scaling}^i for all stars in each cluster pointing i . Our manual choices vary in $0.9 \lesssim f_{\text{scaling}}^i \lesssim 1.1$.

Reflections are considered separately. They are particularly prominent in wide-field imagers, due to the need for multiple corrector optics in order to correct for field distortions. They arise from light that is reflected at various surfaces during its path through the telescope system. These surfaces are the front and back sides of filter glasses, corrector lenses, and the CCD entrance window. The longer path lengths result in out-of-focus duplicates next to bright light sources, so-called ghosts (Figure 6, top panel). For the WWFI g' band, we calculate that 1.78% of the PSF's light is redistributed into these ghosts, which is consistent with the findings of Hopp et al. (2014). We identify eight rings with parameters listed in Table 2. The rings are only concentric if the light source is located on the optical axis, that is, close to the field center. They are shifted radially outward in any other case. The relative shift s of ring j is in good approximation linearly dependent on the distance of the star at position \mathbf{r}_{star} from the optical axis at position \mathbf{r}_{oa} :

$$\mathbf{r}_j = \mathbf{r}_{\text{star}} + s \cdot (\mathbf{r}_{\text{star}} - \mathbf{r}_{\text{oa}}^{q_i}) \quad (4)$$

with

$$\begin{aligned} \mathbf{r}_{\text{oa}}^{q_1} [\text{px}] &= (4011, 4162), \\ \mathbf{r}_{\text{oa}}^{q_2} [\text{px}] &= (4007, -433), \\ \mathbf{r}_{\text{oa}}^{q_3} [\text{px}] &= (-195, -443), \\ \mathbf{r}_{\text{oa}}^{q_4} [\text{px}] &= (-195, 4159) \end{aligned} \quad (5)$$

being the position of the optical axis in the coordinate system of each CCD q_i . The central coordinates of the rings are \mathbf{r}_j . The outer radii r_{outer} are tabulated in Table 2. The inner radii are always $0.424r_{\text{outer}}$, corresponding to the shaded area of the support for the secondary mirror. The surface brightness of the ring j is $\text{SB}_j + g'$ for a star with a g' -band magnitude g' . The values for SB_j are given in Table 2 and are estimated by scaling the brightness of each ring model independently so that the total residual after subtraction is minimal.

3.1.5. Background Subtraction

After flat-fielding, large-scale variations in the background pattern are apparent on a 2% level (see Figure 5, middle panel). That corresponds to a surface brightness of $\text{SB} \sim 26 \text{ } g' \text{ mag arcsec}^{-2}$. In order to measure accurate SBs at the $30 \text{ } g' \text{ mag}$

arcsec $^{-2}$ level, the background has to be flat on the same level. The necessary calibration has to be performed on the individual images because the dithering between observations would otherwise result in sharp-edged jumps in the background pattern of the coadded mosaic.

The delicacy for every background subtraction method lies in the risk of accidentally subtracting the incompletely masked ICL, which mimics an artificial background pattern. The easiest method to follow would be simple surface polynomial or surface spline fitting (e.g., Capaccioli et al. 2015) of the source-masked images. We have discarded this approach because of its severe risk of subtracting part of the ICL. This method is furthermore fairly unstable when the polynomials or splines are unconstrained, due to large masks. This can lead to over-shooting, especially when an edge of the image is masked. A detailed explanation of our masking procedure is given in Section 3.2.

We apply the more robust method of subtracting an average model of the background pattern, a so-called NSF. This is only possible because the background pattern is to zeroth order time-stable (see Section 3.1.2). A separate NSF is created for every visit, that is, for each target in each night. The major advantage of this method is that the background pattern is known at and around the masked BCG. That is because masked regions in individual images are filled up in the NSF by averaging numerous dithered exposures. Moreover, the issue of incomplete masks is reduced because only a small number of images are contaminated by undetected PSF or galaxy halos at a specific, fixed image location, again thanks to the large dither pattern.

The NSF can either be created from separate sky pointings (Iodice et al. 2017; Spavone et al. 2017) or from the target pointings themselves. The first option is safer because the risk of including part of the ICL in the NSF is eliminated. The necessary observing strategy is, on the other hand, twice as time-consuming. We take advantage of the $\sim 4\times$ larger field of view compared to the extent to which we measure ICL. An optimized dithering strategy (see Section 3) ensures that the background can be determined from the target exposures themselves while maximizing the exposure time on-target and minimizing the contribution of the incompletely masked ICL on the NSFs.

The PSF-subtracted (see Section 3.1.4) and source-masked single images are normalized and averaged to an NSF. The normalization is necessary because fluctuations in the sky brightness on a 2% level are common between exposures, and the normalization is allowed since the background pattern is to first order multiplicative because of its origin in flat-fielding residuals (see Section 3.1.2).

A number of undetected charge persistence stripes usually become visible in the deep NSFs (see Figure 5, middle panel, and Section 3.1.3). We therefore fit two-dimensional fourth-order polynomials to each CCD region in order to improve the NSF smoothness (see Figure 5, right panel). The smoothed NSF is then rescaled in flux back to the individual images i from which it was created. The scaling formula is

$$\text{NSF}_i(x, y) = \text{NSF}(x, y) \times a_i + b_i. \quad (6)$$

We allow for an additive b_i and multiplicative a_i scaling. Two fitting parameters are needed to account for the gradual flipping of an outward-increasing to an outward-decreasing brightness of the background pattern as the night-sky color becomes bluer (see Section 3.1.2).

Every NSF is scaled slightly too high because incomplete masks are more present in the individual images than in the averaged NSF. That leads to a small, negative background constant on the order of negative $\sim 30 \text{ g' mag arcsec}^{-2}$ that remains in the coadded mosaics (see Section 5.1). This constant is later determined as the value to which the linear light profiles converge at large radii (see, e.g., Spavone et al. 2017).

3.2. Source Masking

Two situations require source masking: (1) before averaging images to create NSFs and (2) before measuring the BCG/ICL light profiles. Both situations require different masking techniques, but both resulting masks need to be as complete and on large scales as homogeneous as possible. Tools that are being used by other authors include the IRAF task `objmasks` (Mihos et al. 2017) or `EXAM` (Huang et al. 2011; Spavone et al. 2017), which is based on SExtractor (Bertin & Arnouts 1996) catalogs.

We have developed our own technique specifically to tackle the requirement of homogeneity. Our adopted, large dither pattern causes a spatially varying signal-to-noise ratio of $\Delta(S/N) > 2$. That is a severe problem for the choice of masking thresholds:

1. A constant signal masking threshold leads to a more frequent masking of noise peaks as false-positive detections in the low-S/N regions.
2. A constant S/N masking threshold leads to fewer detections of sources in the low-S/N regions.

While choice (1) results in a decrease of the average flux value in the low-S/N regions, choice (2) evokes the opposite. Both options therefore introduce a significant bias in the NSF scaling and isophotal flux measurements. A compromise between the two options, that is, a spatially dependent scaling of the masking threshold $T(x, y)$ by the square root of the local background rms scatter $\text{rms}(x, y)$, results in satisfyingly homogeneous masks for a low average masking threshold T_0 :

$$T(x, y) \geq T_0 \cdot \left(\frac{\sqrt{\text{rms}(x, y)}}{\text{median}(\sqrt{\text{rms}(x, y)})} \right). \quad (7)$$

The information of the local background noise $\text{rms}(x, y)$ is stored in the stacked weight maps generated by `SWarp` (see Figure 4, right panel, for an example).

We now explain our choices for the average masking thresholds for each of the two scenarios that were mentioned in the beginning of this subsection.

3.2.1. Masks for Background Modeling

The basis for this type of mask is a roughly background-subtracted, coadded image. This is in our case a mosaic that was created after subtracting second-order 2D polynomials from the masked single exposures. We mention here that this procedure is iterative. Since there can be no celestial sources with sizes smaller than the seeing, we smooth the stack using a 2D Gaussian filter with standard deviation $\sigma = 11 \text{ px}$ in order to avoid mask fragmentation. All pixels get masked that have greater values than the locally calculated threshold $T(x, y)$, where T_0 in Equation (7) corresponds to a surface brightness of $27.5 \text{ g' mag arcsec}^{-2}$. The regions around the BCG and around bright stars are conservatively enlarged by hand to a size where we expect the $29 \sim 30 \text{ g' mag arcsec}^{-2}$ isophote to be. We

again stress here that ICL residuals at these levels are damped in the NSF by averaging the widely dithered single exposures. That is confirmed by the recovery of a mock-BCG SB profile down to $SB > 30 \text{ g' mag arcsec}^{-2}$, as presented in Section 5.1.

3.2.2. Masks for Light Profile Measurements

Before measuring the flux from a BCG+ICL, we have to mask all other sources except for the BCG+ICL itself. Our approach to this problem is to subtract a model for the BCG+ICL before creating the mask. We exploit the fact that the BCG+ICL system is usually the largest object in the field of view and has the shallowest SB profile gradient. Thus, it can be approximately modeled by a medium-scale background fitting method. That model is created by performing a bicubic spline interpolation to a grid of points that was generated by calculating the clipped median in (51×51) pixel square apertures around the corresponding locations. After subtracting this model from the stack, we generate and combine one mask for the small and one mask for the medium-sized sources. The stack is smoothed with a 2D Gaussian filter with $\sigma = 5 \text{ px}$ (which is the typical seeing) for the first mask and $\sigma = 21 \text{ px}$ (which is about half of the background interpolation step size) for the second mask. All pixels are masked that have values greater than

$$T(x, y) \geq T_0 \cdot \text{rms}(x, y) \cdot \left(\frac{\sqrt{\text{rms}(x, y)}}{\text{median}(\sqrt{\text{rms}(x, y)})} \right)^{-1}, \quad (8)$$

where $T_0 = 0.15$ is given here in units of the local S/N per pixel. We emphasize here that the threshold is extremely low because of the preceding smoothing. Also note that the scaling term is now inverted because the threshold is expressed differently. The chosen threshold $T_0 = 0.15$ corresponds on average to a surface brightness of $27 \gtrsim T_0 \gtrsim 27.5 \text{ g' mag arcsec}^{-2}$ (see Figure 7, red label). We decided to fix the masking threshold this time in units of (scaled) S/N because it provides a more consistent mask homogeneity between stacks of different integration times. In practice, fainter average thresholds result to zeroth order in a higher residual background constant (see the horizontal lines in Figure 7, right panel). That is because the overall distribution of background galaxies is largely homogeneous on the spatial scales of the outermost isophotes. This constant is determined in any case during the measurement of the light profile and thus introduces no bias. A first-order effect of a too-faint masking threshold is a downward bending of the outer surface flux profile (see the slope of the residuals in Figure 7, right panel). That is due to the outward-decreasing signal-to-noise ratio, as explained in the beginning of this subsection. The fainter the threshold, the more sensitive the mask homogeneity becomes toward spatially varying S/N ratios. The effect is reduced by $\sim 50\%$ by the spatial scaling of the threshold T_0 (Equation (8)) but not fully eliminated. The downward bending also biases the background constant choice to too-low values. Both effects combined result in too-bright SB data points in $3.6 < (a[\text{arcsec}])^{1/4} < 5.5$ (empty triangles and filled squares in Figure 7, left panel). The same panel also shows that the SB profiles derived with masking thresholds $26 \lesssim T_0 \lesssim 27.5$ are consistent with each other. The explained effects are less important for shallower

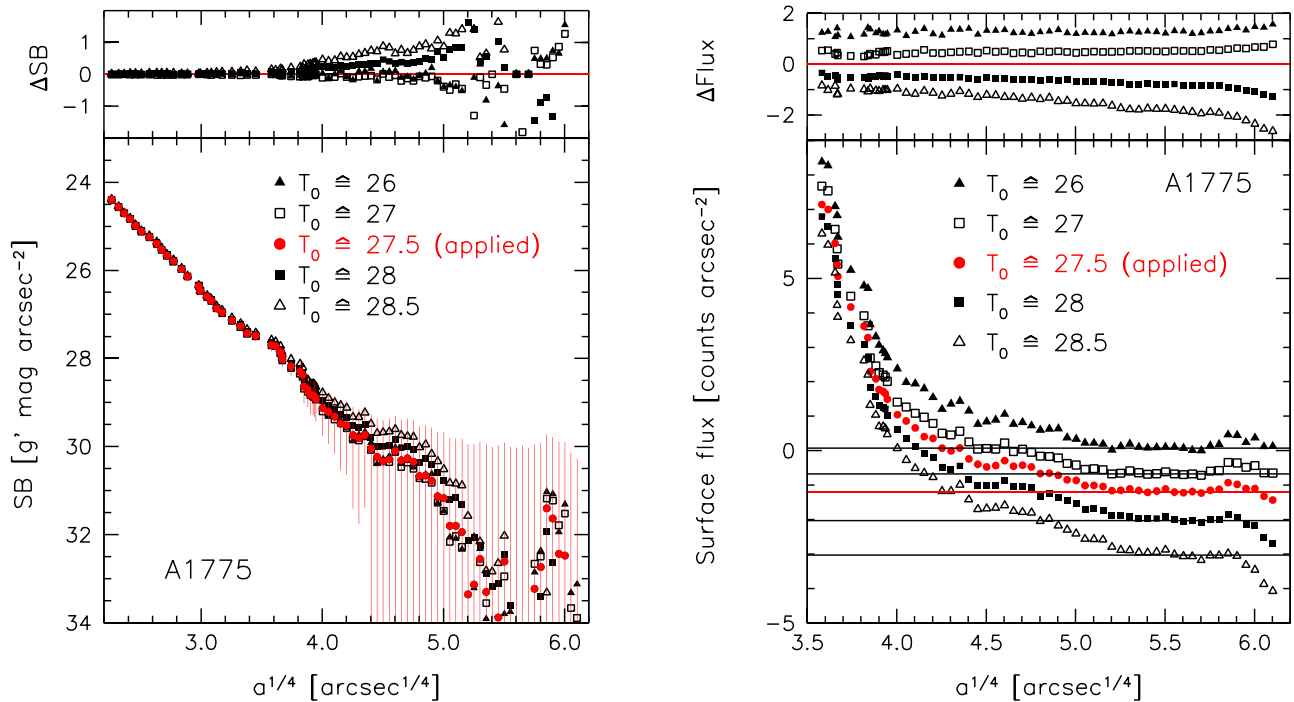


Figure 7. Surface brightness (left) and surface flux (right) profiles of the BCG in A1775 measured for different masking thresholds T_0 (Equation (8)) converted to units of g' mag arcsec $^{-2}$. The residual differences from the measurements done with the applied masking threshold (red) are shown in the top panels. The residual background choices are shown for each masking threshold as the horizontal lines in the right panel.

thresholds because fewer pixels are affected. The optimal threshold is therefore the faintest one that produces a surface flux profile that is still consistent with those derived with shallower thresholds. For the case of A1775, we find the optimal threshold to be $T_0 = 0.15 \hat{=} 27.5$ g' mag arcsec $^{-2}$.

The masks are expanded by convolving them with a circular kernel with radius $r = 9$ px for the first mask and $r = 11$ px for the second mask so that no light around small and medium-sized sources leaks visibly out of the expanded masks. The spline interpolation produces artifacts in the central areas of the BCG. We unmask and remask these regions by hand. Finally, the regions around bright and extended sources excluding the BCG+ICL are conservatively expanded by hand to a size where we expect the $29 \sim 30$ g' mag arcsec $^{-2}$ isophotes to be. The average masked fraction in the final masks is $33 \pm 5\%$.

3.3. Astrometry, Resampling, and Stacking

The astrometric solutions were calculated with SCAMP (Bertin 2006). The resampling and coadding of the calibrated images is performed with SWarp (Bertin 2010). The individual images are weighted by their inverse background rms scatter squared to obtain an optimal S/N for extended sources.

4. Surface Brightness Profiles and Isophotal Shape Parameters

4.1. Fitting Ellipses to the Isophotes

Azimuthally averaged surface brightness (SB) profiles of all BCGs are measured by fitting ellipses to the galaxies' isophotes with the code `ellfitn` from Bender & Moellenhoff (1987). All ellipses have five degrees of freedom: semimajor axis radius a , ellipticity $\epsilon = 1 - b/a$ where b is the semiminor axis radius, central coordinates X_0 and Y_0 , and position angle PA.

Deviations Δr_i of the i th isophote from a perfect ellipse are expanded in a Fourier series,

$$\Delta r_i = \sum_{k=3}^{19} [a_k \cos(k\theta_i) + b_k \sin(k\theta_i)], \quad (9)$$

where θ is the eccentric anomaly.

The routine breaks down usually around $SB \sim 27$ g' mag arcsec $^{-2}$, where the low-SB halos of satellite galaxies deform the ICL isophotes on the one hand, but too conservative masking on the other hand prevents the routine from finding enough sampling points for the ellipse fitting. In order to estimate the light profiles beyond that SB, we fix the isophotal shape parameters ϵ , PA, X_0 , and Y_0 for all ellipses that are larger than the one where the scatter in these parameters increases significantly. The semimajor axis radius for that ellipse is on average 207 ± 141 kpc with a median of 178 kpc. No isophotal parameters besides the flux are determined beyond this radius. The fluxes along all elliptical isophotes in the extended WWFI profiles are then determined by the method described in Section 4.2.

Systems with strong overlap between the BCG and satellite galaxies (e.g., A1656) are handled by mirroring parts of the uncontaminated side of the BCG on the contaminated side before measuring the isophotal shapes.

4.2. Isophotal Flux Measurement

The tools for the flux measurements are developed by us on the basis of Python scripts. They use the output isophotal shape tables that are provided by `ellfitn`. The flux along an isophote is measured in an elliptical annulus centered around that isophote. The annulus has a thickness of the average separation between two consecutive isophotes, calculated in $r^{1/4}$ units and evaluated at the isophotal radius. In other

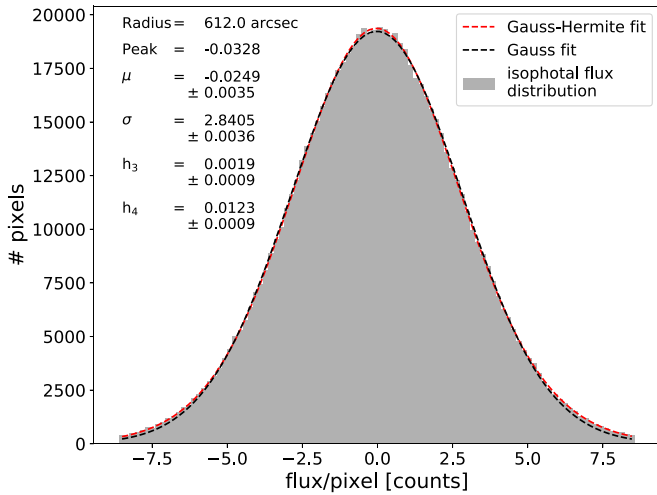


Figure 8. Pixel histogram of an example isophote with $SB = 30 \text{ g}' \text{ mag arcsec}^{-2}$. The flux units are calibrated for a pixel scale of $0''.2/\text{px}$ and a photometric zero-point of $ZP = 30 \text{ g}' \text{ mag}$. The Gaussian fit is overplotted as a black dashed line, and the Gauss-Hermite fit that includes two higher orders h_3 and h_4 is overplotted as a red dashed line. The value μ is used to calculate the SB of the isophote. The negative background constant is not yet subtracted here.

words, the annuli are not overlapping but all together cover the full area. We measure the isophotal flux by fitting a Gaussian with two higher-order moments (van der Marel & Franx 1993) to the pixel histogram (see Figure 8). The distribution is $\kappa - \sigma$ clipped on both sides at three times the standard deviation. The third and fourth Gauss-Hermite moments are given by

$$f(F) = A \exp(-0.5F^2) \times [1 + h_3(c_1F + c_3F^3) + h_4(c_0 + c_2F^2 + c_4F^4)], \quad (10)$$

where $F = (x - \mu)/\sigma$ with μ being the mean and σ being the standard deviation of the standard Gaussian. The normalization coefficient is A , and the other coefficients are given as $c_0 = \sqrt{6}/4$, $c_1 = -\sqrt{3}$, $c_2 = -\sqrt{6}$, $c_3 = 2\sqrt{3}/3$, and $c_4 = \sqrt{6}/3$. We use μ as the final value for the flux measurement.

The wings of the distribution are larger than what would be estimated from a simple Gaussian fit. Incompletely masked stellar halos, galactic outskirts, or cirrus introduce an asymmetry of the distribution toward more positive values, which we describe by the h_3 component. Noisier than average images are weighted less during coaddition. The result on the pixel histogram is similar to adding a second Gaussian component of low amplitude but with larger standard deviation to the high-S/N data. We quantify that behavior with the symmetric h_4 component.

The systematic errors in the light profile of the mock galaxy (see Section 5.1) were smallest when using the mean of the high order Gaussian μ as a robust estimator for the flux. We therefore calculate all SBs from this parameter.

A residual, negative background constant remains in every coadded mosaic (see Section 3.1.5). We estimate this constant as the value to which the linear light profile converges at large radii. An example is shown in Section 5.1. That constant is subtracted from all flux data points before these are converted into magnitudes.

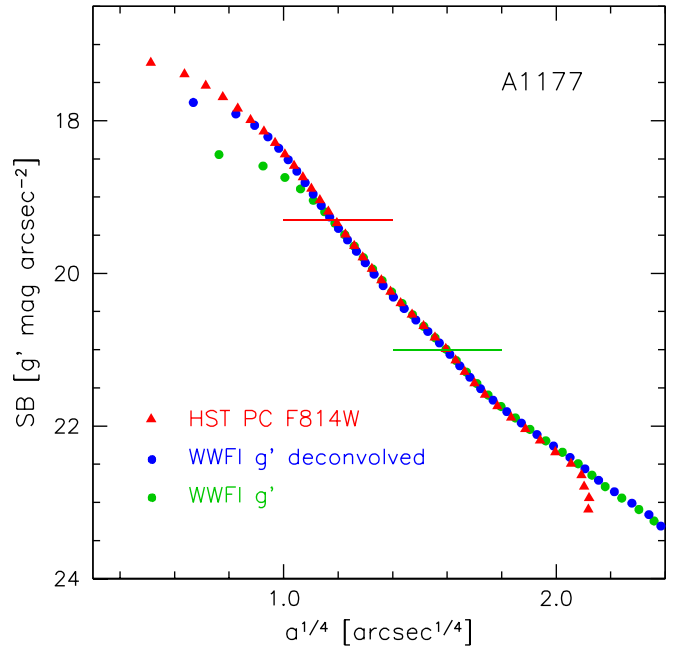


Figure 9. Inner light profile of NGC 3551 in A1177. The green and blue data points are obtained from WWFI data before and after deconvolution, respectively. The Nyquist sampling limit is reached at $a^{1/4} = 0''.8^{1/4} \cong 0''.4 = a$. The red data points are from archival *HST* data. The transition region between *HST* and nondeconvolved WWFI data is between the two horizontal lines.

4.3. Composite SB Profiles

To improve the spatial resolution of the inner light profiles, we deconvolve the innermost $80 \times 80''$ of our WWFI data using the MIDAS task `deconvolve/image`. The task uses 40 iterations of the Richardson-Lucy (1974) algorithm. If available (see Table 1), we use instead archival *Hubble Space Telescope* (*HST*) data in the filter band that is closest to the g' band. The background constant is poorly calibrated in the *HST* imaging data. We vary it manually until the inferred SB profile agrees best and over the largest radial interval with the WWFI-determined SB profile. The photometric zero-point of the *HST* data is also adjusted in the same way.

A transition region is defined for each light profile where both the *HST* or deconvolved WWFI profile and the extended WWFI profile overlap well (horizontal lines in Figure 9). Both profiles are merged in this transition region by weighted averaging of the data points.

The merging and replacing of the inner data points are done for all isophotal shape parameters.

4.4. Sérsic Fits

The Sérsic (1968) function is an empirical description for SB profiles of elliptical galaxies. It fits the semimajor-axis profile shapes of elliptical and spheroidal galaxies overwhelmingly well over a large radial range that, for most galaxies, covers 93%–99% of the total galaxies' light (Kormendy et al. 2009). It was first used to fit SB profiles of BCGs by Graham et al. (1996), who demonstrated its superiority to the hitherto preferentially used de Vaucouleurs ($n = 4$) profile because the Sérsic indices of BCGs are usually $n > 4$. The Sérsic function

is given by

$$SB(a) = SB_e + c(n) \cdot \left[\left(\frac{a}{a_e} \right)^{\frac{1}{n}} - 1 \right], \quad (11)$$

where a_e is the effective radius, that is, the semimajor axis radius of the isophote that encloses one-half of the galaxies' total light. The effective surface brightness $SB_e = SB(a_e)$ is the SB at radius a_e . Half of each galaxy's total light is below this SB. It is not to be confused with $\langle SB_e \rangle$, the average surface brightness inside a_e , which is often used in the literature and significantly brighter than SB_e . The normalization constant $c(n) = 2.5 \times (0.868n - 0.142)$ ensures that a_e encloses half of the total light. Finally, the Sérsic index n controls the outer upward bend of the profile. Higher Sérsic indices hint at a more dominant halo.

If the curvature becomes too strong, then n diverges. For instance, the SB profile of the L3009 BCG ($n = 77 \pm 111$) has a curvature close to that critical value. The power-law slope of the SB profile for divergent n is $+5$. Stronger curvatures cannot be fitted by a single Sérsic function. We then extend the fitting formula by a second Sérsic function SB_2 to account for an outer light excess above the inner Sérsic function SB_1 :

$$SB(a) = -2.5 \log_{10}(10^{-0.4SB_1(a)} + 10^{-0.4SB_2(a)}). \quad (12)$$

The radius where both Sérsic profiles cross, that is, where their SBs are equal, is referred to as transition radius r_{\times} . The SB at that point is the transition surface brightness SB_{\times} .

The outer component is sometimes interpreted as the ICL, which is thereby assumed to be photometrically distinct. The (non)justification of this interpretation will be discussed in a forthcoming paper. The BCGs whose light profile can be fitted well enough by only one Sérsic function are referred to as *single Sérsic BCGs* (SS BCGs), and the BCGs that need two additive Sérsic functions are referred to as *double Sérsic BCGs* (DS BCGs).

An alternative explanation for the origin of some DS profile shapes could be a central poststarburst stellar population that formed after a wet merger, as is often seen in extra-light ellipticals (e.g., Faber et al. 1997; Kormendy 1999; Kormendy et al. 2009; Kormendy & Bender 2013). The origin of the DS shape would then be unrelated to the ICL phenomenon. Those BCGs have small DS transition radii relative to their effective radii $r_{\times} < 0.1r_e$ and small DS transition SBs of $SB_{\times} < 23$ g' mag arcsec $^{-2}$ (Hopkins et al. 2009; Kormendy et al. 2009). We neglect those inner regions for the fits.

The composite SB profiles including the Sérsic fits are shown in Appendix A, and the best-fit parameters are presented in Section 6.3. They are corrected for the broadening effects of the PSF wings (see Section 5.3). The fits are performed using the python `scipy` routine `curve_fit`, which is based on a nonlinear least squares method using the Levenberg–Marquardt algorithm. As pointed out by many authors (e.g., Seigar et al. 2007; Kormendy et al. 2009; Spavone et al. 2017), a simple χ^2 minimization based on measurement uncertainties is not optimal. The reasons are as follows: (1) the Sérsic model is empirical and does not describe the SB profile shapes perfectly, especially not the intrinsic “wiggles”; (2) the brightest SB data points have negligible uncertainties compared to the faintest, outermost ones, which would therefore render the outermost data points useless; (3) errors are strongly correlated; and (4) symmetric uncertainties in the background constant are asymmetric in magnitude units.

The SB profiles in Appendix A show that the scatter and systematic deviations from the Sérsic fits increase at faint SB levels. Therefore, we want to lower their weight but not neglect them for the fits. To achieve that, we minimize the function $\chi^2 = \sum_i (SB_i - SB_i^{\text{fit}}) / \Delta SB_i$, where SB_i is the i th SB data point, SB_i^{fit} is the value from the fit, and ΔSB_i are the uncertainties in SB that depend on SB_i itself. The latter do not represent the measurement uncertainties but still increase toward fainter SBs. We use a combination of two uncertainties. One is the background uncertainty of $\Delta BG = \pm 1$ count arcsec $^{-2}$, given for a photometric zero-point of $ZP = 30$ g' mag (see Section 5.1). Since the linear error bars are asymmetric in magnitude units, we mirror the upper error bars downward. We also added quadratically a systematic uncertainty of 0.18 g' mag arcsec $^{-2}$, which is on the order of stronger intrinsic “wiggles” in the SB profiles. We get

$$\Delta SB = SB + 2.5 \log(10^{-0.4(SB-ZP)} + \Delta BG) + ZP + 0.18. \quad (13)$$

The errors of the best-fit parameters are estimated using Monte Carlo simulations. They are on the same order of magnitude as the uncertainties due to profile cropping (see Section 5.4).

The cores below a median major-axis radius of $a = 0''.86 \pm 0''.26$ are excluded from the fits. The (usually) missing light has negligible influence on the structural parameters.

4.5. 2D Profile Integration

We calculate the total flux F_{tot} and half-light parameters r_e and SB_e of the galaxies by integrating the 2D light profiles numerically while considering the radially varying ellipticities. The SB and ellipticity profiles are spline-interpolated and then evaluated on a grid with equidistant step sizes $\Delta a ["]^{1/4} = 0.001$. The ellipticities below (beyond) the first (last) measured data point are kept fixed. The SBs fainter than the last measured data point or below the limiting magnitude of our survey, $SB_{\text{lim}} = 30$ g' mag arcsec $^{-2}$, are replaced by the single or double Sérsic fit. The two outer limits to which we integrate the light profiles are $SB = 30$ g' mag arcsec $^{-2}$ and effectively infinity.

The step sizes $a_{i+1} - a_i$ are smaller than the scales on which the flux F and ellipticity ϵ change significantly. In that limit holds the approximation

$$F_{\text{tot}} \simeq \frac{1}{2} (F_{\text{tot}}^{\text{lower}} + F_{\text{tot}}^{\text{upper}}), \quad (14)$$

where

$$F_{\text{tot}}^{\text{upper}} = \sum_i F_{i+1} \cdot \pi (a_{i+1}^2 (1 - \epsilon_i) - a_i^2 (1 - \epsilon_i)), \quad (15)$$

$$F_{\text{tot}}^{\text{lower}} = \sum_i F_i \cdot \pi (a_{i+1}^2 (1 - \epsilon_i) - a_i^2 (1 - \epsilon_i)). \quad (16)$$

The effective radius r_e is the semimajor axis radius of the isophote that encircles one-half of the galaxy's integrated flux $F_{\text{tot}}/2$. The effective surface brightness SB_e is the SB at that isophote.

5. Error Analysis and Correction for Systematic Effects

5.1. Background Subtraction

The extended and faint nature of the ICL makes it susceptible to being subtracted in the progress of background subtraction. We examine the magnitude of this effect with the

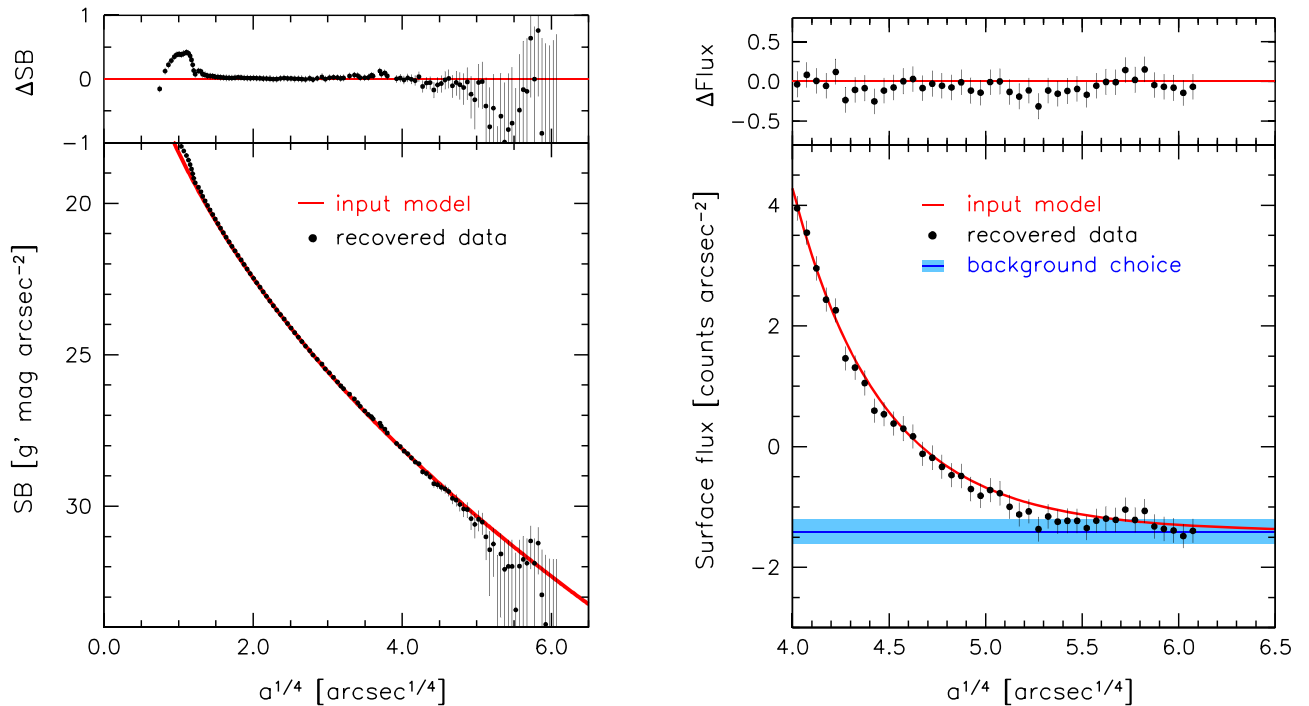


Figure 10. Recovered SB profile of a mock BCG that was inserted into raw data of a sky pointing. The regular data reduction including background subtraction was performed after that. The profile of the input model is plotted as a red line. The error bars are defined by the subjective uncertainty (blue shades) of the residual background constant (blue line).

help of mock data. An empty sky region was observed with the same strategy as the galaxy clusters. Then we insert a mock BCG with a perfect Sérsic light profile ($r_e = 100''$, $SB_e = 26 \text{ g' mag arcsec}^{-2}$, $n = 9$) into the raw data and reduce the data. The deviation of the measured light profile from the input profile provides a measure of the errors that we introduce by background subtraction and masking.

In Figure 10 we show that the light profile of the mock galaxy is well preserved down to $SB = 31 \text{ g' mag arcsec}^{-2}$. The main source of error is the choice of the residual background constant. It is always negative because of the flux-scaling of the NSF to the incompletely masked individual exposures (see Section 3.1.5). We conservatively estimate it to be $\pm 1 \text{ count arcsec}^{-2}$, based on the outermost surface flux profile flatnesses of the worst 75th percentile of all BCGs in our sample. There is a tendency to choose a too-high value because of the finite field of view. The uncertainty corresponds to a limiting surface brightness of $SB_{\text{lim}} = 30 \text{ g' mag arcsec}^{-2}$. That estimation is in agreement with the comparison of the SB profiles measured from WWFI data and larger field-of-view data from the 40 cm Wendelstein Telescope and 70 cm Jay Baum Rich Telescope (JBRT; Section 5.5). The effect of choosing a too-high background constant is a drop in the outermost SB data points. That error only concerns surface brightnesses that are below our limiting magnitude $SB_{\text{lim}} = 30 \text{ g' mag arcsec}^{-2}$.

5.2. Galactic Cirrus

Foreground dust in the Galaxy fundamentally limits the depth of optical imaging data (e.g., Miville-Deschênes et al. 2016 and references therein). It reflects the integrated stellar light of the Galaxy and becomes visible as filamentary structures that are easily misinterpreted as stellar streams. The dust emits at far-infrared and radio wavelengths and is thus

easy to identify as not of extragalactic origin (Duc et al. 2015; Besla et al. 2016).

We estimate the cirrus flux in our observations by scaling the 857 GHz (350 μm) far-infrared emission maps published by Planck Collaboration et al. (2014) so that the overall variations in dust flux match the ones of the galactic cirrus in our most strongly contaminated cluster A407 (see Figure 11):

$$F_{\text{cirrus}}^{\text{g'}} [\text{counts}] \approx 0.5 F_{857 \text{ GHz}} [\text{MJy sr}^{-1}], \quad (17)$$

where the units on the left-hand side are calibrated to a photometric zero-point of $ZP = 30 \text{ g' mag}$ and a pixel scale of $0''.2/\text{pixel}$. We match the variations in flux and not the absolute flux because the average background was already subtracted from the WWFI stacks during data reduction. The residual cirrus is visible down to a surface brightness of $SB \sim 28 \text{ g' mag arcsec}^{-2}$, to which level we mask it by hand. Hidden cirrus below this SB level can evoke a systematic scatter in the outermost data points of the light profiles.

We define three categories of increasing cirrus contamination: A (invisible in the optical images), B (weak contamination), and C (strong contamination; see Figure 11). Not the total dust flux but its large-scale variations have the strongest influence on the light profiles. We estimate these variations as the standard deviation σ of the dust surface flux in binned, $15 \times 15 \text{ px}$ thumbnails of the one-square-degree fields of view. The thresholds are expressed as surface brightness variations SB_σ in units of $\text{g' mag arcsec}^{-2}$:

$$\begin{aligned} \text{Category A: } & 27.6 < SB_\sigma \\ \text{Category B: } & 26.9 < SB_\sigma < 27.6 \\ \text{Category C: } & SB_\sigma < 26.9. \end{aligned} \quad (18)$$

The cirrus-contamination category of each cluster is labeled on the image cutouts in Appendix B. In our sample, 131

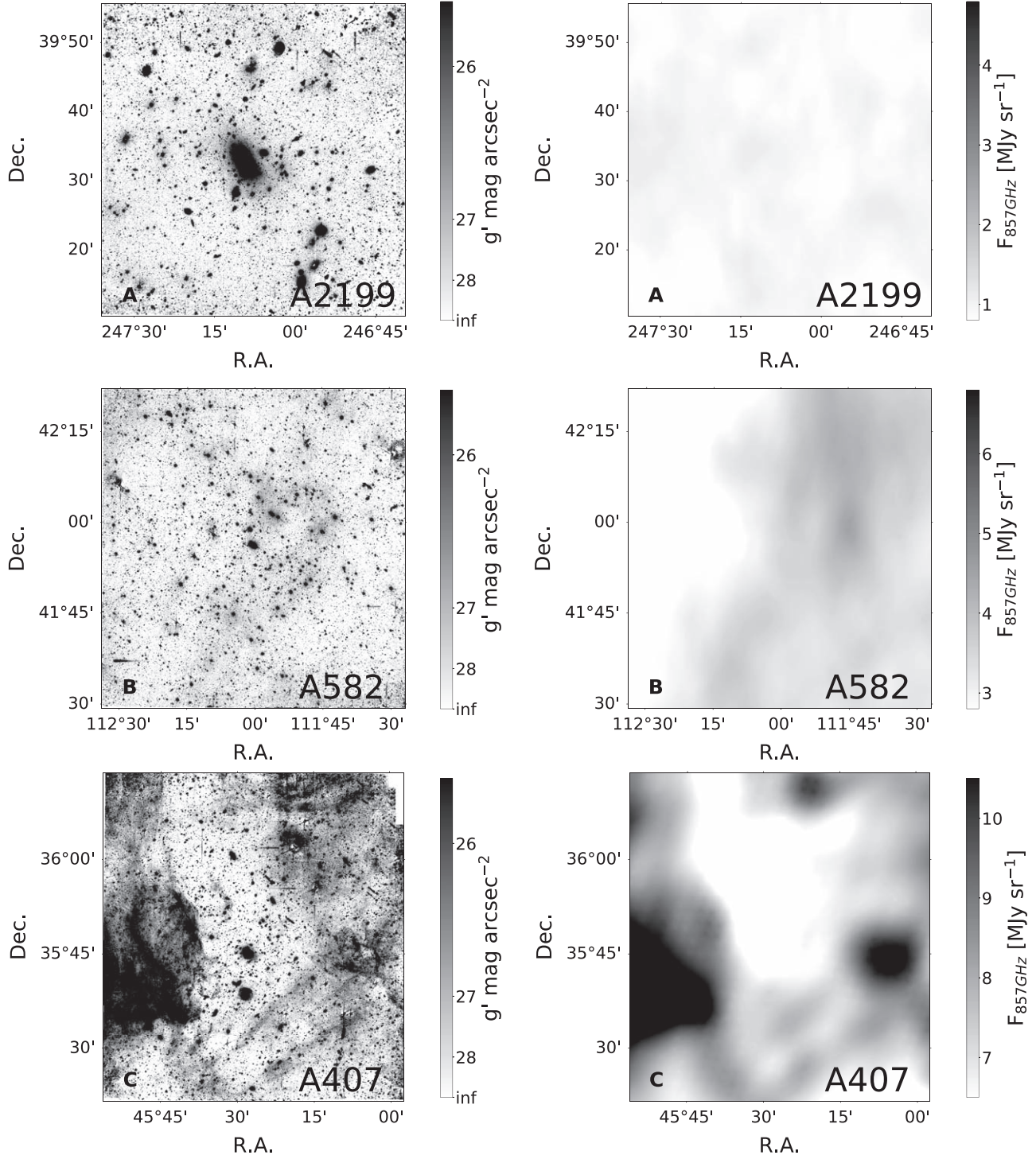


Figure 11. Left panels from top to bottom: three examples for contamination by Galactic cirrus across the fields of view of A2199, A582, and A407. All image cutouts are centered on the BCG. Contamination categories increase from A to C. Right panels: far-infrared 857 GHz maps of the same regions from Planck Collaboration et al. (2014). Note that the background constant and gradient in the optical images were modeled and subtracted by the night-sky flat procedure (see Section 3.1.5).

clusters (77%) belong to category A, 28 clusters (16.5%) to category B, and 11 clusters (6.5%) to category C.

That strength of contamination is reduced (1) by manual masking, (2) by applying a robust estimator on the pixel histogram (see Section 4.2), (3) because the flux is averaged along the large isophotes in the low-SB galactic outskirts, and (4) because large-scale variations, that is, a gradient across the field of view, are included in the NSFs and subtracted.

An all-sky map of the scaled far-infrared map is shown in Figure 2.

5.3. PSF Effects

Seeing has a distorting influence on the light profiles: central galaxy light is redistributed toward larger radii. This effect manifests itself as (1) a flattening and circularization in the

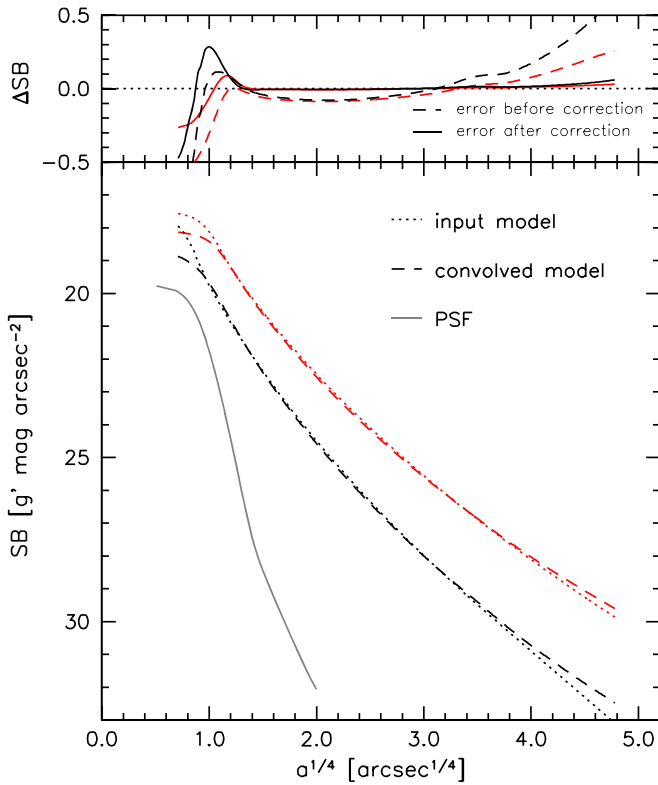


Figure 12. Effect of PSF broadening on SB profiles of two different mock BCGs (red and black). The dotted lines show the original SB profiles, and the dashed lines show the profiles after convolution with the PSF. The dashed and continuous lines in the top panel show the residuals before and after correction, respectively.

inner few arcseconds and (2) brighter SB in the range $1 \lesssim r \lesssim 4$ PSF FWHM. The effect is of the order of the core sizes of the local BCGs that we aim to resolve. As explained in Section 4, we therefore replace the central part of the light profiles by the ones that we either measured from archival (undeconvolved) *Hubble Space Telescope* imaging data or deconvolved WWFI data. As shown in Figure 9, the deconvolved profiles are accurate to almost Nyquist sampling quality, that is, $\gtrsim 0''.4$ resolution. The cores with sizes of order $1''$ are therefore real and not resolution artifacts.

Not only the PSF’s center but also its outer wings distort the galaxy light profiles (see Duc et al. 2015 and references therein or Trujillo & Fliri 2016). The PSF’s wings and reflections from the BCG’s center overlap with the ICL. In other words, light is redistributed from the center to the outskirts. We refer to this effect as PSF broadening. It becomes a problem when the galaxy’s center is bright compared to its outer halo. Figure 12 shows the severity of this effect. SB profiles of two (red and black) representative model BCGs are plotted as dotted lines. The SB profiles after 2D convolution with the PSF are overplotted as dashed lines. The systematic error due to PSF broadening is $0.1 > \Delta SB > 0.5 \text{ g' mag arcsec}^{-2}$ and increasing with galaxy size.

We now describe our correction method for the broadening effect. The accurate approach would be to deconvolve the imaging data prior to the SB profile measurement. However, this is computationally challenging considering the large kernel size of $\sim 2000 \times 2000$ pixels and Richardson–Lucy deconvolution (Lucy 1974) being an iterative procedure. We use a computationally faster method that is based on the approximation that the

amount of scattered light is small (1.78%, see Section 3.1.4) compared to the total light. Under these circumstances, a secondary convolution $i * t$ by image processing results in similar light scattering even after the primary convolution $i = r * t$ by the telescope optics is already inherent to the images. That is quantified by

$$i = r * t, \quad (19)$$

$$r \approx i - (i * t - i), \quad (20)$$

where r is the unknown intrinsic light distribution, t is the kernel, that is, the PSF, and i is the image data after primary convolution. We apply a 2D convolution⁴ to images that were regenerated from the isophotal shape parameters. The scattered light is reconstructed by subtracting the twice-convolved image $i * t$ from the primary convolved image i . Then, by subtracting this scattered light from the primary convolved image, the intrinsic light distribution is recovered (see Equation (20)).

The deviation of the corrected from the original (intrinsic) light profiles of the mock BCGs is shown in Figure 12 (top panel) as continuous lines. The SB data points at radii $a > 4''$ agree well with the input model. The inner regions are badly recovered because the small-influence approximation fails there. However, these regions of the profiles are replaced by those derived from *HST* or deconvolved WWFI data (see Section 4.3).

Each SB profile of the real BCGs is corrected individually. The median correction for the structural parameters that are determined by direct integration of the light profiles (i.e., independent of the Sérsic fits) is

$$r_{e,30}^{\text{corrected}} / r_{e,30}^{\text{uncorrected}} = 0.94 \pm 0.03, \quad (21)$$

$$SB_{e,30}^{\text{corrected}} - SB_{e,30}^{\text{uncorrected}} = -0.11 \pm 0.05, \quad (22)$$

$$M_{\text{tot},30}^{\text{corrected}} - M_{\text{tot},30}^{\text{uncorrected}} = 0.03 \pm 0.02, \quad (23)$$

where the index “30” indicates that the parameters were determined by integrating the light profiles out to the isophote with $SB = 30 \text{ g' mag arcsec}^{-2}$ (for details, see Section 4.5). As expected, only a small influence on the integrated brightness is found. The integration aperture is sufficiently large that the redistribution of the light is close to negligible. The effective radii are increased and the effective surface brightnesses are dimmed by the broadening effect.

After fitting Sérsic functions to the SB profiles before and after PSF broadening correction, we calculate the median corrections for the Sérsic parameters of the SS BCGs:

$$r_{e,SS}^{\text{corrected}} / r_{e,SS}^{\text{uncorrected}} = 0.88 \pm 0.06, \quad (24)$$

$$SB_{e,SS}^{\text{corrected}} - SB_{e,SS}^{\text{uncorrected}} = -0.25 \pm 0.06, \quad (25)$$

$$n_{SS}^{\text{corrected}} / n_{SS}^{\text{uncorrected}} = 0.94 \pm 0.03, \quad (26)$$

and for the Sérsic parameters of the DS BCGs:

$$r_{e,DS1}^{\text{corrected}} / r_{e,DS1}^{\text{uncorrected}} = 0.99 \pm 0.04, \quad (27)$$

$$SB_{e,DS1}^{\text{corrected}} - SB_{e,DS1}^{\text{uncorrected}} = -0.03 \pm 0.08, \quad (28)$$

$$n_{DS1}^{\text{corrected}} / n_{DS1}^{\text{uncorrected}} = 0.99 \pm 0.04, \quad (29)$$

⁴ We also experimented with a 1D convolution using the `python` package `scipy.signal.convolve`. A simple test applied to a slice along the major axis of a BCG and PSF light profiles results in a stronger broadening effect than for the 2D convolution and, hence, erroneous results.

$$r_{e,DS2}^{\text{corrected}} / r_{e,DS2}^{\text{uncorrected}} = 0.95 \pm 0.03, \quad (30)$$

$$SB_{e,DS2}^{\text{corrected}} - SB_{e,DS2}^{\text{uncorrected}} = -0.04 \pm 0.08, \quad (31)$$

$$n_{DS2}^{\text{corrected}} / n_{DS2}^{\text{uncorrected}} = 0.96 \pm 0.04. \quad (32)$$

5.4. Undetected ICL below the Limiting Magnitude

The SB limit of our survey is $SB_{\text{lim}} = 30 \text{ g' mag arcsec}^{-2}$. Below that limit, we have no reliable information on how the SB profiles continue. An educated guess is the extrapolation of the fitted Sérsic profiles because there is no indication for a truncation just above this limit (see Section 6.2). The following median corrections have to be applied when the lower SB boundaries are increased from 30 to infinity $\text{g' mag arcsec}^{-2}$:

$$r_{e,\infty} / r_{e,30} = 1.20 \pm 0.15, \quad (33)$$

$$SB_{e,\infty} - SB_{e,30} = 0.31 \pm 0.22, \quad (34)$$

$$M_{\text{tot},\infty} - M_{\text{tot},30} = -0.09 \pm 0.06. \quad (35)$$

The indices “30” and “ ∞ ” indicate the SB of the outermost considered isophote. *The averages of both values are listed in Section 6.3, and the uncertainties derived from both integration limits are taken as the error.* We stress again that all median correction factors in Sections 5.3 and 5.4 are only given for illustrative purposes. Each SB profile was corrected individually.

5.5. Comparison to Data Obtained with Other Telescopes

The key obstacle for deep imaging is the task of background subtraction. In addition to the mock-BCG test described in Section 5.1, we perform another test to make sure that the ICL is not oversubtracted in the WWFI data. For a control sample, we have obtained independent imaging data for A1177 with the 70 cm JBRT at the WISE observatory (2 hr target integration time) and for A2589 with the 40 cm telescope at the Wendelstein observatory (12 hr integration time). Both imagers span an even wider field of view than the WWFI and are made of one single CCD chip. That makes them less susceptible to systematic errors during background subtraction because the BCG+ICLs cover a smaller fraction of the field of view and less masking is required.

The control sample data were observed, dithered, and reduced in a similar way to the WWFI data. The only difference is the method of background subtraction. The background in the 70 cm JBRT data was modeled by fourth-order 2D polynomials in each exposure. Nonphotometric observing conditions degraded the stability of the background pattern so that the NSF method failed. However, the polynomial approach works sufficiently well because of the large field of view.

The background in the 40 cm WST data was modeled by scaling and averaging the two bracketing source-masked exposures that were taken before and after each exposure. No offset sky exposures were taken. The sky background is modeled from the science exposures themselves. The large dither pattern ensures that empty sky regions in the bracketing exposures always fall around the BCG’s position so that the sky is modeled accurately across the whole field of view. Regions that happen to be masked in both bracketing exposures are replaced by fourth-order 2D polynomials that were fitted to the whole average sky images.

Figure 13 shows a comparison of the SB profiles measured in both data sets. The WWFI-obtained profiles are plotted before (gray) and after (black) PSF broadening correction (see Section 5.3). The two comparison profiles are not PSF broadening corrected. The overall agreement especially in the outermost data points provides further confidence in the accuracy of the background subtraction method. Moreover, it confirms that $<1 \text{ m}$ class telescopes can be sufficient to perform deep imaging projects by reaching the $30 \text{ g' mag arcsec}^{-2}$ SB limit.

6. Results

6.1. Accretion and Merging Signatures

The advent of low-surface-brightness photometry has unveiled a myriad of fine structure in the outskirts of galaxies. These relics of violent accretion have been predicted by numerical simulations as the most direct evidence for hierarchical clustering (Bullock & Johnston 2005; Johnston et al. 2008; Rudick et al. 2009; Cooper et al. 2010, 2013; Puchwein et al. 2010; Rodriguez-Gomez et al. 2016; Harris et al. 2017; Mancillas et al. 2019). They have been discovered around local late-type galaxies (e.g., Martínez-Delgado et al. 2010; Chonis et al. 2011; Foster et al. 2014; Ibata et al. 2014; Amorisco et al. 2015; Merritt et al. 2016) and local early-type galaxies (Tal et al. 2009; Duc et al. 2015; Bílek et al. 2016; Crnojević et al. 2016; Duc 2017), as well as galaxy groups (Da Rocha & Mendes de Oliveira 2005; Da Rocha et al. 2008; Watkins et al. 2014, 2015; Okamoto et al. 2015; Spavone et al. 2018) and galaxy clusters (Feldmeier et al. 2002; Arnaboldi et al. 2012; Iodice et al. 2016, 2017, 2019; Mihos et al. 2017). A review on the topic can be found in Carlin et al. (2016). For a comparison between literature data on the frequency of disturbed morphologies, see Atkinson et al. (2013).

We visually inspect the clusters for accretion and merging signatures and classify them into four categories: (1) two BCGs, (2) shells, (3) tidal streams, and (4) multiple nuclei. There was no a priori knowledge of the galaxies’ Sérsic type during the identification procedure. To maximize our likelihood of finding structures on various surface brightnesses, we have visually scanned linearly and logarithmically scaled, minimum filtered (Bílek et al. 2016), isophote-model and parametric-model subtracted images. The 2D models for the latter two methods are created from the isophotal shape profiles. For the parametric models, we replaced the SB values in the data tables by their corresponding SS or DS fit values.

One prototypical example for each category is shown in Figure 14, top panel. An explanation of the characteristics of each category follows.

The “two BCGs” category is not a direct sign of interactions between galaxies, but a likely indicator for merging clusters, as is the case for the Coma cluster. Since the appearance of at least two similar-sized BCGs is a hint of a nonrelaxed state of the cluster, we include this category in our analysis. We find that 7.0% of the clusters have two BCGs (4.1% for SS BCG clusters and 12.2% for DS BCG clusters).

Shells are accumulations of stars that align in circle segments around the BCG center (e.g., Malin & Carter 1980, 1983; Hernquist & Quinn 1988, 1989 and many more). These segments can be more or less concentric, depending on the type of shell system. They form when a satellite galaxy falls onto the BCG on a nearly radial trajectory with pericentric

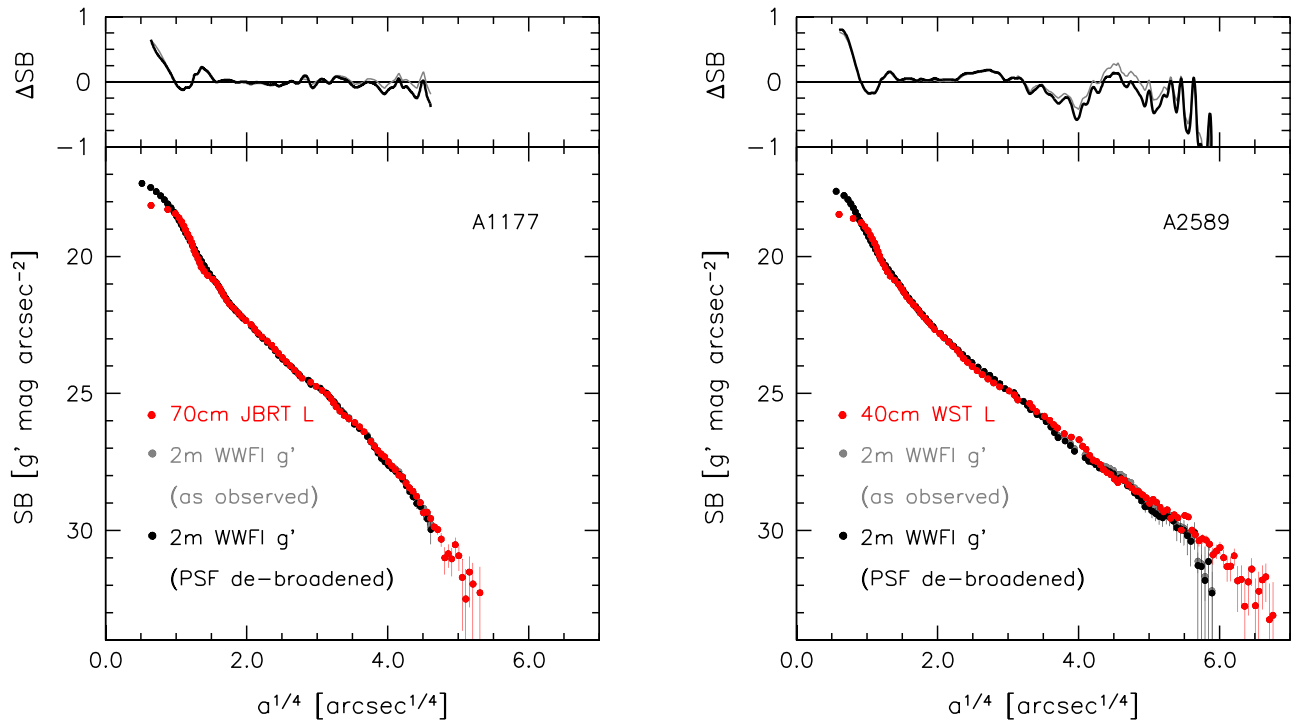


Figure 13. Control sample of two BCGs that were observed independently with different telescopes (red data points). Left panel: 70 cm Jay Baum Rich Telescope (JBRT) at the *WISE* observatory, owned and operated by Tel Aviv University. Right panel: 40 cm telescope at the Wendelstein observatory. The photometric zero-points of the *L*-band profiles are adjusted so that the *L*-band profiles match the WWFI *g'*-band profiles for comparison. Color gradients in the two filters are assumed to be negligible. The WWFI *g'*-band profiles are shown with (black) and without (gray) PSF debroadening correction. The deviations of the spline-interpolated comparison profiles from the WWFI profiles are shown in the top panels.

distance <15 kpc (Karademir et al. 2019) and is disrupted (Bilek et al. 2016; Pop et al. 2018). The shells mark the turnaround lines in the orbits of the progenitor’s stars. Shells have been reproduced in simulations with mass ratios of the merging galaxies ranging from 1/100 (Quinn 1984; Karademir et al. 2019) to $>1/3$ (Karademir et al. 2019; Pop et al. 2018). See also Bilek et al. (2015) for a review. Shells are found in between $\sim 10\%$ (Schweizer & Seitzer 1988) and $\sim 22\%$ of elliptical galaxies (Tal et al. 2009). The frequency in the Illustris simulation is $18 \pm 3\%$, which increases with increasing mass cut (Pop et al. 2018). We find that 9.4% of our analyzed BCGs show shells (11.6% of SS BCGs and 4.1% of DS BCGs). A lower frequency could be explained with the degrading angular resolution because the BCGs in our sample are a factor of ~ 10 more distant than the local ellipticals in the Tal et al. (2009) sample, which decreases the detectability of existing shells. Our result should therefore be understood as a lower boundary for the abundance of shells in BCGs.

Tidal streams are made of stars that were liberated from a satellite galaxy by a collision (Moore et al. 1996) or due to the mean tidal field of the cluster (Merritt 1984). These unbound stars then virialize in the cluster and add up to the ICL budget. For instance, unprecedentedly deep photometric surveys of the Virgo (Mihos et al. 2017) and Fornax clusters (Iodice et al. 2016, 2017, 2019) have unveiled multitudes of tidal streams. Other examples have been discovered in the Coma and Centaurus clusters (Gregg & West 1998; Trentham & Mobasher 1998; Calcáneo-Roldán et al. 2000). We do not make a strict differentiation between tidal tails and tidal streams as proposed by Duc et al. (2015) because we lack color information. Finally, we find that 22% of our observed BCGs show some form of stream-like features (21% of SS BCGs and

24% of DS BCGs). The features are usually dynamically hotter than the ones reported for field galaxies (e.g., Martínez-Delgado et al. 2010) and thus dissolve quicker. The observed abundance therefore implies ongoing ICL accretion.

Multiple nuclei are in $\sim 47\%$ of the cases simply chance superpositions as concluded from their undisturbed morphology (Lauer 1988). The remaining half is split into high-velocity unbound interactions (24%) with radial velocity differences $\Delta V \gtrsim 400$ km s $^{-1}$ that lead to tidal stripping of the secondaries’ envelopes and possible low-velocity, strong merger interactions (29%) that lead to cannibalism of the secondary nucleus (Lauer 1988; see also Tonry 1985a, 1985b; Beers & Tonry 1986). Without differentiating between the cases of real interactions and pure projections, we identify at least one secondary nucleus in 24% of all BCGs (21% of SS BCGs and 24% of DS BCGs). That is a slightly lower fraction than values reported in the literature (28%, Hoessel 1980; 45%, Schneider et al. 1983).

The relative abundances of the four discussed types of accretion signatures are also shown in Figure 14. The error bars are determined using Poisson statistics. We cannot tell whether SS or DS BCGs have higher abundances of specific accretion signature types, due to small-number statistics. However, the total frequency of accretion signatures is 46% for SS BCGs and 63% for DS BCGs. The latter show more indications of ongoing merging processes with a 1σ certainty. The frequency for all BCGs is 51%.

6.2. Average Profiles

The average light profiles and isophotal shape parameter profiles are presented in Figure 15. All profiles are averaged in

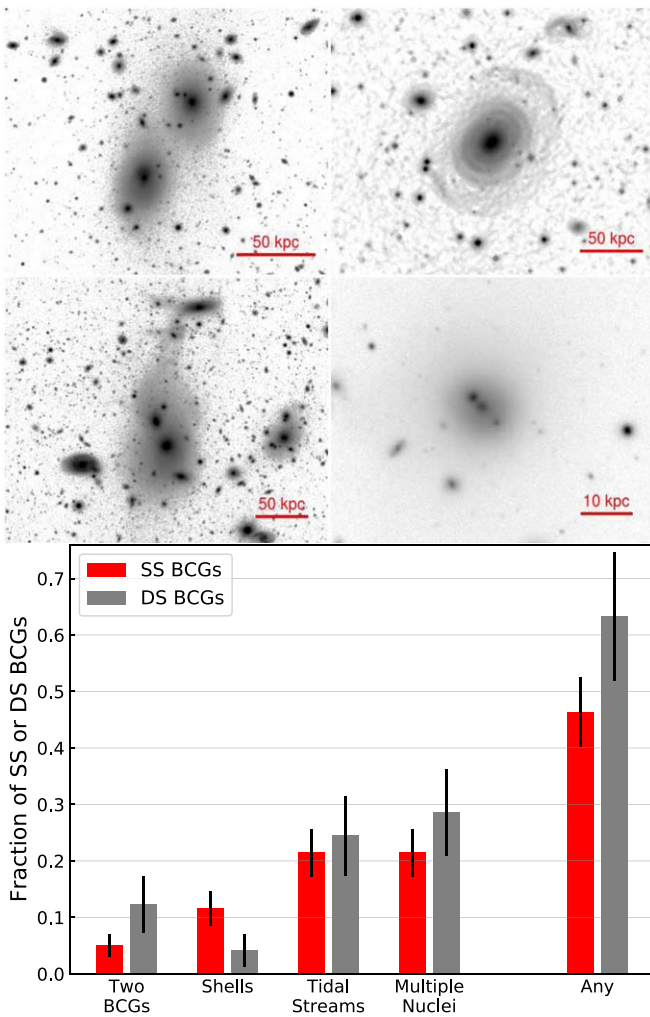


Figure 14. Accretion and merging signatures. Top panel: representative examples for each category. Top left: two BCGs in A1190. Top right: shells in A2197. Bottom left: tidal streams in A1257. Bottom right: multiple nuclei in A1185. Bottom panel: relative abundance of each of the four features and of any of the four features.

radial intervals besides the SB profiles, which were calculated by averaging in SB intervals. The different method is necessary because the limited depth would otherwise result in an artificial upward trend in the SB profiles below $SB \gtrsim 28 \text{ g}' \text{ mag arcsec}^{-2}$. Before averaging, outliers in every radius (or SB) interval are rejected that deviate more than 6.5 standard deviations from the mean. If data points for a minimum of 14 BCGs remain, then the average is plotted. The 1σ standard deviations of the intrinsic scatter are shown as shaded regions for SB, ϵ , ΔPA , $\Delta r/r$, and a_4 . The shaded regions for a_3 , b_3 , and b_4 correspond to the measurement uncertainties.

The SB profiles are a composite of data and fits. Inner regions below $r < 16 \text{ kpc}$ are taken directly from the measured light profiles, and the outer regions are replaced by the Sérsic fits. The radius is given along the effective axis $r = \sqrt{ab}$. This is equivalent to measuring the profiles in circular apertures. It allows direct comparison to the SB profile that was measured by Zibetti et al. (2005) by combining 683 galaxy cluster images from the SDSS-DR1. We apply a K-correction of $g'[\text{rest frame}] = [\text{observed frame}] - 0.71 \text{ mag}$ to the r -band data from Zibetti et al. (Chilingarian et al. 2010; Chilingarian & Zolotukhin 2012), a color correction of $g = r + 1.2$, derived

from their multiband SB profiles and corrected for cosmic dimming. The average profile from Zibetti et al. is inconsistent with our average profiles within the standard error of the mean, that is, the thickness of the red and black lines. We unsuccessfully tried to match our average SB profiles with the profile from Zibetti et al. by applying various total brightness cuts on our sample: after discarding all BCGs fainter than $M_{\text{tot}} > -23 \text{ g}' \text{ mag}$, the average SBs around $SB \sim 30 \text{ g}' \text{ mag arcsec}^{-2}$ match well, but the slope below $r < 40 \text{ kpc}$ is too shallow. Instead, if we discard all BCGs brighter than $M_{\text{tot}} < -23 \text{ g}' \text{ mag}$, then the slopes match well at these radii but the profiles are too faint, especially in the ICL outskirts. We conclude from this analysis that the deviations cannot be attributed to sample selection alone. A possible explanation is the different age of the galaxies. The mean redshift $\bar{z}_Z = 0.25$ of Zibetti et al.'s sample is higher than ours ($\bar{z}_K = 0.06$). That equals 2.16 Gyr in time evolution, after which the BCG's SB profiles might have evolved to become smoother.

The overall shape and scatter of SS and DS BCGs are fairly similar. The largest difference occurs around $r = 240 \text{ kpc}$, where DS BCGs are on average $0.65 \pm 0.18 \text{ g}' \text{ mag arcsec}^{-2}$ brighter than SS BCGs. The difference decreases again toward larger radii and becomes zero at $r = 470 \text{ kpc}$.

We now move on to discuss the isophotal shape parameters. As explained in Section 4, these parameters are kept fixed beyond the last plausible radius. Hence, the average profiles for these parameters do not extend as far out as the averaged surface brightnesses.

The ellipticities $\epsilon = 1 - b/a$ rise with radius. The slope is slightly shallower for SS BCGs.

The position angles PA are counted counterclockwise starting from the north-south axis. PA is unambiguously defined in the range $0^\circ \leq PA < 180^\circ$. It flips $\pm 180^\circ$ when it is crossing the north-south axis. These jumps are eliminated by the following procedure: if the difference between two subsequent PA data points is greater than $PA_i - PA_{i+1} > 90^\circ$, an offset of 180° is subtracted from all data points at greater radii. The opposite is done when $PA_i - PA_{i+1} < -90^\circ$. All PA profiles are normalized to the median in the range $16 < r[\text{kpc}] < 40$. Since PAs are randomly oriented, their profiles average to constant zero for a large sample. To avoid this, we flip PA profiles with negative gradients. The gradients are determined between the median of the range $16 \leq r[\text{kpc}] < 40$ and the median of the range $r \geq 40 \text{ kpc}$. We find average isophote twists of order $\Delta PA / \Delta r \sim 10^\circ / 100 \text{ kpc}$ for both SS and DS BCGs. The scatter beyond $r \gtrsim 50 \text{ kpc}$ is about twice as high for DS BCGs than for SS BCGs. The higher scatter below $r \lesssim 20 \text{ kpc}$ can be explained by the lower ellipticities of DS BCGs at these radii.

The ICL offset $\Delta r(r)$ is the distance between the center of the BCG and the center of the isophotal ellipse with radius r along the effective axis. The average and relative ICL offsets increase with radius. At $r = 150 \text{ kpc}$, they reach 10% (i.e., 15 kpc) for SS BCGs and 20% (i.e., 30 kpc) for DS BCGs. The spatial direction of these offsets will be discussed in a forthcoming paper.

Isophotal distortions from perfect ellipses are expanded in a Fourier series (see Section 4.1). The most informative coefficient a_4 is expressed as a percentage of semimajor axis radius a (see Figure 15, bottom middle panel). It quantifies the diskyness ($a_4 > 0$) or boxiness ($a_4 < 0$) of the isophotes (e.g., Bender & Moellenhoff 1987).

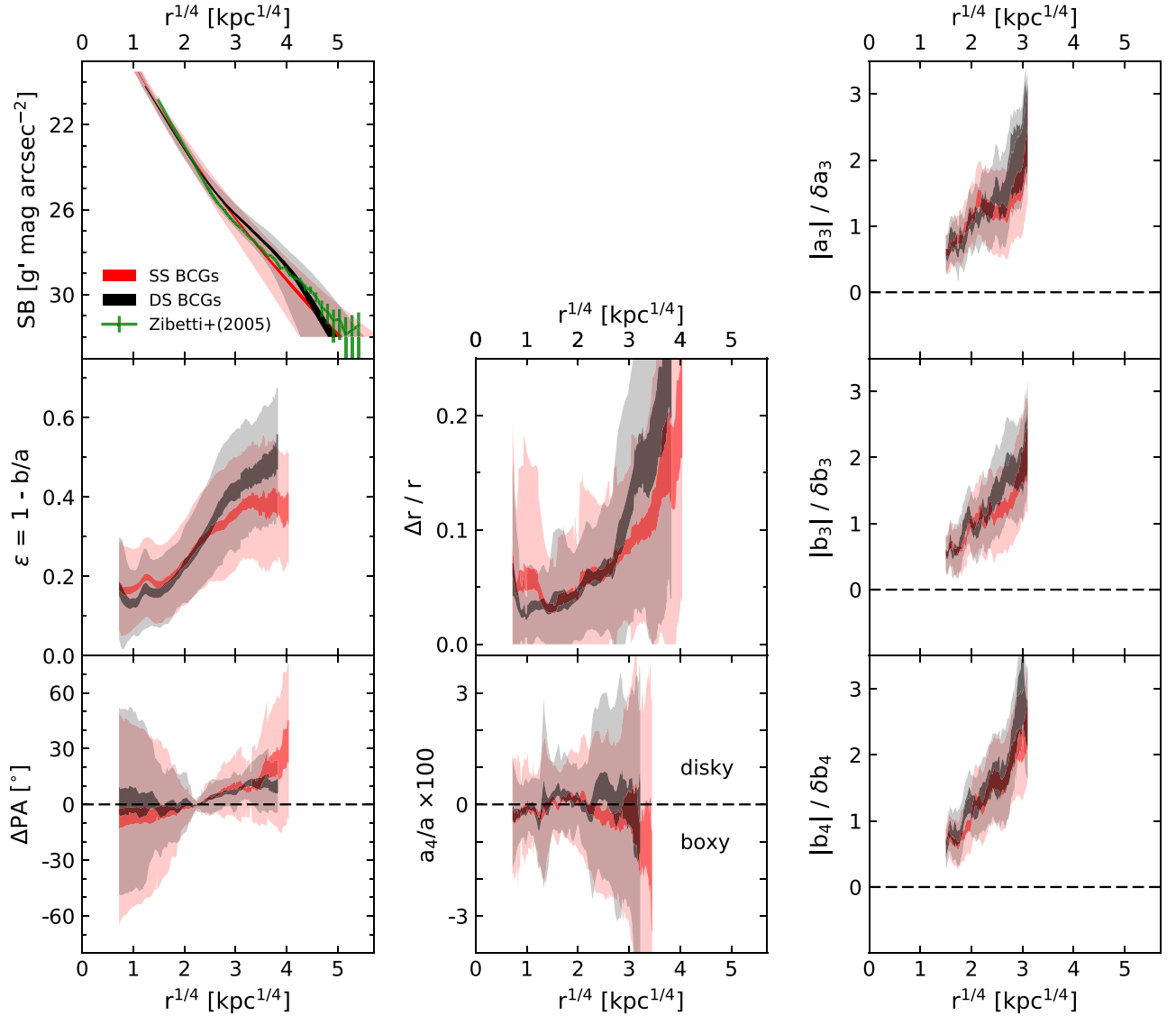


Figure 15. Average profiles of SS (DS) BCGs in red (black). The radius on the x-axis is given along the effective axis $r = \sqrt{ab}$. The more transparent shades correspond to the intrinsic 1σ scatter, and the more opaque shades correspond to the standard error of the mean. The average SB profiles are created by averaging the measured SB data points of all BCG+ICLs inside $a < 16$ kpc and the extrapolated Sérsic fits outside of that semimajor axis radius. Isophote twist ΔPA profiles are normalized to the median in the range $16 < r[\text{kpc}] < 40$. Profiles with a negative gradient are flipped. Coefficients of the Fourier expansion of the deviations from elliptical isophotes (see Equation (9)) are plotted in the bottom middle and right panels. The diskyness/boxyness indicator a_4 is expressed as a percentage of the semimajor axis radius a . The more transparent error shades describe the 1σ intrinsic scatter. The other three Fourier coefficients a_3 , b_3 , and b_4 are expressed differently because they quantify asymmetric distortions that are randomly oriented and therefore average to zero for large samples. Their absolute value is divided by the measurement uncertainty. This is a measure of the significance that the corresponding deviations are detected. The error shades correspond to the 1σ measurement uncertainty. The comparison between SS and DS BCGs is only fair because the measurement scatter is almost identical.

We find that the inner isophotes in $10 \text{ kpc} \lesssim r \lesssim 25 \text{ kpc}$ are on average slightly diskly. SS BCGs become boxy in the outskirts beyond $r \gtrsim 40 \text{ kpc}$, whereas DS BCGs are slightly diskly at that radius.

We show the first three coefficients of the Fourier expansion a_3 , b_3 , and b_4 in Figure 15. The two parameters a_3 and b_3 quantify the triangularity of the isophotal shapes. The last parameter b_4 quantifies distortions similar to the diskly/boxy parameter a_4 , but includes a $\sim 45^\circ$ rotation because it is the amplitude of the sine component from the Fourier expansion (see Equation (9)). The values of all of these parameters average to zero for a large sample because asymmetric distortions are randomly oriented. In order to gain knowledge from them, we have to look at their moduli. What makes the

analysis difficult is that the measurement errors are of the order of the values themselves. A better diagnostic is the significance whether a_3 , b_3 , and b_4 type deviations are detected at all. We therefore express these parameters in the form of their modulus, divided by the measurement uncertainty. The error shades in the bottom three panels on the right are the average measurement uncertainties and, like for the other parameters, the intrinsic scatter. A comparison between SS and DS profiles is only fair because the average uncertainties are very similar, as is expected for a large sample size of similar galaxies. We find that SS BCGs are characterized by lower values for a_3 , b_3 , and b_4 than DS BCGs. In other words, SS BCGs have less pronounced asymmetric isophotal distortions, indicating a more relaxed state of SS BCGs.

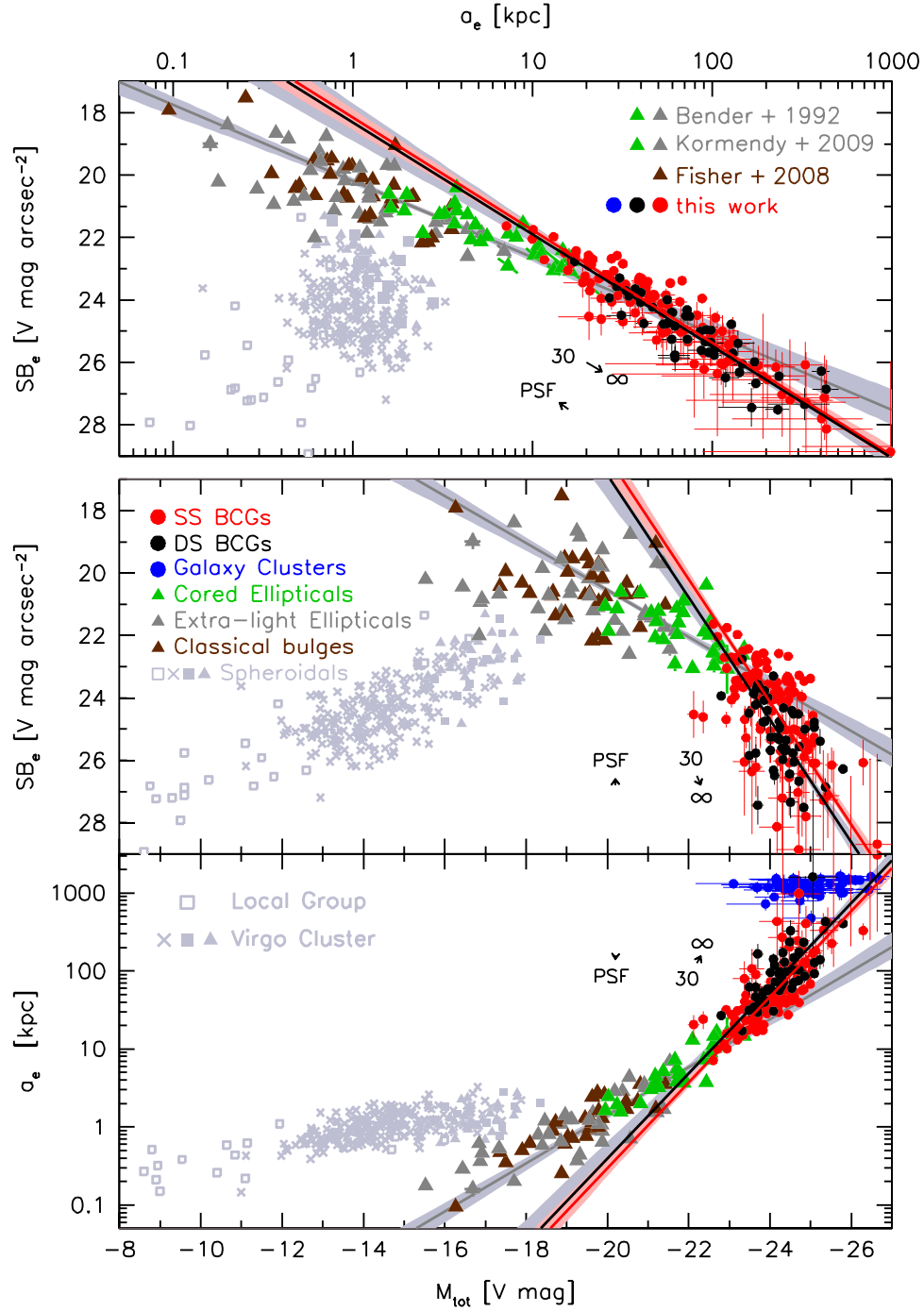


Figure 16. Comparison between integrated absolute brightnesses M_{tot} , effective radii a_e along the major axis, and effective SB SB_e of BCGs, regular ellipticals, and galaxy clusters. The basis for this plot is Figure 37 in Kormendy et al. (2009) with updates in Figure 2 in Kormendy & Bender (2012) and Figure 14 in Bender et al. (2015). The galaxy data points from the literature and from this work are calculated from 2D profile integration and evaluated along the major axes. For the clusters, the (circular) gravitational radius r_g is used, which will be described in a forthcoming paper. The arrow $30 \rightarrow \infty$ shows the median shift of the BCG parameters when using no upper integration limit compared to $SB_{\text{lim}} = 30 \text{ g' mag arcsec}^{-2}$. The arrow $\rightarrow \text{PSF}$ shows the median shift of the BCG parameters due to the PSF broadening correction. The g' -band magnitudes were converted to V-band magnitudes via $V = g - 0.45 \text{ mag}$ (Jester et al. 2005) for $g - r = 0.78$ (Tojeiro et al. 2013).

6.3. Structural Parameters

In this section, we examine first how BCGs populate the parameter space (r_e , SB_e , M_{tot}) and second how the Sérsic indices n are distributed. We therefore overplot the structural parameters listed in columns (9), (10), and (11) in Appendix C on Figure 2 from Kormendy & Bender (2012). The result is shown in Figure 16. The literature parameters are determined by integrating

the extrapolated SB profiles down to $SB \sim 29.7 \text{ V mag arcsec}^{-2}$ for core ellipticals and down to an arbitrarily faint SB for coreless ellipticals and dwarf spheroidal galaxies (Kormendy et al. 2009). Hence, they include most of the stellar halos. Since no attempt at a galaxy–halo decomposition was done for the literature parameters, we avoid doing so for the BCGs, too; that is, we use the structural parameters determined for the whole light distribution including ICL for a consistent comparison.

Table 3
Correlations between Structural Parameters

Galaxy Type (1)	X (2)	Y (3)	Slope α (4)	Offset β (5)
Regular Es	M	$\log(r_e)$	-0.309 ± 0.020	-6.02 ± 0.43
SS BCGs	M	$\log(r_e)$	-0.550 ± 0.037	-11.29 ± 0.87
DS BCGs	M	$\log(r_e)$	-0.547 ± 0.060	-11.10 ± 1.43
All BCGs	M	$\log(r_e)$	-0.563 ± 0.032	-11.57 ± 0.75
Regular Es	M	SB_e	-0.75 ± 0.13	5.47 ± 2.65
SS BCGs	M	SB_e	-1.90 ± 0.20	-20.32 ± 4.70
DS BCGs	M	SB_e	-1.96 ± 0.35	-20.95 ± 8.26
all BCGs	M	SB_e	-2.02 ± 0.18	-22.93 ± 4.26
Regular Es	$\log(r_e)$	SB_e	2.44 ± 0.22	20.18 ± 0.12
SS BCGs	$\log(r_e)$	SB_e	3.61 ± 0.13	18.61 ± 0.22
DS BCGs	$\log(r_e)$	SB_e	3.58 ± 0.26	18.77 ± 0.51
All BCGs	$\log(r_e)$	SB_e	3.63 ± 0.11	18.61 ± 0.88

Note. The correlations are in the form $Y = \alpha X + \beta$. Orthogonal distance regression was applied to find the best-fit parameters. All values are for the g' band. The galaxies of type “regular Es” are from Bender et al. (1992), i.e., the dark gray data points in Figure 16.

The average corrections for PSF broadening and the average systematic error due to the finite depth of our survey are indicated by the arrows. These average corrections and also the individual errors are neglected for the fitting of the parameter correlations. Otherwise, a significant number of data points had almost zero weight, due to the high inhomogeneity of the errors. We find that BCGs extend the population of regular ellipticals in parameter space to larger integrated brightnesses, dimmer effective SBs, and larger effective radii, but their parameter correlations have different slopes (see Table 3). In the next paragraphs, we compare our derived parameter correlations to those derived by Donzelli et al. (2011) and Bernardi et al. (2007) from shallower data sets and offer an explanation for the discrepancies. Later, we argue that the broken slopes appear because the growth of BCGs, compared to regular ellipticals, is more dominated by accretion of stellar material in their outskirts.

The Kormendy (1977) relation $SB_e = \alpha \log(r_e) + \beta$ that we fit to our data has a slope of $\alpha = 3.61 \pm 0.13$ for the SS BCGs and $\alpha = 3.58 \pm 0.26$ for the DS BCGs (see Table 3). Both results are in tension with the Kormendy relations found by Donzelli et al. (2011). Using shallower imaging data, they measured a slope of $\alpha = 3.29 \pm 0.06$ for the SS BCGs and $\alpha = 2.79 \pm 0.08$ for the DS BCGs. By also taking the offsets β after color corrections into consideration, we notice that the data points from Donzelli et al. are systematically shifted off our measured Kormendy relation toward smaller effective radii. A plausible explanation for this offset is the underestimation of the ICL amount in Donzelli et al.’s data because some upward curvature of the light profiles remained undetected. Their limiting SB converted to the g' band is $SB_{\text{lim}}^{\text{Donzelli+2011}} = 25.7 \text{ } g' \text{ mag arcsec}^{-2}$. In a forthcoming paper, we show that about half of the transitions between the two Sérsic components (and therefore a strong upward curvature in the SB profiles) occur below Donzelli et al.’s detection limit. The authors themselves pointed out that their measured correlation coefficients depend on the applied radius or surface brightness cuts.

Our measured size–luminosity relation $\log(r_e) = \alpha M + \beta$ has a slope $\alpha = -0.550 \pm 0.037$ for SS BCGs and $\alpha = -0.547 \pm 0.060$ for DS BCGs. That is significantly steeper than $\alpha = -0.354$

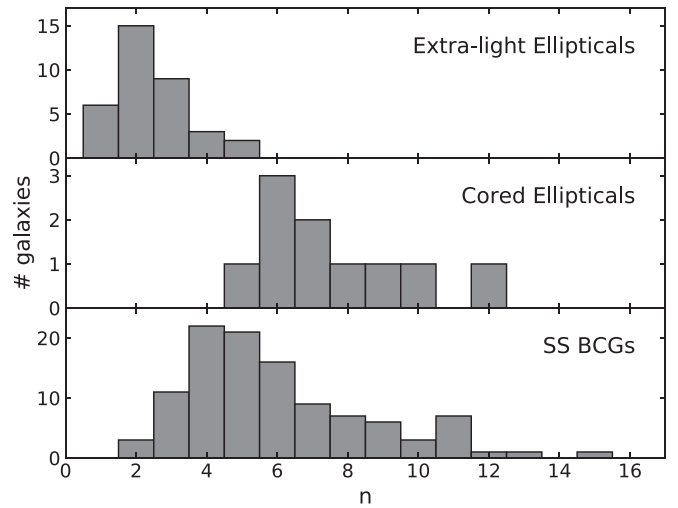


Figure 17. Distribution of Sérsic indices n for extra-light ellipticals (top panel), cored ellipticals (middle panel), and SS BCGs (bottom panel). The data for the extra-light and cored ellipticals are taken from Kormendy et al. (2009).

as measured by Bernardi et al. (2007). They fit SS functions to the semimajor axis SB profiles of 215 BCGs ($z < 0.12$), measured on SDSS DR2 r -band data. The average total brightness of the BCGs in the Bernardi et al. sample is 1–2 g' mag fainter than the BCGs in our sample. A different sample selection, preferentially toward lower mass clusters, could explain that discrepancy. Unfortunately, direct comparison of individual BCGs was not possible. Furthermore, the authors concluded from mock observations that undetected ICL shifts the data points along the size–luminosity relation but does not change its slope. However, our results disagree with their conclusion. For the brightest BCGs, we find larger effective radii than predicted by the size–luminosity relation as measured by Bernardi et al. (2007). In a forthcoming paper, we show that the fraction of light that is encompassed in the low-SB outskirts increases with total BCG+ICL brightness. That can lead to a shallower size–luminosity relation when that trend is not included in the models of Bernardi et al.

The trend that brighter BCGs have larger luminosity fractions in their low-SB outskirts offers an explanation for the broken slope in the size–luminosity relation and consequently also in the other two relations shown in Figure 16 and listed in Table 3. If BCGs are unique in growing predominantly by accreting stellar material into their outskirts, then their effective radii increase for a fixed brightness.

The same argument can also be made for galaxy clusters as a whole that grow purely by accretion. The slope of the size–luminosity relation is broken here once more. Compared to the BCGs, they are located at much larger radii but only slightly larger brightnesses (blue data points in Figure 16). The measurements of the cluster parameters will be discussed in a forthcoming paper.

We notice from further inspecting Figure 16 that SS BCGs have a smaller median effective radius and a brighter median effective surface brightness ($45 \pm 24 \text{ kpc}$; $22.4 \pm 0.9 \text{ } g' \text{ mag arcsec}^{-2}$) compared to their DS counterparts ($72 \pm 31 \text{ kpc}$; $25.5 \pm 0.8 \text{ } g' \text{ mag arcsec}^{-2}$). The slightly more compact shape of SS BCGs is also seen in the average SB profiles in Figure 15. In integrated brightnesses, SS BCGs are 14.8% fainter ($-23.68 \pm 0.53 \text{ } g' \text{ mag}$) than DS BCGs ($-23.83 \pm 0.41 \text{ } g' \text{ mag}$).

The distribution of Sérsic indices n for all SS BCGs is shown in Figure 17. Most SS BCGs have $n \geq 4$, but 20/121 (17%)

have significantly lower n . That value approximately separates the two classes of disk–coreless–rotating ellipticals (denoted extra-light ellipticals in the histogram) and boxy–core–nonrotating ellipticals (Kormendy et al. 2009). We further elaborate on that dichotomy in the next subsection. The high Sérsic indices can be explained by accretion that is predominantly happening in the outskirts, which subsequently increases the upward curvature of the SB profiles and consequently the Sérsic indices.

7. Discussion

7.1. Do BCGs Form a Unique Class of Elliptical Galaxies?

We compare the structural parameters of BCGs to those of regular ellipticals in Figure 16. Spheroidals and ellipticals including classical bulges populate different areas in parameter space, which indicates that they are formed by different formation scenarios (Kormendy et al. 2009). BCGs also do not follow the correlations for regular ellipticals. The slopes are steeper. The downward trend of the Kormendy and $M_{\text{tot}} \propto \text{SB}_e$ relations in Figure 16 illustrates the growing importance of the low-surface-brightness stellar halo and ICL contribution of ellipticals with increasing luminosity because half of the light is below the effective surface brightness. The broken slopes of these relations underline that the stellar halos and ICL are even more important for BCGs; that is, their growth is even more dominated by accretion in their low-SB outskirts (e.g., Oser et al. 2010). We emphasize that we do not try to dissect the ICL or stellar halos from the BCGs in this work and instead consider their combined stellar light.

The effective radii are also larger than what would be expected from extrapolating the size–luminosity relation $M_{\text{tot}} \propto \log(r_e)$ for regular ellipticals. All these findings confirm the picture that regular ellipticals and BCGs differ from each other in the importance of accretion in their formation history. BCGs reside near the center of their host cluster. Contrary to regular ellipticals, that enables them to accumulate enormous amounts of stellar material instead of being tidally stripped by the cluster potential.

7.2. Is the Inner Component of DS BCGs “Extra Light”?

An alternative explanation for the origin of DS profile shapes could be due to a central poststarburst stellar population as is often seen in extra-light ellipticals (e.g., Faber et al. 1997; Kormendy 1999; Kormendy et al. 2009; Kormendy & Bender 2013). There are two families of ellipticals: boxy–core–nonrotating and disk–extra-light–rotating (Bender 1988; Bender et al. 1988, 1989, 1991; Kormendy & Bender 1996; Kormendy et al. 2009). Most BCGs are categorized as boxy–core–nonrotating galaxies, which is further confirmed by the distribution of Sérsic indices (see Section 6.3). Those ellipticals are believed to have formed via dissipationless merging and subsequent violent relaxation. However, judging from the SB profiles in Appendix A, there are some BCGs that could potentially be categorized as unusually massive extra-light ellipticals. Non-BCG extra-light ellipticals have small transition radii of $r_{\times} \lesssim 1$ kpc (Hopkins et al. 2009; Kormendy et al. 2009) or $r_{\times} < 0.04r_e$ (Mihos & Hernquist 1994). A light excess above the inward extrapolation of the outer Sérsic profile is interpreted to arise from a poststarburst stellar population that was formed after a wet merger. The origin of the DS shape would then be unrelated to the ICL phenomenon. Those BCGs can bias the

structural parameter relations and correlations with cluster properties.

By conservatively selecting only DS BCGs that have transition radii $r_{\times} \gtrsim 0.1r_e$ and transition surface brightness $\text{SB}_{\times} > 23$ g' mag arcsec^{−2}, we discard 49/98 BCGs from the DS sample that are potentially extra-light ellipticals and classify them as SS BCGs. The structural parameter relations between r_e , SB_e , and M_{tot} for both split samples do not differ significantly from each other.

Furthermore, we inspect the isophotal distortions a_4 of the potential extra-light ellipticals. Extra light is frequently observed to have disk-like isophotes when viewed edge-on (e.g., Section 9.3 in Kormendy et al. 2009). At least some of the 49 potential extra-light BCGs in our sample should have high inclinations. Therefore, we expect the average a_4 to be higher in the inner regions for the potential extra-light BCG subsample than for the rest of the DS BCGs. We do not find that. The isophotes of the potential extra-light ellipticals are not diskier near the transition radii than those of the BCGs that have no potential extra light.

The abundance of multiple cores for potential extra-light ellipticals would increase if some of them are the remnants of wet mergers. Contrary to that expectation, it is even less. Also, malicious handling of overlapping galaxies is thereby excluded as an artificial origin of small r_{\times} DS profiles.

All 18 BCGs that overlap with the Lauer et al. (2007) sample (A76, A193, A260, A347, A376, A397, A634, A999, A1016, A1020, A1142, A1177, A1656, A1831, A2052, A2147, A2199, and A2589) are classified by the authors as cored ellipticals. The decisions were made based on high-resolution *HST* images. Six of those BCGs are classified by our criteria as potential extra-light ellipticals: A193, A260, A397, A1020, A2147, and A2589; that is, the SB profiles have a core inside a potential extra-light region. This will break the known dichotomy if the extra light will be confirmed to form in the same poststarburst scenario as is the case for lower mass ellipticals.

7.3. Do DS BCGs Differ from SS BCGs in Their Evolutionary State?

The members of both Sérsic types are, in general, very similar in their appearance. Both families follow the same structural parameter correlations (see Figure 16 and Table 3). Any characteristic that qualifies each Sérsic type as distinct might be subtle. Nevertheless, there are differences beyond the simple number of analytic functions that are needed to fit their light profiles well.

First of all, we take a closer look at the average profiles presented in Figure 15. The clearest discrepancy is found in the ellipticity ϵ profiles. DS BCGs are, on average, rounder at small radii $r = \sqrt{ab} < 16$ kpc and become more elliptical at larger radii. This is qualitatively consistent with the discovery by Donzelli et al. (2011). DS BCGs furthermore have lower scatter in position angle drifts $\Delta\text{PA}(r)$, that is, smaller isophote twists for individual galaxies.⁵ And finally, DS BCGs have on average less boxy isophotes ($a_4^{\text{DS}} > a_4^{\text{SS}}$). We must note here that boxy isophotes also result from shells (González-García & van Albada 2005), which are actually marginally more common for SS BCGs (see Figure 14). Nevertheless, all of these tendencies are identical with those of more rotationally supported and thus less evolved systems. The spatial offsets

⁵ The larger scatter at small radii can be attributed to the smaller ellipticities that increase the uncertainty of the PA measurement.

between the ICL and the BCG are on average larger for DS BCGs. This is related to the higher abundance of multiple nuclei (see Figure 14) that drag the main nucleus along by their gravitational attraction. The analog to ICL offsets in velocity space is systemic velocity offsets, that is, the line-of-sight velocity difference between the BCG and the average cluster line-of-sight velocity. We have examined the distributions of systemic velocity offsets for SS and DS BCGs separately using published data from Lauer et al. (2014). A Kolmogorov–Smirnov test showed that no conclusion can be drawn from those data.

The isophotal parameters that describe asymmetric distortions a_3 , b_3 , and b_4 are higher for DS BCGs (see Figure 15). Such shapes are not stable and are therefore evidence for ongoing accretion. The larger abundance of signatures from these accretion processes is also documented in Figure 14. These features are relatively short-lived because they are dynamically hot. They originate from collisions and stripping events with high relative velocities of order $\sim 1000 \text{ km s}^{-1}$. Because these remnants are visible today, DS BCGs must have undergone more of these events recently.

We mentioned before that any dichotomy between SS and DS BCGs is subtle. Most of our distinctions are not very significant, but they all point to the same conclusion. SS BCGs are currently in a more relaxed state because they have experienced fewer accretion events in the recent past. Either the earlier accreted stellar mass has already virialized by violent relaxation, or the events that would create a distinctly visible envelope have not yet taken place.

8. Summary and Conclusion

We have obtained optical g' -band observations of 170 galaxy clusters with the Wendelstein Wide Field Imager. The data reduction pipeline was developed and assembled specifically for that instrument and optimized for low-surface-brightness photometry.

We have measured semimajor axis surface brightness profiles of the BCGs down to a limiting surface brightness of $SB_{\text{lim}} = 30 \text{ g' mag arcsec}^{-2}$, which is an unprecedented depth for a large sample size.

Our results are summarized as follows:

(1) BCGs have larger effective radii, dimmer effective surface brightnesses, and brighter absolute magnitudes than expected for an extrapolation of the parameter correlations for regular ellipticals. The Kormendy, the size–luminosity, and the $M_{\text{tot}}\text{--}SB_e$ relations have broken slopes at least in part because of the presence of ICL around the BCGs.

(2) By fitting Sérsic functions to the semimajor axis SB profiles, we find that 71% of the observed BCGs are well described by a single Sérsic function (SS BCGs). The remaining 29% of BCGs have variations in the slope of their SB profiles that require using two Sérsic functions to obtain a good fit (DS BCGs). DS BCGs with transition radii $r_{\times} < 0.1 r_e$ and transition surface brightnesses $SB_{\times} < 23 \text{ g' mag arcsec}^{-2}$ were fitted with a single Sérsic function excluding the inner excess light. The DS profile shape is more likely to arise in those cases because of a poststarburst stellar population following a wet merger than because of the ICL phenomenon.

(3) SS and DS BCGs do not deviate significantly from each other in their parameter correlations between effective radii a_e along the major axis, effective surface brightnesses SB_e , and integrated absolute brightnesses M_{tot} .

(4) SS BCGs are slightly more compact ($r_e^{\text{SS}} = 45 \pm 24 \text{ kpc}$) than DS BCGs ($r_e^{\text{DS}} = 72 \pm 31 \text{ kpc}$). In integrated brightnesses, SS BCGs are 14.8% fainter ($-23.68 \pm 0.53 \text{ g' mag}$) than DS BCGs ($-23.83 \pm 0.41 \text{ g' mag}$).

(5) The Sérsic indices of SS BCGs are significantly larger than $n \geq 4$ in 83% of the cases. That value approximately separates the two classes of disk–coreless–rotating ellipticals and boxy–core–nonrotating ellipticals.

(6) The radial profiles of their structural parameters show that SS BCGs have on average

1. shallower ellipticity profiles,
2. stronger individual isophote twists,
3. smaller ICL offsets,
4. boxier isophotes,
5. less pronounced asymmetric isophotal distortions, and
6. fewer accretion signatures

than DS BCGs. We deduce from these results that SS BCGs are on average marginally more relaxed because they have encountered fewer accretion events in the recent past. The tendencies are identical to those of more triaxial and dispersion supported, that is, more evolved systems.

(7) The average isophote twists are $\Delta\text{PA}/\Delta r \sim 10^\circ/100 \text{ kpc}$.

(8) The average ellipticity increases with radius and reaches $\epsilon = 0.4\text{--}0.5$ at a circular radius of $r \approx 200 \text{ kpc}$.

(9) The isophotal offset with respect to the nucleus increases with radius. At 200 kpc circular galactocentric radius from the nucleus, the average offset is 37 kpc with 34 kpc intrinsic scatter.

We conclude from our study that BCG+ICLs have scaling relations with steeper slopes than those for normal non-BCG ellipticals. That is likely because the faint ICL outskirts around BCGs have a significant influence on the structural parameters. Our deep SB profiles enable us furthermore to decide more consistently whether an SB profile is well described by an SS or DS profile. The former case is more common (71%) at redshift $z = 0.06$; that is, most of the BCG+ICLs have relatively smooth SB profiles. Whether the photometrically distinct stellar envelopes around the rarer DS BCGs trace the ICL is debated. We have shown that the isophotal shapes of DS BCGs are more disturbed and accretion signatures are more common inside them than in SS BCGs. Hence, it is possible that the envelopes are simply the result of unrelaxed, recently accreted material and not necessarily the signature of pure ICL. On the other hand, it could also be that SS BCGs have not yet accumulated sufficient stellar material to build up a distinct ICL envelope. We will further address that question in a forthcoming paper where we compare different photometric methods to dissect the ICL from the BCGs. Lastly, we have shown in Figure 16 that the size–brightness relation curves upward toward host cluster data points. In other words, the ICL transitions smoothly into the galaxy clusters. We will explore further correlations between BCG/ICL and host cluster properties in the same forthcoming paper.

We are grateful to Rhea-Silvia Remus, Klaus Dolag, Stella Seitz, John Kormendy, Tod Lauer, and Walter Dehnen for helpful conversations and constructive feedback on the manuscript. We also wish to thank the anonymous referee for his or her comments and suggestions that allowed us to significantly improve the paper.

The 2 m telescope project is funded by the Bavarian government and by the German Federal government through

a common funding process. Part of the 2 m instrumentation including some of the upgrades for the infrastructure and the 40 cm telescope housing were funded by the Cluster of Excellence “Origin of the Universe” of the German Science foundation DFG. The 40 cm telescope was funded by the Ludwig-Maximilians-University, Munich.

This work made use of data products based on observations made with the NASA/ESA *Hubble Space Telescope* and obtained from the Hubble Legacy Archive, which is a collaboration between the Space Telescope Science Institute (STScI/NASA), the Space Telescope European Coordinating Facility (ST-ECF/ESA), and the Canadian Astronomy Data Centre (CADC/NRC/CSA).

This work would not have been practical without extensive use of NASA’s Astrophysics Data System Bibliographic Services and the SIMBAD database, operated at CDS, Strasbourg, France.

We also used the image display tool SAOImage DS9 developed by Smithsonian Astrophysical Observatory and the image display tool Fitsedit, developed by Johannes Koppenhoefer.

This research made use of Astropy, a community-developed core Python package for Astronomy (Astropy Collaboration et al. 2013).

Facilities: WO:2m (Wide-field camera), *HST* (WFPC2, ACS), Planck (HFI).

Appendix A Surface Brightness Profiles and Sérsic Fits

The SB profiles, ellipticity profiles, and PA profiles of all BCGs in our sample are shown in Figure 18 as data points. Sérsic profiles with the best-fit parameters (see Appendix C) are overplotted as lines.

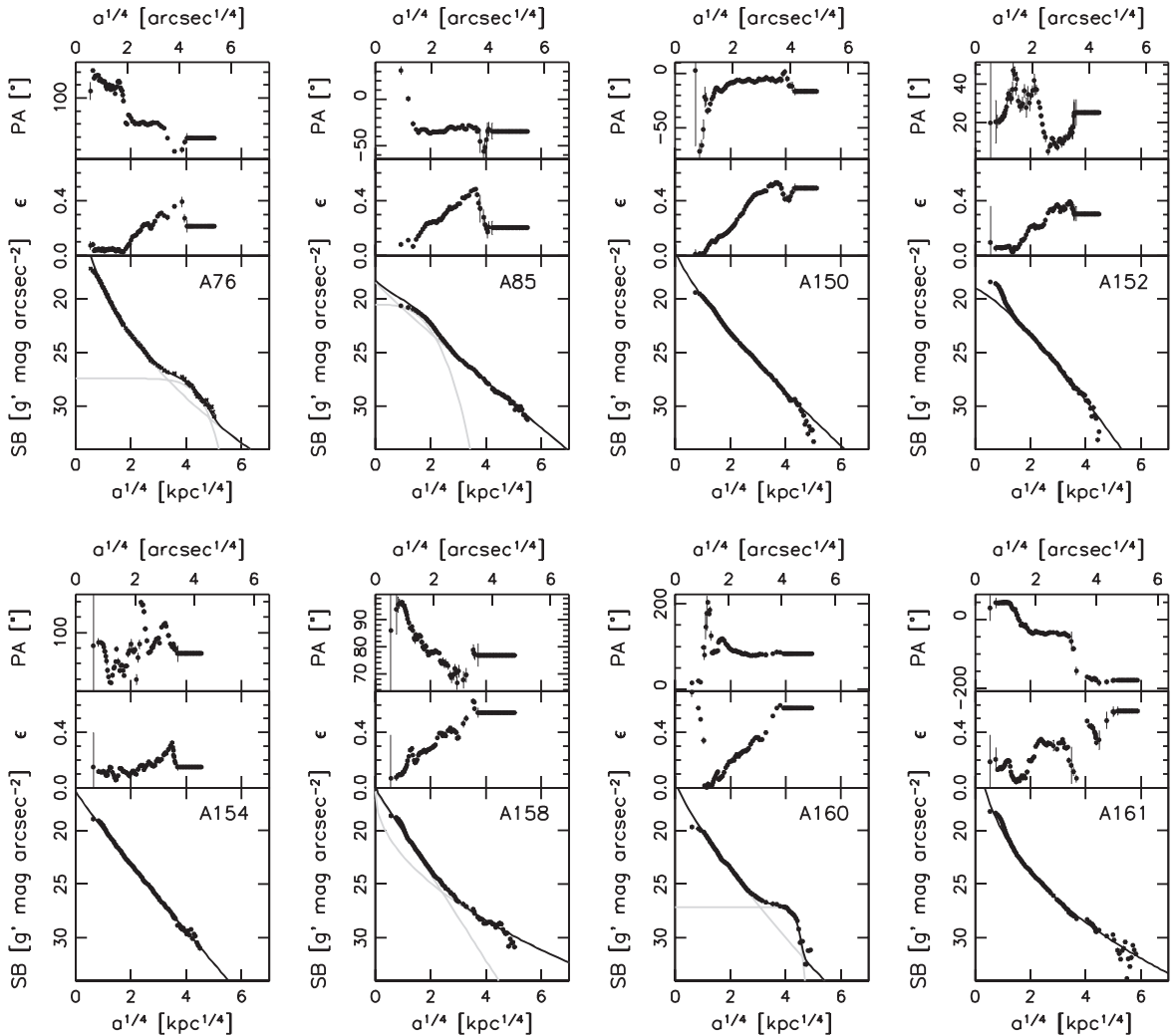


Figure 18. SB profiles are corrected for PSF broadening. No K-correction and no corrections for dust extinction and cosmic dimming are applied. If the SB profiles were fitted by a double Sérsic function, then the light gray lines show the contributions of each component. Ellipticity and position angle profiles are presented in the middle and top panels, respectively. (An extended version of this figure is available.)

Appendix B Image Cutouts

Figure 19 shows our observations, centered on the BCGs. They are all rescaled to the same physical size.

Appendix C Structural Parameters of the BCG+ICLs

Table 4 lists the structural parameters of the BCG+ICLs, that is, the best-fit Sérsic parameters, and parameters, which are derived by direct integration of the light profiles.

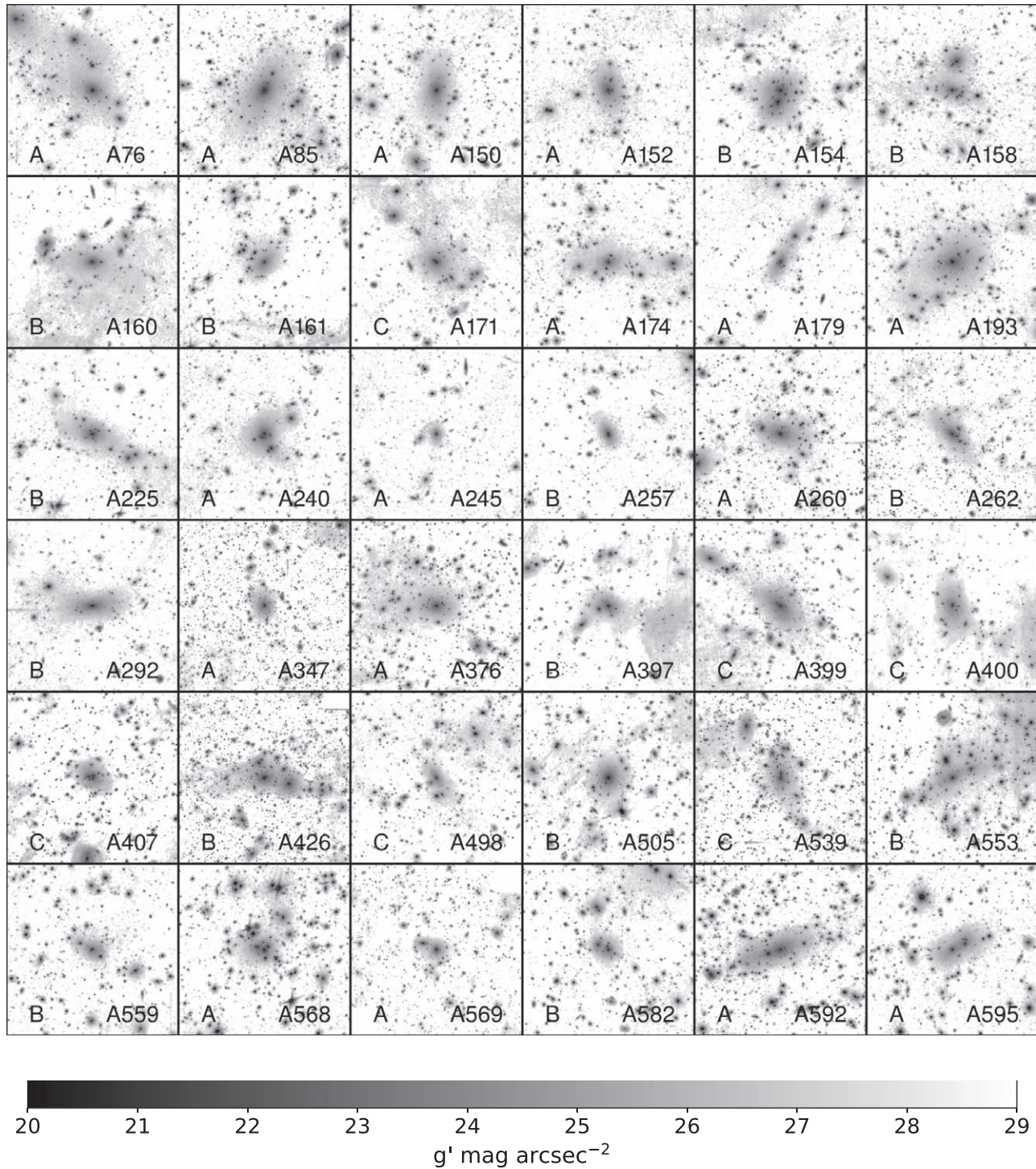


Figure 19. Image cutouts, centered on all BCGs that are analyzed in this study. The side length of each box is 750 kpc. North is up and east is left. (An extended version of this figure is available.)

Table 4
Structural Parameters of the BCG+ICLs

Cluster	First Semimajor Axis Sérsic Component			Second Semimajor Axis Sérsic Component			$S_2/(S_1 + S_2)$	Parameters from 2D Profile Integration			Feature
	n_1	$r_{e,1}$ (kpc)	$SB_{e,1}$ ($g' \text{ mag}''^{-2}$)	n_2	$r_{e,2}$ (kpc)	$SB_{e,2}$ ($g' \text{ mag}''^{-2}$)		r_e (kpc)	SB_e ($g' \text{ mag}''^{-2}$)	M_{tot} ($g' \text{ mag}$)	
(1)	(2)	(3)	(4)	(5)	(6)	(7)	(8)	(9)	(10)	(11)	(12)
A76	10.24 ± 1.14	$79.43^{+29.66}_{-23.16}$	26.15 ± 0.63	0.46 ± 0.08	$249.7^{+6.95}_{-6.81}$	27.66 ± 0.10	0.38 ± 0.06	147.0 ± 20.37	26.51 ± 0.06	-24.14 ± 0.07	d
A85	1.26 ± 0.29	$15.81^{+0.87}_{-0.84}$	22.43 ± 0.18	4.21 ± 0.70	$208.1^{+10.48}_{-10.10}$	26.74 ± 0.10	0.83 ± 0.04	139.1 ± 32.81	25.84 ± 0.40	-24.79 ± 0.10	...
A150	5.06 ± 0.25	$84.98^{+4.48}_{-4.31}$	25.61 ± 0.11	52.19 ± 5.66	24.57 ± 0.18	-23.81 ± 0.06	cd
A152	3.13 ± 0.09	$56.51^{+1.14}_{-1.13}$	24.97 ± 0.05	44.02 ± 2.15	24.50 ± 0.06	-23.55 ± 0.03	...
A154	4.28 ± 0.18	$51.08^{+1.38}_{-1.35}$	24.59 ± 0.06	43.09 ± 2.93	24.24 ± 0.10	-24.01 ± 0.04	ad
A158	3.90 ± 2.39	$19.24^{+44.43}_{-15.78}$	23.78 ± 1.10	7.95 ± 34.21	$3980^{+7.0E5}_{-2.9E4}$	32.65 ± 19.64	0.84 ± 0.26	1601 ± 1409	29.74 ± 2.32	-24.60 ± 0.60	...
A160	4.96 ± 0.31	$46.13^{+5.73}_{-5.24}$	25.08 ± 0.22	0.17 ± 0.02	$167.4^{+91.10}_{-64.60}$	26.58 ± 0.05	0.54 ± 0.08	130.4 ± 2.31	26.16 ± 0.01	-23.91 ± 0.01	d
A161	11.37 ± 1.55	$863.5^{+436.9}_{-316.3}$	30.28 ± 0.83	406.5 ± 277.3	28.25 ± 1.53	-24.43 ± 0.36	c
A171	5.98 ± 0.46	$21.39^{+1.64}_{-1.55}$	23.36 ± 0.15	0.27 ± 0.02	$236.3^{+3.06}_{-3.03}$	26.76 ± 0.04	0.52 ± 0.02	103.2 ± 1.33	26.01 ± 0.03	-24.27 ± 0.01	...
A174	9.89 ± 1.11	$113.9^{+45.75}_{-35.14}$	26.97 ± 0.66	0.38 ± 0.08	$264.6^{+8.22}_{-8.03}$	27.85 ± 0.11	0.30 ± 0.05	86.95 ± 13.94	26.06 ± 0.10	-23.85 ± 0.06	...
A179	8.66 ± 0.88	$100.9^{+34.47}_{-27.43}$	26.63 ± 0.57	0.53 ± 0.17	$382.3^{+28.75}_{-27.21}$	28.46 ± 0.13	0.37 ± 0.06	141.8 ± 26.63	26.77 ± 0.16	-23.64 ± 0.07	cd
A193	7.79 ± 0.98	$243.1^{+41.03}_{-36.42}$	27.38 ± 0.33	181.1 ± 67.92	26.55 ± 0.64	-24.67 ± 0.18	d
A225	10.54 ± 1.37	$284.1^{+91.64}_{-73.76}$	28.14 ± 0.58	98.82 ± 42.02	25.79 ± 0.79	-24.04 ± 0.18	...
A240	4.22 ± 0.16	$53.47^{+1.47}_{-1.44}$	24.89 ± 0.06	40.36 ± 2.35	24.21 ± 0.10	-23.74 ± 0.04	...
A245	5.05 ± 0.53	$16.09^{+0.81}_{-0.78}$	23.78 ± 0.10	11.61 ± 0.50	23.16 ± 0.09	-22.43 ± 0.02	...
A257	2.92 ± 0.16	$21.81^{+0.51}_{-0.50}$	23.33 ± 0.05	17.46 ± 0.33	22.88 ± 0.03	-23.02 ± 0.01	...
A260	7.58 ± 0.53	$115.0^{+13.55}_{-12.45}$	26.47 ± 0.23	53.07 ± 10.64	24.87 ± 0.42	-23.60 ± 0.10	...
A262	2.96 ± 0.11	$54.26^{+1.32}_{-1.29}$	25.02 ± 0.06	32.70 ± 1.18	24.11 ± 0.06	-22.89 ± 0.02	d
A292	4.57 ± 0.19	$81.07^{+2.85}_{-2.78}$	24.92 ± 0.08	66.02 ± 6.35	24.51 ± 0.13	-24.01 ± 0.05	...
A347	7.54 ± 0.54	$36.97^{+3.37}_{-3.15}$	25.26 ± 0.19	27.57 ± 3.94	24.51 ± 0.26	-22.60 ± 0.08	d
A376	11.17 ± 1.00	$446.3^{+116.5}_{-97.41}$	29.10 ± 0.47	244.3 ± 147.5	27.48 ± 1.34	-24.24 ± 0.29	...
A397	5.66 ± 0.35	$55.34^{+3.93}_{-3.74}$	25.14 ± 0.15	38.04 ± 4.09	24.23 ± 0.24	-23.42 ± 0.06	c
A399	2.85 ± 0.11	$65.11^{+1.72}_{-1.68}$	24.20 ± 0.06	58.36 ± 1.51	23.91 ± 0.05	-24.39 ± 0.02	c
A400	4.52 ± 0.90	$4.92^{+1.46}_{-1.20}$	21.94 ± 0.51	1.05 ± 0.09	$65.23^{+1.67}_{-1.64}$	25.10 ± 0.07	0.79 ± 0.02	46.56 ± 0.39	24.68 ± 0.01	-23.20 ± 0.01	d
A407	1.90 ± 0.14	$34.91^{+1.28}_{-1.25}$	23.45 ± 0.09	29.50 ± 0.22	23.03 ± 0.02	-23.77 ± 0.01	d
A426	4.25 ± 0.28	$14.55^{+1.32}_{-1.23}$	22.42 ± 0.17	0.44 ± 0.04	$97.04^{+1.42}_{-1.41}$	25.86 ± 0.07	0.37 ± 0.03	30.46 ± 0.30	23.75 ± 0.02	-23.64 ± 0.00	d
A498	5.38 ± 0.39	$98.41^{+9.35}_{-8.73}$	25.39 ± 0.19	55.21 ± 6.92	24.29 ± 0.21	-24.12 ± 0.06	b
A505	4.45 ± 0.17	$30.15^{+0.66}_{-0.65}$	23.43 ± 0.05	27.45 ± 0.90	23.12 ± 0.06	-24.00 ± 0.02	...
A539	4.44 ± 0.72	$45.65^{+21.11}_{-15.66}$	24.99 ± 0.66	0.42 ± 0.10	$97.99^{+2.44}_{-2.39}$	25.93 ± 0.16	0.37 ± 0.11	59.06 ± 3.11	24.85 ± 0.09	-23.49 ± 0.03	d
A553	2.66 ± 0.38	$7.14^{+1.19}_{-1.06}$	21.55 ± 0.27	2.62 ± 0.33	$505.6^{+64.47}_{-58.84}$	27.22 ± 0.23	0.93 ± 0.01	405.4 ± 47.01	26.73 ± 0.06	-25.35 ± 0.09	...
A559	2.73 ± 0.59	$3.34^{+0.57}_{-0.50}$	20.81 ± 0.28	1.75 ± 0.18	$51.18^{+2.53}_{-2.44}$	25.08 ± 0.11	0.75 ± 0.04	29.36 ± 0.80	24.02 ± 0.03	-23.25 ± 0.02	...
A568	25.83 ± 11.10	$228.5^{+284.6}_{-145.7}$	28.10 ± 1.88	191.4 ± 139.2	26.89 ± 2.01	-24.35 ± 0.32	...
A569	4.60 ± 0.21	$9.76^{+0.29}_{-0.29}$	22.59 ± 0.06	9.95 ± 0.20	22.49 ± 0.04	-22.26 ± 0.01	d
A582	9.41 ± 1.38	$69.87^{+12.36}_{-10.91}$	26.14 ± 0.35	52.96 ± 18.66	25.51 ± 1.02	-23.56 ± 0.14	...
A592	2.44 ± 0.13	$122.2^{+5.81}_{-5.61}$	25.21 ± 0.10	87.88 ± 2.98	24.40 ± 0.06	-24.31 ± 0.02	cd
A595	8.26 ± 1.46	$8.71^{+2.46}_{-2.03}$	22.68 ± 0.50	0.77 ± 0.07	$61.35^{+1.08}_{-1.07}$	25.34 ± 0.06	0.55 ± 0.04	34.36 ± 0.83	24.32 ± 0.02	-23.15 ± 0.01	a
A600	3.93 ± 0.20	$27.38^{+1.64}_{-1.57}$	23.97 ± 0.12	0.42 ± 0.18	$355.8^{+29.61}_{-27.87}$	29.48 ± 0.19	0.29 ± 0.04	59.45 ± 8.92	25.71 ± 0.53	-23.57 ± 0.06	d
A602	3.53 ± 0.31	$30.25^{+6.15}_{-5.34}$	24.66 ± 0.31	1.14 ± 0.16	$391.2^{+20.67}_{-19.88}$	27.70 ± 0.11	0.71 ± 0.03	172.0 ± 13.04	26.43 ± 0.04	-23.87 ± 0.04	c
A607	2.67 ± 0.28	$126.0^{+14.45}_{-13.30}$	26.43 ± 0.22	121.7 ± 16.37	26.41 ± 0.45	-23.86 ± 0.08	...
A612	20.24 ± 14.22	$199.4^{+389.8}_{-154.5}$	28.98 ± 2.60	106.7 ± 78.96	26.81 ± 2.01	-23.11 ± 0.31	...

Table 4
(Continued)

Cluster	First Semimajor Axis Sérsic Component			Second Semimajor Axis Sérsic Component			$S_2/(S_1 + S_2)$	Parameters from 2D Profile Integration			Feature
	n_1	$r_{e,1}$ (kpc)	$SB_{e,1}$ (g' mag $^{n-2}$)	n_2	$r_{e,2}$ (kpc)	$SB_{e,2}$ (g' mag $^{n-2}$)		r_e (kpc)	SB_e (g' mag $^{n-2}$)	M_{tot} (g' mag)	
(1)	(2)	(3)	(4)	(5)	(6)	(7)	(8)	(9)	(10)	(11)	(12)
A634	7.14 ± 0.57	$22.81^{+1.24}_{-1.19}$	24.17 ± 0.12	24.07 ± 3.09	24.40 ± 0.24	-22.69 ± 0.06	b
A671	3.57 ± 0.16	$44.18^{+1.31}_{-1.28}$	24.05 ± 0.07	40.45 ± 1.44	23.76 ± 0.05	-23.99 ± 0.02	...
A688	3.98 ± 0.19	$41.54^{+0.83}_{-0.82}$	23.87 ± 0.04	39.34 ± 1.61	23.73 ± 0.09	-24.27 ± 0.03	...
A690	3.88 ± 0.19	$53.45^{+1.73}_{-1.69}$	24.59 ± 0.07	41.56 ± 2.17	24.04 ± 0.08	-24.09 ± 0.03	...
A695	3.92 ± 0.25	$20.80^{+0.75}_{-0.73}$	23.11 ± 0.08	20.48 ± 0.69	23.02 ± 0.08	-23.40 ± 0.02	d
A734	3.52 ± 0.18	$24.94^{+0.66}_{-0.65}$	23.80 ± 0.06	20.49 ± 0.65	23.36 ± 0.07	-23.23 ± 0.02	...
A744	17.44 ± 2.28	$142.8^{+32.98}_{-28.10}$	27.39 ± 0.45	114.8 ± 66.44	26.53 ± 1.34	-24.03 ± 0.25	...
A757	9.20 ± 1.09	$38.77^{+10.41}_{-8.66}$	25.53 ± 0.48	0.46 ± 0.16	$227.8^{+14.11}_{-13.49}$	28.93 ± 0.15	0.26 ± 0.05	62.10 ± 12.01	26.30 ± 0.44	-23.04 ± 0.07	...
A834	3.70 ± 0.32	$36.13^{+5.80}_{-5.17}$	24.14 ± 0.27	0.38 ± 0.08	$199.8^{+5.89}_{-5.76}$	26.75 ± 0.09	0.48 ± 0.04	98.28 ± 1.96	25.81 ± 0.07	-23.94 ± 0.01	...
A883	18.08 ± 3.28	$2.1E3^{+2.0E3}_{-1.1E3}$	32.40 ± 1.45	$9.8E2 \pm 8.9E2$	29.31 ± 2.90	-24.26 ± 0.54	...
A999	8.02 ± 0.66	$32.61^{+2.37}_{-2.24}$	24.86 ± 0.15	20.98 ± 2.34	23.90 ± 0.16	-22.71 ± 0.05	c
A1003	4.31 ± 0.33	$36.78^{+1.82}_{-1.76}$	24.54 ± 0.11	25.45 ± 1.36	23.63 ± 0.11	-23.18 ± 0.03	...
A1016	21.23 ± 4.11	$163.0^{+90.82}_{-63.95}$	28.56 ± 0.97	79.53 ± 53.95	26.50 ± 1.72	-22.93 ± 0.29	c
A1020	5.62 ± 0.53	$24.36^{+1.17}_{-1.13}$	24.11 ± 0.10	19.58 ± 1.57	23.69 ± 0.13	-23.14 ± 0.04	...
A1056	3.55 ± 0.20	$65.15^{+2.44}_{-2.38}$	25.38 ± 0.08	43.42 ± 2.53	24.50 ± 0.08	-23.64 ± 0.04	...
A1066	2.20 ± 0.22	$7.67^{+0.90}_{-0.82}$	21.82 ± 0.18	1.91 ± 0.30	$125.9^{+6.42}_{-6.19}$	26.62 ± 0.11	0.73 ± 0.03	72.69 ± 6.01	25.71 ± 0.15	-23.68 ± 0.04	d
A1100	6.87 ± 0.27	$53.62^{+2.03}_{-1.98}$	25.34 ± 0.08	33.82 ± 4.71	24.32 ± 0.26	-23.18 ± 0.07	c
A1108	8.45 ± 1.01	$28.66^{+3.37}_{-3.27}$	25.50 ± 0.26	24.12 ± 6.22	25.06 ± 0.52	-21.91 ± 0.11	cd
A1142	6.10 ± 0.56	$23.57^{+1.38}_{-1.32}$	23.96 ± 0.13	23.30 ± 1.83	23.76 ± 0.10	-22.95 ± 0.04	bcd
A1155	10.04 ± 1.02	$61.36^{+5.66}_{-5.29}$	25.80 ± 0.19	34.94 ± 8.40	24.52 ± 0.54	-23.27 ± 0.11	...
A1173	5.52 ± 0.49	$83.91^{+19.15}_{-16.35}$	26.04 ± 0.39	0.35 ± 0.12	$443.2^{+27.33}_{-26.12}$	28.68 ± 0.16	0.39 ± 0.05	174.7 ± 16.46	27.12 ± 0.09	-24.26 ± 0.04	d
A1177	7.46 ± 1.61	$28.62^{+29.08}_{-16.40}$	24.61 ± 1.31	1.38 ± 0.24	$72.57^{+3.32}_{-3.21}$	25.51 ± 0.10	0.53 ± 0.14	40.15 ± 1.45	24.21 ± 0.03	-23.41 ± 0.02	bc
A1185	6.36 ± 1.01	$24.46^{+2.18}_{-2.04}$	23.69 ± 0.19	29.76 ± 2.89	24.31 ± 0.17	-23.25 ± 0.05	d
A1187	12.79 ± 2.03	$149.0^{+41.06}_{-34.02}$	27.12 ± 0.52	66.69 ± 25.34	25.48 ± 0.90	-23.95 ± 0.16	a
A1190	2.09 ± 0.24	$25.66^{+3.29}_{-3.00}$	23.26 ± 0.21	0.66 ± 0.09	$188.7^{+7.98}_{-7.74}$	26.43 ± 0.12	0.54 ± 0.04	71.25 ± 1.08	24.96 ± 0.02	-24.13 ± 0.01	a
A1203	7.09 ± 0.51	$41.24^{+6.46}_{-5.78}$	24.71 ± 0.29	0.63 ± 0.11	$309.7^{+11.10}_{-10.81}$	28.31 ± 0.09	0.37 ± 0.04	102.5 ± 9.87	26.22 ± 0.13	-24.11 ± 0.04	...
A1213	1.60 ± 0.17	$6.38^{+0.42}_{-0.40}$	21.23 ± 0.08	3.20 ± 1.36	$106.8^{+14.77}_{-13.39}$	27.30 ± 0.28	0.60 ± 0.08	31.21 ± 5.41	24.94 ± 0.24	-23.03 ± 0.06	c
A1218	10.98 ± 1.69	$149.7^{+86.54}_{-60.26}$	28.26 ± 0.92	0.35 ± 0.17	$407.0^{+37.39}_{-34.98}$	29.66 ± 0.22	0.28 ± 0.09	165.7 ± 58.25	27.89 ± 0.61	-23.25 ± 0.15	...
A1228	3.49 ± 0.11	$21.41^{+0.37}_{-0.37}$	23.18 ± 0.04	21.59 ± 0.40	23.15 ± 0.04	-23.23 ± 0.01	cd
A1257	2.09 ± 0.32	$2.39^{+0.22}_{-0.20}$	20.77 ± 0.16	1.76 ± 0.16	$52.39^{+1.63}_{-1.60}$	25.56 ± 0.07	0.77 ± 0.02	26.73 ± 0.73	24.39 ± 0.03	-22.35 ± 0.02	c
A1270	2.51 ± 0.10	$18.01^{+0.42}_{-0.41}$	23.28 ± 0.05	15.03 ± 0.18	22.94 ± 0.02	-22.89 ± 0.01	...
A1275	14.93 ± 2.60	$9.17^{+1.60}_{-1.41}$	22.32 ± 0.36	18.98 ± 4.11	23.89 ± 0.49	-22.76 ± 0.10	...
A1279	2.57 ± 0.10	$20.53^{+0.42}_{-0.42}$	23.55 ± 0.04	16.44 ± 0.27	23.16 ± 0.03	-22.70 ± 0.01	...
A1314	6.56 ± 1.51	$7.29^{+2.44}_{-1.95}$	22.05 ± 0.58	1.18 ± 0.07	$71.91^{+0.99}_{-0.98}$	25.23 ± 0.07	0.63 ± 0.05	37.27 ± 0.52	24.10 ± 0.02	-23.29 ± 0.01	c
A1324	6.12 ± 0.72	$19.46^{+2.15}_{-1.98}$	23.54 ± 0.22	0.69 ± 0.19	$478.3^{+50.14}_{-46.48}$	28.83 ± 0.20	0.59 ± 0.04	232.0 ± 33.94	27.96 ± 0.18	-24.38 ± 0.07	...
A1356	4.97 ± 0.38	$22.59^{+0.81}_{-0.79}$	24.30 ± 0.08	20.84 ± 1.48	24.15 ± 0.14	-22.68 ± 0.04	...
A1365	7.67 ± 1.11	$20.60^{+4.61}_{-3.95}$	23.93 ± 0.42	0.96 ± 0.18	$347.5^{+23.21}_{-22.10}$	28.67 ± 0.13	0.50 ± 0.05	118.3 ± 22.60	26.94 ± 0.29	-23.67 ± 0.07	d
A1367	9.80 ± 0.77	$74.47^{+9.17}_{-8.40}$	26.12 ± 0.25	52.23 ± 15.99	25.32 ± 0.66	-23.32 ± 0.13	...
A1371	2.03 ± 0.63	$3.87^{+0.73}_{-0.64}$	21.24 ± 0.30	2.12 ± 0.21	$104.7^{+4.49}_{-4.35}$	25.62 ± 0.09	0.89 ± 0.02	72.45 ± 3.19	24.77 ± 0.05	-23.89 ± 0.03	a
A1400	16.49 ± 5.48	$15.57^{+2.30}_{-2.07}$	24.50 ± 0.30	20.56 ± 6.68	24.98 ± 0.75	-21.67 ± 0.15	...

Table 4
(Continued)

Cluster	First Semimajor Axis Sérsic Component			Second Semimajor Axis Sérsic Component			$S_2/(S_1 + S_2)$	Parameters from 2D Profile Integration			Feature
	n_1	$r_{e,1}$ (kpc)	$SB_{e,1}$ (g' mag $^{n-2}$)	n_2	$r_{e,2}$ (kpc)	$SB_{e,2}$ (g' mag $^{n-2}$)		r_e (kpc)	SB_e (g' mag $^{n-2}$)	M_{tot} (g' mag)	
(1)	(2)	(3)	(4)	(5)	(6)	(7)	(8)	(9)	(10)	(11)	(12)
A1413	16.34 ± 1.91	7256^{+4667}_{-3141}	32.50 ± 1.01	3083 ± 2766	29.14 ± 2.90	-26.19 ± 0.53	...
A1423	3.58 ± 0.13	$19.46^{+0.93}_{-0.90}$	23.54 ± 0.09	0.76 ± 0.15	$225.1^{+10.64}_{-10.27}$	28.73 ± 0.10	0.33 ± 0.03	41.62 ± 3.99	25.20 ± 0.29	-23.43 ± 0.04	d
A1424	8.93 ± 1.58	$151.7^{+40.16}_{-33.50}$	26.67 ± 0.51	97.78 ± 32.81	25.63 ± 0.95	-24.35 ± 0.15	c
A1435	4.66 ± 0.37	$49.23^{+3.08}_{-2.94}$	25.17 ± 0.13	31.17 ± 3.19	24.12 ± 0.32	-23.26 ± 0.05	c
A1436	7.29 ± 2.50	$18.40^{+20.06}_{-10.95}$	23.98 ± 1.50	1.44 ± 0.37	$147.5^{+8.09}_{-7.77}$	27.10 ± 0.21	0.54 ± 0.12	53.41 ± 2.82	25.22 ± 0.08	-23.38 ± 0.03	ac
A1452	7.27 ± 0.72	$51.62^{+4.06}_{-3.83}$	25.15 ± 0.16	38.79 ± 6.49	24.48 ± 0.34	-23.50 ± 0.08	a
A1507	5.49 ± 0.41	$35.45^{+1.64}_{-1.59}$	24.48 ± 0.10	29.02 ± 2.57	24.00 ± 0.20	-23.30 ± 0.05	...
A1516	4.63 ± 0.22	$63.37^{+2.29}_{-2.23}$	24.89 ± 0.08	47.19 ± 3.66	24.27 ± 0.13	-24.16 ± 0.04	...
A1526	15.44 ± 4.15	$56.23^{+47.20}_{-28.84}$	26.32 ± 1.33	0.50 ± 0.14	$265.9^{+15.58}_{-14.92}$	28.53 ± 0.14	0.29 ± 0.11	61.94 ± 12.16	26.22 ± 0.29	-23.20 ± 0.07	...
A1534	4.69 ± 0.30	$38.13^{+1.38}_{-1.35}$	24.33 ± 0.08	32.85 ± 2.33	23.95 ± 0.13	-23.62 ± 0.04	...
A1569	4.58 ± 2.62	$3.76^{+1.31}_{-1.04}$	21.05 ± 0.61	2.11 ± 0.25	$146.9^{+8.02}_{-7.70}$	26.31 ± 0.11	0.83 ± 0.04	98.19 ± 5.54	25.42 ± 0.08	-23.79 ± 0.04	c
A1589	6.67 ± 0.66	$160.4^{+23.56}_{-21.22}$	26.39 ± 0.29	123.5 ± 30.95	25.91 ± 0.49	-24.59 ± 0.11	bc
A1610	3.74 ± 0.19	$22.92^{+0.57}_{-0.56}$	23.61 ± 0.05	16.78 ± 0.48	23.09 ± 0.06	-23.22 ± 0.02	c
A1656	9.00 ± 0.90	$784.0^{+291.1}_{-227.6}$	29.30 ± 0.62	421.2 ± 234.7	27.58 ± 1.35	-24.97 ± 0.29	ac
A1668	2.97 ± 0.17	$27.35^{+2.36}_{-2.22}$	23.68 ± 0.15	0.86 ± 0.17	$274.4^{+13.58}_{-13.09}$	28.12 ± 0.11	0.40 ± 0.04	56.30 ± 3.68	25.20 ± 0.12	-23.78 ± 0.03	c
A1691	16.87 ± 3.63	$552.0^{+404.7}_{-260.3}$	29.33 ± 1.19	333.8 ± 220.2	27.73 ± 1.61	-24.87 ± 0.33	c
A1749	11.20 ± 0.95	$104.6^{+12.95}_{-11.85}$	26.48 ± 0.25	68.99 ± 24.29	25.46 ± 0.82	-23.84 ± 0.15	...
A1767	5.38 ± 0.33	$195.9^{+17.03}_{-15.99}$	26.57 ± 0.17	131.7 ± 31.46	25.71 ± 0.37	-24.64 ± 0.11	b
A1775	7.31 ± 0.44	$153.9^{+13.16}_{-12.36}$	26.64 ± 0.17	126.1 ± 38.52	26.11 ± 0.69	-24.49 ± 0.14	...
A1795	3.47 ± 1.27	$17.68^{+9.39}_{-6.70}$	23.05 ± 0.79	1.42 ± 0.14	$199.2^{+10.21}_{-9.83}$	26.00 ± 0.14	0.78 ± 0.06	127.7 ± 4.72	25.23 ± 0.05	-24.64 ± 0.02	c
A1800	3.57 ± 0.15	$79.54^{+2.45}_{-2.40}$	24.29 ± 0.07	67.94 ± 3.40	23.83 ± 0.08	-24.55 ± 0.03	bc
A1809	9.12 ± 0.90	$111.7^{+33.43}_{-27.30}$	26.16 ± 0.52	0.16 ± 0.01	$71.76^{+3.2E8}_{-2.7E8}$	27.31 ± 0.15	0.24 ± 0.01	85.80 ± 13.65	25.46 ± 0.17	-24.41 ± 0.06	b
A1812	6.03 ± 0.55	$121.9^{+17.05}_{-15.43}$	27.31 ± 0.27	90.05 ± 30.34	26.67 ± 0.95	-23.20 ± 0.16	...
A1825	3.87 ± 0.22	$29.28^{+0.85}_{-0.84}$	24.21 ± 0.07	23.63 ± 1.06	23.75 ± 0.07	-23.08 ± 0.03	acd
A1828	10.99 ± 2.26	$3.03^{+1.36}_{-1.01}$	19.58 ± 0.90	10.07 ± 0.57	22.20 ± 0.14	-22.49 ± 0.03	...
A1831	6.44 ± 0.35	$270.2^{+25.34}_{-23.85}$	27.04 ± 0.18	226.1 ± 63.27	26.60 ± 0.56	-25.07 ± 0.16	...
A1890	5.95 ± 0.37	$53.23^{+2.46}_{-2.37}$	24.57 ± 0.10	38.85 ± 3.46	23.83 ± 0.23	-23.95 ± 0.05	...
A1899	2.76 ± 0.16	$9.60^{+0.53}_{-0.51}$	22.02 ± 0.11	0.87 ± 0.27	$119.3^{+8.62}_{-8.18}$	27.87 ± 0.15	0.27 ± 0.03	17.13 ± 0.41	23.21 ± 0.07	-22.87 ± 0.01	d
A1904	6.83 ± 0.43	$164.3^{+15.21}_{-14.22}$	26.61 ± 0.18	123.6 ± 37.51	25.86 ± 0.68	-24.43 ± 0.13	...
A1913	8.87 ± 0.80	$77.53^{+9.44}_{-8.65}$	26.47 ± 0.24	37.30 ± 9.84	24.86 ± 0.49	-23.08 ± 0.12	...
A1982	3.97 ± 0.22	$37.70^{+1.30}_{-1.27}$	24.30 ± 0.08	31.80 ± 1.78	24.01 ± 0.10	-23.18 ± 0.03	b
A1983	16.03 ± 2.07	$1047^{+613.8}_{-425.5}$	31.42 ± 0.95	431.5 ± 352.1	28.58 ± 2.22	-23.72 ± 0.43	...
A2022	24.43 ± 4.06	$3.3E4^{+5.7E4}_{-2.4E4}$	36.96 ± 2.17	$1.1E4 \pm 1.1E4$	31.16 ± 5.02	-25.12 ± 0.80	...
A2029	5.55 ± 0.26	$261.2^{+17.47}_{-16.64}$	26.08 ± 0.14	329.3 ± 82.12	26.53 ± 0.73	-25.85 ± 0.12	...
A2052	4.02 ± 0.23	$79.16^{+4.74}_{-4.54}$	25.32 ± 0.12	47.87 ± 2.12	24.33 ± 0.11	-23.64 ± 0.03	d
A2061	23.24 ± 6.48	$158347^{+777761}_{-152375}$	38.80 ± 4.12	64592 ± 64343	32.39 ± 5.97	-26.02 ± 1.10	b
A2063	8.46 ± 0.64	$345.6^{+68.57}_{-59.69}$	28.41 ± 0.36	202.1 ± 103.1	27.00 ± 1.21	-24.02 ± 0.23	...
A2065	7.58 ± 2.29	$25.55^{+23.75}_{-13.92}$	24.42 ± 1.34	1.24 ± 0.30	$189.5^{+8.79}_{-10.35}$	27.35 ± 0.18	0.58 ± 0.13	91.60 ± 6.60	25.79 ± 0.11	-23.78 ± 0.04	...
A2107	3.31 ± 0.11	$35.71^{+1.28}_{-1.24}$	23.78 ± 0.07	0.43 ± 0.08	$352.5^{+11.00}_{-10.75}$	28.74 ± 0.08	0.27 ± 0.02	60.10 ± 3.01	24.85 ± 0.15	-24.09 ± 0.02	c
A2122	3.35 ± 0.13	$58.19^{+1.52}_{-1.49}$	24.53 ± 0.06	43.82 ± 1.52	23.86 ± 0.09	-24.03 ± 0.02	...

Table 4
(Continued)

Cluster	First Semimajor Axis Sérsic Component			Second Semimajor Axis Sérsic Component			$S_2/(S_1 + S_2)$	Parameters from 2D Profile Integration			Feature
	n_1	$r_{e,1}$ (kpc)	$SB_{e,1}$ (g' mag $^{n-2}$)	n_2	$r_{e,2}$ (kpc)	$SB_{e,2}$ (g' mag $^{n-2}$)		r_e (kpc)	SB_e (g' mag $^{n-2}$)	M_{tot} (g' mag)	
(1)	(2)	(3)	(4)	(5)	(6)	(7)	(8)	(9)	(10)	(11)	(12)
A2147	1.43 ± 0.39	$6.32^{+0.79}_{-0.73}$	21.78 ± 0.17	1.77 ± 0.16	$85.49^{+2.93}_{-2.86}$	25.26 ± 0.07	0.84 ± 0.03	56.15 ± 1.32	24.44 ± 0.04	-23.50 ± 0.01	a
A2151	8.91 ± 0.70	$152.4^{+23.52}_{-21.08}$	27.21 ± 0.30	111.9 ± 42.43	26.48 ± 0.69	-23.80 ± 0.17	...
A2152	5.51 ± 0.30	$11.78^{+0.86}_{-0.81}$	22.89 ± 0.14	0.52 ± 0.03	$188.8^{+3.04}_{-3.00}$	26.92 ± 0.04	0.60 ± 0.01	95.39 ± 2.25	26.13 ± 0.01	-23.56 ± 0.01	a
A2162	6.36 ± 0.51	$20.11^{+3.50}_{-3.09}$	23.52 ± 0.30	0.70 ± 0.09	$99.66^{+2.09}_{-2.06}$	26.38 ± 0.09	0.34 ± 0.03	33.13 ± 1.06	24.15 ± 0.06	-23.22 ± 0.02	c
A2197	5.19 ± 0.29	$35.00^{+1.42}_{-1.37}$	23.89 ± 0.09	28.29 ± 1.63	23.51 ± 0.13	-23.48 ± 0.03	b
A2199	7.23 ± 0.19	$144.2^{+6.09}_{-5.90}$	26.31 ± 0.09	101.7 ± 27.05	25.50 ± 0.50	-24.22 ± 0.12	d
A2247	6.31 ± 1.29	$72.43^{+24.69}_{-19.65}$	26.30 ± 0.61	40.63 ± 5.83	25.14 ± 0.43	-22.93 ± 0.08	...
A2248	4.39 ± 0.27	$39.20^{+1.40}_{-1.36}$	24.60 ± 0.08	26.15 ± 1.42	23.66 ± 0.09	-23.27 ± 0.03	...
A2255	23.77 ± 6.61	9338^{+23985}_{-7908}	34.64 ± 2.92	5055 ± 4844	30.86 ± 3.90	-25.53 ± 0.75	...
A2256	10.96 ± 1.14	$217.4^{+45.73}_{-39.50}$	27.41 ± 0.40	169.2 ± 71.65	26.54 ± 0.77	-24.61 ± 0.20	a
A2271	6.17 ± 0.29	$111.9^{+6.54}_{-6.26}$	25.99 ± 0.12	56.83 ± 7.09	24.61 ± 0.22	-23.96 ± 0.07	c
A2293	8.59 ± 1.13	$85.51^{+14.85}_{-13.14}$	26.10 ± 0.34	89.57 ± 27.84	26.16 ± 0.64	-23.81 ± 0.12	d
A2308	10.92 ± 1.49	$270.9^{+83.32}_{-67.68}$	27.92 ± 0.56	130.0 ± 66.38	26.34 ± 1.32	-24.39 ± 0.21	...
A2319	1.34 ± 0.13	$22.61^{+2.12}_{-1.98}$	22.69 ± 0.13	1.18 ± 0.25	$168.6^{+11.88}_{-11.29}$	26.39 ± 0.14	0.64 ± 0.04	92.40 ± 3.15	25.40 ± 0.05	-24.64 ± 0.02	d
A2388	11.08 ± 0.79	$526.6^{+173.4}_{-139.0}$	29.52 ± 0.54	0.16 ± 0.06	$141.0^{+1.7E11}_{-1.6E11}$	28.87 ± 0.12	0.25 ± 0.04	327.4 ± 123.1	27.79 ± 0.51	-24.06 ± 0.19	...
A2469	4.08 ± 0.34	$50.30^{+3.65}_{-3.46}$	25.99 ± 0.15	31.83 ± 2.92	25.14 ± 0.24	-22.47 ± 0.06	...
A2495	3.81 ± 0.22	$157.7^{+12.03}_{-11.38}$	25.78 ± 0.15	104.2 ± 9.91	25.02 ± 0.17	-24.61 ± 0.05	...
A2506	4.06 ± 0.17	$23.76^{+0.67}_{-0.66}$	23.81 ± 0.06	16.66 ± 0.59	23.14 ± 0.07	-22.61 ± 0.02	d
A2513	3.50 ± 0.09	$23.07^{+0.41}_{-0.40}$	23.47 ± 0.04	20.22 ± 0.43	23.19 ± 0.04	-23.20 ± 0.01	...
A2516	4.21 ± 0.29	$16.82^{+0.61}_{-0.59}$	22.91 ± 0.08	17.31 ± 0.53	23.02 ± 0.05	-23.38 ± 0.02	...
A2524	5.11 ± 0.36	$39.90^{+1.74}_{-1.69}$	24.37 ± 0.09	32.46 ± 2.48	23.96 ± 0.18	-23.73 ± 0.04	...
A2558	6.25 ± 0.39	$79.90^{+5.94}_{-5.63}$	26.25 ± 0.15	55.86 ± 12.99	25.46 ± 0.59	-23.32 ± 0.11	...
A2572	8.43 ± 0.47	$109.3^{+10.50}_{-9.80}$	26.67 ± 0.19	73.14 ± 24.10	25.79 ± 0.74	-23.57 ± 0.14	d
A2589	5.92 ± 0.26	$276.8^{+24.84}_{-23.27}$	27.32 ± 0.17	113.7 ± 26.69	25.45 ± 0.50	-24.14 ± 0.12	c
A2593	5.78 ± 0.47	$72.58^{+6.14}_{-5.77}$	25.41 ± 0.17	45.63 ± 6.32	24.52 ± 0.36	-23.56 ± 0.07	d
A2618	6.97 ± 0.48	$129.4^{+12.31}_{-11.49}$	26.17 ± 0.19	88.33 ± 19.27	25.32 ± 0.49	-24.50 ± 0.10	...
A2622	5.05 ± 0.21	$37.77^{+3.01}_{-2.84}$	24.35 ± 0.15	0.67 ± 0.19	$410.8^{+38.95}_{-36.36}$	28.76 ± 0.18	0.32 ± 0.04	62.06 ± 6.46	25.28 ± 0.19	-23.83 ± 0.04	...
A2625	2.82 ± 0.13	$13.16^{+0.34}_{-0.33}$	22.40 ± 0.05	13.08 ± 0.16	22.42 ± 0.02	-22.75 ± 0.01	...
A2626	4.97 ± 0.33	$61.03^{+3.34}_{-3.21}$	24.83 ± 0.11	47.21 ± 3.63	24.34 ± 0.19	-23.83 ± 0.04	d
A2630	5.87 ± 0.63	$7.17^{+0.52}_{-0.49}$	22.18 ± 0.15	7.16 ± 0.18	22.08 ± 0.04	-22.16 ± 0.02	...
A2634	4.79 ± 0.28	$56.56^{+3.38}_{-3.23}$	24.73 ± 0.13	42.75 ± 3.31	24.05 ± 0.17	-23.67 ± 0.04	bd
A2637	9.63 ± 1.09	$46.50^{+3.79}_{-3.57}$	24.82 ± 0.17	36.44 ± 7.56	24.21 ± 0.35	-23.76 ± 0.09	...
A2657	3.17 ± 0.17	$48.52^{+2.05}_{-1.99}$	24.86 ± 0.09	32.94 ± 1.36	23.98 ± 0.08	-23.04 ± 0.03	b
A2665	4.29 ± 0.15	$61.63^{+4.77}_{-4.51}$	24.81 ± 0.13	0.19 ± 0.04	$170.1^{+33.40}_{-29.11}$	27.30 ± 0.10	0.22 ± 0.04	75.08 ± 4.43	24.97 ± 0.17	-24.25 ± 0.03	...
A2666	4.79 ± 0.36	$33.19^{+1.90}_{-1.82}$	24.06 ± 0.13	27.40 ± 1.89	23.80 ± 0.14	-23.25 ± 0.04	cd
A2675	4.24 ± 0.38	$27.48^{+5.41}_{-4.71}$	23.85 ± 0.32	1.87 ± 0.31	$751.8^{+96.65}_{-88.15}$	28.28 ± 0.22	0.80 ± 0.03	430.4 ± 69.07	27.31 ± 0.28	-24.91 ± 0.10	...
A2678	5.76 ± 0.40	$9.59^{+0.74}_{-0.70}$	22.44 ± 0.15	1.02 ± 0.08	$370.7^{+14.97}_{-14.53}$	27.69 ± 0.08	0.74 ± 0.02	235.4 ± 19.22	26.89 ± 0.07	-24.04 ± 0.05	d
AWM1	4.99 ± 0.16	$14.47^{+0.33}_{-0.32}$	23.00 ± 0.05	16.51 ± 0.69	23.28 ± 0.11	-22.73 ± 0.02	bc
AWM5	6.53 ± 0.16	$58.72^{+1.98}_{-1.93}$	24.69 ± 0.07	41.67 ± 4.22	23.91 ± 0.20	-23.96 ± 0.05	...
AWM7	6.49 ± 0.17	$150.4^{+7.30}_{-7.04}$	26.22 ± 0.10	82.44 ± 16.77	24.94 ± 0.43	-24.22 ± 0.09	c

Table 4
(Continued)

Cluster	First Semimajor Axis Sérsic Component			Second Semimajor Axis Sérsic Component			$S_2/(S_1 + S_2)$	Parameters from 2D Profile Integration			Feature
	n_1	$r_{e,1}$ (kpc)	$SB_{e,1}$ ($g' \text{ mag}^{n-2}$)	n_2	$r_{e,2}$ (kpc)	$SB_{e,2}$ ($g' \text{ mag}^{n-2}$)		r_e (kpc)	SB_e ($g' \text{ mag}^{n-2}$)	M_{tot} ($g' \text{ mag}$)	
(1)	(2)	(3)	(4)	(5)	(6)	(7)	(8)	(9)	(10)	(11)	(12)
L2027	12.12 ± 1.66	$465.2^{+193.4}_{-147.3}$	29.58 ± 0.72	271.1 ± 199.8	27.66 ± 1.95	-23.85 ± 0.35	...
L2030	2.47 ± 0.11	$34.97^{+1.04}_{-1.02}$	24.28 ± 0.07	30.65 ± 0.67	23.96 ± 0.02	-22.75 ± 0.02	...
L2069	5.04 ± 0.29	$64.08^{+2.87}_{-2.77}$	24.82 ± 0.10	56.18 ± 6.74	24.43 ± 0.24	-24.34 ± 0.06	d
L2093	5.60 ± 0.55	$21.45^{+1.50}_{-1.42}$	24.00 ± 0.15	15.73 ± 1.15	23.50 ± 0.15	-22.49 ± 0.04	bd
L2211	5.34 ± 0.36	$26.18^{+1.03}_{-1.00}$	23.73 ± 0.09	21.23 ± 1.21	23.32 ± 0.11	-23.28 ± 0.03	c
L3009	77.14 ± 111.1	$3426^{+177679}_{-805.4}$	34.51 ± 14.30	3446 ± 3405	30.51 ± 5.51	-23.87 ± 0.67	d
L3055	5.39 ± 0.60	$57.26^{+6.39}_{-5.90}$	25.96 ± 0.23	49.05 ± 7.94	25.73 ± 0.33	-22.96 ± 0.08	...
L3152	5.39 ± 0.22	$30.84^{+2.33}_{-2.20}$	24.09 ± 0.14	0.25 ± 0.05	$175.1^{+4.82}_{-4.73}$	27.70 ± 0.09	0.22 ± 0.03	39.91 ± 1.59	24.52 ± 0.08	-23.41 ± 0.02	...
L3186	5.38 ± 0.42	$40.78^{+2.01}_{-1.94}$	24.59 ± 0.10	32.27 ± 3.29	24.02 ± 0.19	-23.49 ± 0.05	c
MKW4	4.20 ± 0.15	$39.32^{+1.00}_{-0.98}$	23.76 ± 0.06	31.81 ± 1.12	23.29 ± 0.07	-23.46 ± 0.02	b

Notes. All parameters are corrected for PSF broadening, dust extinction, and cosmic dimming and are K-corrected. The parameters of the single Sérsic fits (see Equation (11)) or double Sérsic fits (see Equation (12)) are given in columns (2)–(7). The errors are calculated solely from the covariance matrices of the fits. The fraction of the integrated outer Sérsic component (column 8) compared to the total galaxy light $S_2/(S_1 + S_2)$ is calculated by integrating both semimajor axis Sérsic functions out to infinite radius. Both components are assumed to have the same ellipticity profiles. The parameters from 2D profile integration are listed in columns (9)–(11). They are corrected for undetected ICL (see Section 5.4), and the errors are estimated from that correction. Column (12) lists the found types of accretion signatures: a = 2 BCGs, b = shells, c = tidal streams, and d = multiple nuclei.

(This table is available in machine-readable form.)

ORCID iDs

M. Kluge  <https://orcid.org/0000-0002-9618-2552>
 A. Riffeser  <https://orcid.org/0000-0002-5466-3892>
 R. Bender  <https://orcid.org/0000-0001-7179-0626>
 C. Goessl  <https://orcid.org/0000-0002-2152-6277>

References

- Abell, G. O., Corwin, H. G., Jr., & Olowin, R. P. 1989, *ApJS*, **70**, 1
- Albert, C. E., White, R. A., & Morgan, W. W. 1977, *ApJ*, **211**, 309
- Amorisco, N. C., Martínez-Delgado, D., & Schedler, J. 2015, arXiv:1504.03697
- Arnaboldi, M., Ventimiglia, G., Iodice, E., Gerhard, O., & Coccato, L. 2012, *A&A*, **545**, A37
- Arp, H., & Bertola, F. 1969, *ApL*, **4**, 23
- Arp, H., & Bertola, F. 1971, *ApJ*, **163**, 195
- Astropy Collaboration, Robitaille, T. P., Tollerud, E. J., et al. 2013, *A&A*, **558**, A33
- Atkinson, A. M., Abraham, R. G., & Ferguson, A. M. N. 2013, *ApJ*, **765**, 28
- Beers, T. C., & Tonry, J. L. 1986, *ApJ*, **300**, 557
- Bender, R. 1988, *A&A*, **193**, L7
- Bender, R., Burstein, D., & Faber, S. M. 1992, *ApJ*, **399**, 462
- Bender, R., Doebereiner, S., & Moellenhoff, C. 1988, *A&AS*, **74**, 385
- Bender, R., Kormendy, J., Cornell, M. E., & Fisher, D. B. 2015, *ApJ*, **807**, 56
- Bender, R., & Moellenhoff, C. 1987, *A&A*, **177**, 71
- Bender, R., Paquet, A., & Nieto, J.-L. 1991, *A&A*, **246**, 349
- Bender, R., Surma, P., Doebereiner, S., Moellenhoff, C., & Madejsky, R. 1989, *A&A*, **217**, 35
- Bernardi, M., Hyde, J. B., Sheth, R. K., Miller, C. J., & Nichol, R. C. 2007, *AJ*, **133**, 1741
- Bertin, E. 2006, in ASP Conf. Ser. 351, Astronomical Data Analysis Software and Systems XV, ed. C. Gabriel et al. (San Francisco, CA: ASP), 112
- Bertin, E. 2010, SWarp: Resampling and Co-adding FITS Images Together v2.38.0, Astrophysics Source Code Library, ascl:1010.068
- Bertin, E., & Armouts, S. 1996, *A&AS*, **117**, 393
- Besla, G., Martínez-Delgado, D., van der Marel, R. P., et al. 2016, *ApJ*, **825**, 20
- Bílek, M., Cuillandre, J.-C., Gwyn, S., et al. 2016, *A&A*, **588**, A77
- Bílek, M., Ebrová, I., Jungwiert, B., Jílková, L., & Bartošková, K. 2015, *CaJPh*, **93**, 203
- Bullock, J. S., & Johnston, K. V. 2005, *ApJ*, **635**, 931
- Byrd, G., & Valtonen, M. 1990, *ApJ*, **350**, 89
- Calcáneo-Roldán, C., Moore, B., Bland-Hawthorn, J., Malin, D., & Sadler, E. M. 2000, *MNRAS*, **314**, 324
- Capaccioli, M., Spavone, M., Grado, A., et al. 2015, *A&A*, **581**, A10
- Carlin, J. L., Beaton, R. L., Martínez-Delgado, D., & Gabany, R. J. 2016, *ASSL*, **420**, 219
- Cattapan, A., Spavone, M., Iodice, E., et al. 2019, *ApJ*, **874**, 130
- Chilingarian, I. V., Melchior, A.-L., & Zolotukhin, I. Y. 2010, *MNRAS*, **405**, 1409
- Chilingarian, I. V., & Zolotukhin, I. Y. 2012, *MNRAS*, **419**, 1727
- Chonis, T. S., Martínez-Delgado, D., Gabany, R. J., et al. 2011, in Proc. Frank N. Bash Symp. 2011, New Horizons in Astronomy, ed. S. Salviander, J. Green, & A. Pawlik (Trieste: PoS), 23, <http://pos.sissa.it/cgi-bin/reader/conf.cgi?confid=149>
- Contini, E., De Lucia, G., Villalobos, Á., & Borgani, S. 2014, *MNRAS*, **437**, 3787
- Contini, E., Yi, S. K., & Kang, X. 2018, *MNRAS*, **479**, 932
- Cooper, A. P., Cole, S., Frenk, C. S., et al. 2010, *MNRAS*, **406**, 744
- Cooper, A. P., D'Souza, R., Kauffmann, G., et al. 2013, *MNRAS*, **434**, 3348
- Cooper, A. P., Gao, L., Guo, Q., et al. 2015, *MNRAS*, **451**, 2703
- Côté, P., McLaughlin, D. E., Hanes, D. A., et al. 2001, *ApJ*, **559**, 828
- Crnojević, D., Sand, D. J., Spekkens, K., et al. 2016, *ApJ*, **823**, 19
- Cui, W., Murante, G., Monaco, P., et al. 2014, *MNRAS*, **437**, 816
- Da Rocha, C., & Mendes de Oliveira, C. 2005, *MNRAS*, **364**, 1069
- Da Rocha, C., Ziegler, B. L., & Mendes de Oliveira, C. 2008, *MNRAS*, **388**, 4015
- de Vaucouleurs, G. 1969, *ApL*, **4**, 17
- Donzelli, C. J., Muriel, H., & Madrid, J. P. 2011, *ApJS*, **195**, 15
- Duc, P.-A. 2017, in IAU Symp. 321, Formation and Evolution of Galaxy Outskirts, ed. A. Gil de Paz, J. H. Knapen, & J. C. Lee (Cambridge: Cambridge Univ. Press), 180
- Duc, P.-A., Cuillandre, J.-C., Karabal, E., et al. 2015, *MNRAS*, **446**, 120
- ESA 1997, ESA Spec. Publ., 1200
- Faber, S. M., Tremaine, S., Ajhar, E. A., et al. 1997, *AJ*, **114**, 1771
- Feldmeier, J. J., Mihos, J. C., Morrison, H. L., Rodney, S. A., & Harding, P. 2002, *ApJ*, **575**, 779
- Ferrarese, L., Côté, P., Cuillandre, J.-C., et al. 2012, *ApJS*, **200**, 4
- Flewellling, H. A., Magnier, E. A., Chambers, K. C., et al. 2016, arXiv:1612.05243
- Foster, C., Lux, H., Romanowsky, A. J., et al. 2014, *MNRAS*, **442**, 3544
- Gnedin, O. Y. 2003, *ApJ*, **582**, 141
- Gonzalez, A. H., Zabludoff, A. I., & Zaritsky, D. 2005, *ApJ*, **618**, 195
- González-García, A. C., & van Albada, T. S. 2005, *MNRAS*, **361**, 1043
- Gössl, C. A., & Riffeser, A. 2002, *A&A*, **381**, 1095
- Graham, A., Lauer, T. R., Colless, M., & Postman, M. 1996, *ApJ*, **465**, 534
- Gregg, M. D., & West, M. J. 1998, *Natur*, **396**, 549
- Hansen, S. M., Sheldon, E. S., Wechsler, R. H., & Koester, B. P. 2009, *ApJ*, **699**, 1333
- Harris, K. A., Debattista, V. P., Governato, F., et al. 2017, *MNRAS*, **467**, 4501
- Hartke, J., Arnaboldi, M., Gerhard, O., et al. 2018, *A&A*, **616**, A123
- Hernquist, L., & Quinn, P. J. 1988, *ApJ*, **331**, 682
- Hernquist, L., & Quinn, P. J. 1989, *ApJ*, **342**, 1
- Hoessel, J. G. 1980, *ApJ*, **241**, 493
- Høg, E., Fabricius, C., Makarov, V. V., et al. 2000, *A&A*, **355**, L27
- Hopkins, P. F., Cox, T. J., Dutta, S. N., et al. 2009, *ApJS*, **181**, 135
- Hopp, U., Bender, R., Goessl, C., et al. 2008, *Proc. SPIE*, **7016**, 70161T
- Hopp, U., Bender, R., Grupp, F., et al. 2014, *Proc. SPIE*, **9145**, 91452D
- Hoshino, H., Leauthaud, A., Lackner, C., et al. 2015, *MNRAS*, **452**, 998
- Huang, Z., Radovich, M., Grado, A., et al. 2011, *A&A*, **529**, A93
- Ibata, R. A., Lewis, G. F., McConnachie, A. W., et al. 2014, *ApJ*, **780**, 128
- Iodice, E., Capaccioli, M., Grado, A., et al. 2016, *ApJ*, **820**, 42
- Iodice, E., Spavone, M., Capaccioli, M., et al. 2017, *ApJ*, **839**, 21
- Iodice, E., Spavone, M., Capaccioli, M., et al. 2019, *A&A*, **623**, 1
- Jester, S., Schneider, D. P., Richards, G. T., et al. 2005, *AJ*, **130**, 873
- Johnston, K. V., Bullock, J. S., Sharma, S., et al. 2008, *ApJ*, **689**, 936
- Jorgensen, I., Franx, M., & Kjaergaard, P. 1992, *A&AS*, **95**, 489
- Karabal, E., Duc, P.-A., Kuntschner, H., et al. 2017, *A&A*, **601**, A86
- Karademir, G. S., Remus, R.-S., Burkert, A., et al. 2019, *MNRAS*, **487**, 318
- Kellogg, E., Gursky, H., Leong, C., et al. 1971, *ApJL*, **165**, L49
- Kormendy, J. 1973, *AJ*, **78**, 255
- Kormendy, J. 1977, *ApJ*, **218**, 333
- Kormendy, J. 1999, in ASP Conf. Ser. 182, Galaxy Dynamics, ed. D. R. Merritt, M. Valluri, & J. A. Sellwood (San Francisco, CA: ASP), 124
- Kormendy, J., & Bahcall, J. N. 1974, *AJ*, **79**, 671
- Kormendy, J., & Bender, R. 1996, *ApJL*, **464**, L119
- Kormendy, J., & Bender, R. 2012, *ApJS*, **198**, 2
- Kormendy, J., & Bender, R. 2013, *ApJL*, **769**, L5
- Kormendy, J., Fisher, D. B., Cornell, M. E., & Bender, R. 2009, *ApJS*, **182**, 216
- Kosyra, R., Gössl, C., Hopp, U., et al. 2014, *ExA*, **38**, 213
- Krick, J. E., & Bernstein, R. A. 2005, *BAAS*, **37**, 1452
- Lauer, T. R. 1988, *ApJ*, **325**, 49
- Lauer, T. R., Gebhardt, K., Faber, S. M., et al. 2007, *ApJ*, **664**, 226
- Lauer, T. R., Postman, M., Strauss, M. A., Graves, G. J., & Chisari, N. E. 2014, *ApJ*, **797**, 82
- Longobardi, A., Arnaboldi, M., Gerhard, O., Pulsoni, C., & Söldner-Rembold, I. 2018, *A&A*, **620**, A111
- Lucy, L. B. 1974, *AJ*, **79**, 745
- Malin, D. F., & Carter, D. 1980, *Natur*, **285**, 643
- Malin, D. F., & Carter, D. 1983, *ApJ*, **274**, 534
- Mancillas, B., Duc, P. A., Combes, F., et al. 2019, *A&A*, **632**, 122
- Martínez-Delgado, D., Gabany, R. J., Crawford, K., et al. 2010, *AJ*, **140**, 962
- Matthews, T. A., Morgan, W. W., & Schmidt, M. 1964, *ApJ*, **140**, 35
- Merritt, A., van Dokkum, P., Abraham, R., & Zhang, J. 2016, *ApJ*, **830**, 62
- Merritt, D. 1984, *ApJ*, **276**, 26
- Mihos, J. C. 2004, in Carnegie Observatories Centennial Symp., Clusters of Galaxies: Probes of Cosmological Structure and Galaxy Evolution, ed. J. S. Mulchaey, A. Dressler, & A. Oemler (Cambridge: Cambridge Univ. Press), 277
- Mihos, J. C., Harding, P., Feldmeier, J., & Morrison, H. 2005, *ApJL*, **631**, L41
- Mihos, J. C., Harding, P., Feldmeier, J. J., et al. 2017, *ApJ*, **834**, 16
- Mihos, J. C., & Hernquist, L. 1994, *ApJL*, **437**, L47
- Miville-Deschênes, M.-A., Duc, P.-A., Marleau, F., et al. 2016, *A&A*, **593**, A4
- Moffat, A. F. J. 1969, *A&A*, **3**, 455
- Moore, B., Katz, N., Lake, G., Dressler, A., & Oemler, A. 1996, *Natur*, **379**, 613
- Morgan, W. W., Kayser, S., & White, R. A. 1975, *ApJ*, **199**, 545
- Morgan, W. W., & Lesh, J. R. 1965, *ApJ*, **142**, 1364
- Oegerle, W. R., & Hill, J. M. 2001, *AJ*, **122**, 2858

- Okamoto, S., Arimoto, N., Ferguson, A. M. N., et al. 2015, [ApJL](#), **809**, L1
- Oser, L., Ostriker, J. P., Naab, T., Johansson, P. H., & Burkert, A. 2010, [ApJ](#), **725**, 2312
- Patel, P., Maddox, S., Pearce, F. R., Aragón-Salamanca, A., & Conway, E. 2006, [MNRAS](#), **370**, 851
- Pillepich, A., Nelson, D., Hernquist, L., et al. 2018, [MNRAS](#), **475**, 648
- Planck Collaboration, Ade, P. A. R., Aghanim, N., et al. 2014, [A&A](#), **571**, A1
- Pop, A.-R., Pillepich, A., Amorisco, N. C., & Hernquist, L. 2018, [MNRAS](#), **480**, 1715
- Postman, M., & Lauer, T. R. 1995, [ApJ](#), **440**, 28
- Puchwein, E., Springel, V., Sijacki, D., & Dolag, K. 2010, [MNRAS](#), **406**, 936
- Quinn, P. J. 1984, [ApJ](#), **279**, 596
- Rodríguez-Gómez, V., Pillepich, A., Sales, L. V., et al. 2016, [MNRAS](#), **458**, 2371
- Rudick, C. S., Mihos, J. C., Frey, L. H., & McBride, C. K. 2009, [ApJ](#), **699**, 1518
- Rudick, C. S., Mihos, J. C., & McBride, C. 2006, [ApJ](#), **648**, 936
- Schlaflly, E. F., & Finkbeiner, D. P. 2011, [ApJ](#), **737**, 103
- Schneider, D. P., Gunn, J. E., & Hoessel, J. G. 1983, [ApJ](#), **268**, 476
- Schombert, J. M. 1986, [ApJS](#), **60**, 603
- Schweizer, F., & Seitzer, P. 1988, [ApJ](#), **328**, 88
- Seigar, M. S., Graham, A. W., & Jerjen, H. 2007, [MNRAS](#), **378**, 1575
- Sérsic, J. L. 1968, Atlas de Galaxias Australes (Córdoba: Univ. Córdoba)
- Sharples, R. M., Zepf, S. E., Bridges, T. J., et al. 1998, [AJ](#), **115**, 2337
- Skibba, R. A., van den Bosch, F. C., Yang, X., et al. 2011, [MNRAS](#), **410**, 417
- Slater, C. T., Harding, P., & Mihos, J. C. 2009, [PASP](#), **121**, 1267
- Spavone, M., Capaccioli, M., Napolitano, N., et al. 2017, [Galax](#), **5**, 31
- Spavone, M., Iodice, E., Capaccioli, M., et al. 2018, [ApJ](#), **864**, 149
- Tal, T., van Dokkum, P. G., Nelan, J., & Bezanson, R. 2009, [AJ](#), **138**, 1417
- Thuan, T. X., & Kormendy, J. 1977, [PASP](#), **89**, 466
- Tojeiro, R., Masters, K. L., Richards, J., et al. 2013, [MNRAS](#), **432**, 359
- Tonry, J. L. 1985a, [ApJ](#), **291**, 45
- Tonry, J. L. 1985b, [AJ](#), **90**, 2431
- Trentham, N., & Mobasher, B. 1998, [MNRAS](#), **293**, 53
- Trujillo, I., & Fliri, J. 2016, [ApJ](#), **823**, 123
- van der Marel, R. P., & Franx, M. 1993, [ApJ](#), **407**, 525
- Von Der Linden, A., Best, P. N., Kauffmann, G., & White, S. D. M. 2007, [MNRAS](#), **379**, 867
- Watkins, A. E., Mihos, J. C., & Harding, P. 2015, [ApJL](#), **800**, L3
- Watkins, A. E., Mihos, J. C., Harding, P., & Feldmeier, J. J. 2014, [ApJ](#), **791**, 38
- Welch, G. A., & Sastry, G. N. 1971, [ApJL](#), **169**, L3
- Willmer, C. N. A. 2018, [ApJS](#), **236**, 47
- Wright, E. L. 2006, [PASP](#), **118**, 1711
- Zhang, Y., Yanny, B., Palmese, A., et al. 2019, [ApJ](#), **874**, 165
- Zibetti, S., White, S. D. M., Schneider, D. P., & Brinkmann, J. 2005, [MNRAS](#), **358**, 949
- Zwicky, F. 1951, [PASP](#), **63**, 61